NTNU

Norwegian University of
Science and Technology

Dynamic loads on Francis turbines

Ingebjørg Valkvæ

NTNU

Norwegian University
of Science and Technology

Department of Energy
and Process Engineering

EPT-M-2016-147

MASTER THESIS

for

Student
Ingebjørg Valkvæ

Spring 2016

Dynamic loads in Francis turbines

Dynamiske laster i Francisturbiner

Background and objective

The current electrical energy system is characterized by large variations in the production and consumption of electricity. Additional installation of power to the European grid is likely to be from an intermittent energy source like wind energy or photovoltaic solar energy. This will result in more need for balancing services like the ones that can be provided by hydro power plants producing power from reservoirs. Such balancing services are, however, putting stress on the mechanical equipment by exerting them to dynamical loads. The calculation of the stresses in the turbine runner material due to these dynamical loads are highly uncertain, yet these stresses are crucial when dimensioning the runner for operation and for prediction of the runner life time. The best computational tools used to evaluate such strains in hydraulic turbines are known as Fluid Structure Interaction (FSI) analysis, but still the need verification from laboratory measurements. Particle Image Velocimetry (PIV) is particular useful for this verification.

The objective of the master thesis is to perform a FSI analysis of a Francis runner model subjected to variable speed of rotation, as well as PIV measurements on the physical model. The model is installed at the Waterpower laboratory at NTNU and is the subject of much research to come.

The following tasks are to be considered:

1. Literature study on dynamical loads in a Francis turbine and PIV measurement techniques

2. Perform PIV measurements in the Francis test rig at specified, chosen operating conditions

3. Use FSI computational tools and complete the simulations initiated in the recent project work with the suggested modification from that work

4. Perform new simulations using test conditions from the PIV measurements and compare the results with the laboratory measurements

Within 14 days of receiving the written text on the master thesis, the candidate shall submit a research plan for his project to the department.

When the thesis is evaluated, emphasis is put on processing of the results, and that they are presented in tabular and/or graphic form in a clear manner, and that they are analyzed carefully.

The thesis should be formulated as a research report with summary both in English and Norwegian, conclusion, literature references, table of contents etc. During the preparation of the text, the candidate should make an effort to produce a well-structured and easily readable report. In order to ease the evaluation of the thesis, it is important that the cross-references are correct. In the making of the report, strong emphasis should be placed on both a thorough discussion of the results and an orderly presentation.

The candidate is requested to initiate and keep close contact with his/her academic supervisor(s) throughout the working period. The candidate must follow the rules and regulations of NTNU as well as passive directions given by the Department of Energy and Process Engineering.

Risk assessment of the candidate's work shall be carried out according to the department's procedures. The risk assessment must be documented and included as part of the final report. Events related to the candidate's work adversely affecting the health, safety or security, must be documented and included as part of the final report. If the documentation on risk assessment represents a large number of pages, the full version is to be submitted electronically to the supervisor and an excerpt is included in the report.

Pursuant to "Regulations concerning the supplementary provisions to the technology study program/Master of Science" at NTNU §20, the Department reserves the permission to utilize all the results and data for teaching and research purposes as well as in future publications.
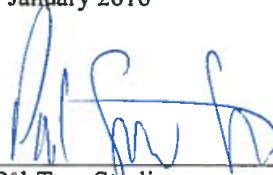
The final report is to be submitted digitally in DAIM. An executive summary of the thesis including title, student's name, supervisor's name, year, department name, and NTNU's logo and name, shall be submitted to the department as a separate pdf file. Based on an agreement with the supervisor, the final report and other material and documents may be given to the supervisor in digital format.

☒ Work to be done in lab (Water power lab, Fluids engineering lab, Thermal engineering lab)
☐ Field work

Department of Energy and Process Engineering, 13. January 2016

Olav Bolland
Department Head

Pål-Tore Storli
Academic Supervisor

Research Advisor:
Ole Gunnar Dahlhaug
Rakel Ellingsen

Acknowledgements

This master thesis was written at the Waterpower Laboratory at the Norwegian University of Science and Technology (NTNU) during the spring semester 2016. The thesis is a continuation of a project assignment carried out by the author during the corresponding fall semester. Execution of the laboratory experiment and the computer simulations were performed partly together with PhD Candidate Rakel Ellingsen and Postdoc. Fellow Chirag Trivedi.

I take this opportunity to gratefully acknowledge the assistance and contributions of several persons. First of all, I would like to thank my supervisor Pål-Tore Storli for his valuable guidance and reassurance during troubled times this year. His scientific approach have helped me to complete the given tasks. I would also like to thank my co-supervisors Rakel Ellingsen and Ole Gunnar Dahlhaug for sharing their ideas on the subject. Further thanks to master student Einar Agnalt and Chirag Trivedi. Einar have produced the computer aided design (CAD) models used in my work, and spent a lot of time on the laboratory preparations. Chirag conducted the necessary computational fluid dynamics (CFD) simulation and provided me with his results. I would not have been able to finalize my work without your help. I am also very grateful to all the other Ph.D. Candidates at the Waterpower Laboratory for their good advices, including a special thanks to Ph.D. Candidate Carl W. Bergan for the much needed help with computer programs and difficulties in the laboratory.

Finally, I want to express my gratitude to my family and boyfriend for their endless support throughout the time spent at NTNU. In addition, thanks to all my fellow students in the Mechanical Engineering class and at the Waterpower Laboratory. It has been an enjoyable journey.

Ingebjørg Valkvæ

Ingebjørg Valkvæ
Trondheim, 24.06.2016

Abstract

New installations of unregulated power to the electrical grid have led to more fluctuations in the grid frequency. Hydropower plants with large reservoirs can provide services to balance the frequency by increasing or reducing production in accordance to what is needed. However, such balancing services are putting stress on the turbines by exposing them to dynamic loads. In the recent years, several high head Francis turbines have been taken out of operation due to cracks in the runner. It is thought to be because the turbines are not designed with sufficient measures to handle all the types of dynamic loads appearing during variations in operation. Analysis of stresses caused by fluid-structure interaction (FSI) is therefore of increasing interest in the hydropower industry.

In this thesis, pressure and strain measurements have been performed on the Francis test rig in the Waterpower Laboratory at NTNU. The results were further used as validation of a FSI analysis conducted on the same turbine model in the software program ANSYS. The rotational speed of the runner was decreased by 60 revolutions per minute (RPM) over a time period of 2 seconds to illustrate how an estimated change in grid frequency impact stresses in the turbine.

The results from the FSI simulation showed high stresses both on the leading and trailing edge of the runner blades, where the maximum stress was found on the trailing edge tip towards the shroud. A decrease in runner speed resulted in a decrease in material stresses. At the end time, the maximum equivalent stress has a magnitude of 5 MPa, which is way below the yielding limit for the material. Validation of the CFD simulation showed sufficient correlation between the measured and simulated pressures. However, it was difficult to achieve a comparison of strain results with the strain gage, and the FSI results should therefore be further validated before they can be used as background for more research.

Sammendrag

Nye installasjoner av ikke-regulerbar elektrisitet i strømnettet har ført til større svingninger i nettfrekvensen. Vannkraftverk med store reservoarer kan tilby tjenester for å balansere frekvensen ved å øke eller redusere produksjonen i henhold til behovet. Slike balansetjenester påfører spenninger i turbinene ved å utsette dem for dynamiske belastninger. I de siste årene har flere høytrykk Francisturbiner måtte tas ut av drift på grunn av sprekker i løpehjulet. Det antas å være fordi turbinene ikke er utformet for å håndtere alle typer av dynamiske belastninger som opptrer i løpet av variasjoner i driften. Analyse av spenninger forårsaket av fluid-struktur interaksjon er derfor av økende interesse.

I denne oppgaven har trykk- og deformasjonsmålinger blitt gjennomført på Francis testriggen i Vannkraftlaboratoriet ved NTNU. Resultatene ble videre brukt som validering av en FSI analyse utført på samme turbinmodell i programmet ANSYS. Rotasjonshastigheten til løpehjulet ble redusert med 60 RPM i løpet av en periode på 2 sekunder for å illustrere hvordan en estimert forandring i nettfrekvensen påvirker spenninger i turbinen.

Resultatene fra FSI simuleringen viste høye spenninger både i forkant og bakkant av turbinbladene, hvor den maksimale belastning ble funnet på spissen av bakkanten mot turbinringen. En reduksjon i rotasjonshastigheten resulterte i en reduksjon i materialspenningene. Ved endetiden har den maksimal spenningen en størrelse på 5 MPa, noe som er langt under det som er flytgrensen til materialet. Validering av CFD simuleringen viste tilstrekkelig korrelasjon mellom målt og simulert trykk. Det var imidlertid vanskelig å oppnå en sammenligning av deformasjonsresultatene ved hjelp av strekklappen, og FSI resultatene bør derfor ytterligere valideres før de kan brukes som bakgrunn for videre forskning.

Contents

x

List of Tables

List of Figures

Nomenclature

Abbreviations

3D	Three-Dimensional
BEP	Best Efficiency Point
CAD	Computer Aided Design
CFD	Computational Fluid Dynamics
FEA	Finite Element Analysis
FEM	Finite Element Method
FSI	Fluid-Structure Interaction
HCF	High Cycle Fatigue
LCF	Low Cycle Fatigue
NTNU	Norwegian University of Science and Technology
RPM	Revolutions Per Minute
RSI	Rotor-Stator Interaction
TSO	Transmission System Operator

Greek symbols

δ	Magnetic torque angle	$^{\circ}$
ϵ	Strain	-
η	Efficiency	%
γ	Guide vane angle	$^{\circ}$
μ	Kinematic viscosity	$\mathrm{Ns/m}^2$
ω	Angular velocity	$1/\mathrm{s}$
ρ	Density	kg/m^3

σ	Stress	Pa

Other symbols

b_p	Permanent speed droop	%
u_r	Friction velocity	m/s
A	Area	m^2
D	Diameter	m
E	Modulus of elasticity	Pa
F	Force	N
f	Frequency	Hz
g	Gravity	m^2/s
H	Net head	m
J	Moment of inertia	kg m^2
l	Length	m
N	Rotor speed	RPM
P	Power	N m/s
p	Pressure	kPa
po	Number of stator poles	-
Q	Discharge	m^3/s
T	Torque	N m
y	Distance from node to wall	m
y+	Non-dim. wall distance	-

Subscripts

0	Original
d	Dampening
el	Electrical
gen	Generated
h	Hydraulic
i	Instantaneous
load	Demand
m	Magnetic

nom	Nominal
ran	Random
sys	System
tot	Total

Chapter 1

Introduction

Today's energy system is characterized by large time variations in consumption and production of electricity. This is partly due to the increasing installation of power from renewable energy sources, like wind turbines and solar cells, to the electrical grid. As a consequence, the grid frequency is fluctuating and there is more need for balancing services like the ones that can be provided by hydropower plants. However, such balancing services are exposing the rotating machinery to dynamic loads and increases the turbine stresses. These dynamic loads come in addition to other loads caused by pressure pulsations in the waterway. Calculation of material stresses in a turbine runner due to dynamic loads is uncertain, yet these stresses are crucial when dimensioning the runner for operation and for prediction of runner life.

In recent years, several turbines have received major damages just after a short period in operation [45]. This applies in particular to high head Francis turbines, the most commonly used turbine in Norway. The reasons behind the damages are not fully known, but dynamic loads are one of the likely causes. From the early days of hydropower production, turbines were designed to run continuously, operating at a rated head and discharge, while pumped-storage plants or gas turbines provided the regulatory power. The introduction of a new energy legislation in the beginning of the 1990s affected the energy market and hydropower operation. The current market requires a great flexibility in operation, and operation outside of the design point happens quite often.

An understanding of fluid-structure interaction in turbines have become more essential since the different turbine loads are mainly induced by the internal fluid flow. Fluid phenomena like rotor-stator interaction (RSI) and draft tube vortex rope are under investigation, but the link between fluid dynamics and structural mechanics is still not well established. Safe operation of a plant requires that the machine components are optimised with respect to both static and dynamic loading in the design phase. Accordingly, the numerical methods for prediction and analysis of dynamic loads must be improved.

1.1 Objective

This master thesis is a continuation of the author's project thesis aiming for a FSI analysis of a Francis turbine. Lack of time to perform PIV measurements, together with problems with execution of the CFD simulation, led to alterations in the original tasks of the master thesis. This did not change the purpose of the work and therefore did not require any large rearrangements. A new objective and new tasks were made in accordance with supervisor Pål-Tore Storli and are stated below.

The objective of the master thesis is to perform a FSI analysis of a Francis runner model subjected to variable speed of rotation, as well as pressure and strain measurements on the physical turbine model. The model is installed at the Waterpower laboratory at NTNU and is the subject of much research to come.

The following tasks are to be considered:

1. Literature study on dynamic loads in a Francis turbine, in addition to pressure and strain measurement techniques.

2. Perform transient pressure and strain measurements in the Francis test rig at chosen operating conditions.

3. Perform a FSI simulation using test conditions from the measurements as inputs.

4. Validate the simulation with the model measurements.

1.2 Previous and ongoing work

Unsteady flow in Francis turbines have been investigated for over 50 years. Different aspects have been studied, trying to determine what are causing the various load phenomena, how turbine material reacts and how further damage can be prevented through better design and operation restrictions. The researchers have mainly focused on pressure fluctuations in the flow path during steady state operation, such as those caused by rotor-stator interaction and vortex rope in the draft tube. However, since the operation of hydropower plants have changed after the introduction of the new energy law in 1991, dynamic loads and fatigue in Francis turbines have become a major field of study.

In 2010, Frunzaverde et al. [27] presented a failure analysis of a broken Francis turbine runner blade. The failure had appeared just some months after a welding repair work on a fatigue crack initiated near the trailing egde at the junction with the hub. They conducted a metallographic investigation on a piece of the damaged blade and concluded that the cracking of the blade was caused by improper welding conditions and high material stresses. In addition to this investigation, they performed numerical computations with static finite element analysis (FEA) in order to

evaluate the deformation and stress distribution on the blade. In 2012, Seidel et al. [40] evaluated RSI-induced stresses in Francis runners. They describe the equipment and procedure of strain gage measurements in Francis prototype runners, and how this is dependent on head and specific speed. The measurement data was compared with simulations of Francis runner dynamics to predict dynamic stresses caused by RSI. Furthermore, in 2014, Seidel et al. [41] published a paper called "Dynamic load in Francis runners and their impact on fatigue life". Summarized findings of recent investigations through experiments and CFD analysis enabling Francis runners which combine high efficiency and a robust mechanical design, were presented. Luna-Ramírez et al. [35] performed a failure analysis of moving blades in a Francis runner in 2015. The analysis consisted of determination of pressure on the blade surface using CFD, calculation of stress distribution in the runner at different operating conditions with the finite element method (FEM), and a simple fatigue analysis. Their results showed a large concentration of stresses in the T-joint between the blade and the hub during steady state operation at different loads.

The Waterpower Laboratory at NTNU have a long history on hydropower research, and over 400 master thesis have been written concerning different hydropower issues and developments. Kobro [34] wrote his PhD thesis on "Measurement of pressure pulsations in Francis turbines" in 2010. The conducted measurements were performed by means of onboard measuring equipment both in model runners and full-scale prototype runners. Resulting data sets were used to investigate the dynamic pressure and strain in the runners. The analysis results from both model and prototype runner showed that the wake leaving the guide vanes is the most severe source of dynamic pressure in the runner. Even though the draft tube vortex rope pulsation propagates upstream the runner, it did not appear as a significant frequency in the strain measurements. In 2012, Bergmann-Paulsen [18] carried out a static FSI analysis on selected turbine components to study sediment erosion and develop an improved turbine design. The results showed a stress distribution which coincided with the energy transfer along the runner blade. In addition to that for different designs, the stress was relatively low compared to the criteria for hydraulic turbines. The following year, Hovland [32] investigated pressure pulsations and stress in a high head Francis model turbine. She performed model tests on the Tokke turbine with simultaneously measurements of pressure at different parts of the waterway. Then, spectral analysis was performed on all measurements to map out frequencies and corresponding amplitudes at various load conditions. RSI induced pulsations dominated the vaneless space and runner channels. Pressure pulsations was dampened across the runner, and sensors at the trailing edge displayed large values compared to the sensors positioned at the outlet. In 2014, Haga [29] conducted pressure measurements on the Tokke runner during transient start and stop procedures. A Fast Fourier transform analysis was used to identify pressure oscillations. The results showed that the largest frequency experienced was the blade passing frequency during start/stop and operation at best efficiency point(BEP) and part load.

PhD Candidate Rakel Ellingsen [25] and Associate Professor Pål-Tore Storli [45], are currently investigating how today's variable grid frequency impact components

in hydropower plants with regard to dynamic loads. They have conducted field measurements and simulations in MATLAB on torque oscillations to calculate stresses in a Francis turbine. Simulation results gave a torque variation in the range of 3-5% of the set point value, meaning a 5% increase in the dynamic loads imparted on the turbine. The work is a part of a longer term goal, namely to identifying stress oscillations in a Francis runner operating at oscillating speed of rotation due to grid frequency variations. Furthermore, Postdoc. Fellow Chirag Trivedi is performing a fluid-structure analysis of a high head Francis turbine as a part of the Francis-99 project [2] [49]. Detailed mechanical analysis on the runner will be carried out under different operating conditions. Load variation, start-stop, total load rejection, and spin-no-load caused by penetration of intermittent power into the power grid network summarizes the transients being studied. Trivedi is a former PhD Candidate from Luleå University of Technology in Sweden, where he wrote his thesis on "Investigations of transient pressure loading on a high head Francis turbine".

Chapter 2

Theoretical background

2.1 Mechanical properties and failure of metals

Many materials are subjected to forces or loads when in service. In such situations it is necessary to know the characteristics of the material being used and to design the related component so that any excessive deformation and fracture are prevented. A material's mechanical behaviour is reflected by the relationship between an applied force/load and deformation. There are three ways a load may be applied: tension, compression, and shear [23]. Its magnitude may be constant over time or fluctuate continuously. To compare specimens of different sizes, load is calculated per unit area, also called normalization to the area. Force divided by area is defined as stress [30]. In tension and compression tests, the relevant area is that perpendicular to the force, while in shear or torsion tests, the area is perpendicular to the axis of rotation. As a result of a tensile or compressive stress, a change in dimensions or deformation elongation occur. To enable comparison of specimens with different length, the elongation is also normalized, but to the length L. This is defined as strain. Equations of stress, σ, and strain, ϵ, are given below:

$$\sigma = \frac{F}{A_0} \tag{2.1}$$

$$\epsilon = \frac{l_i - l_0}{l_0} = \frac{\Delta l}{l_0} \tag{2.2}$$

F is here the instantaneous force applied perpendicular to the cross section, A_0 is the original cross-sectional area prior to an applied load, l_0 is the original length of the material, and l_i is the instantaneous length. Strain can be positive (tensile) or negative (compression), and is sometimes expressed in units such as mm/mm although it is dimensionless [23].

2.1.1 Deformation

Two types of material deformation exists; elastic and plastic. Elastic deformation is characterized by Hooke's law (Equation (2.3)), where stress and strain are proportional to each other and result in a linear relationship in a plot [23].

$$\sigma = E \cdot \epsilon \tag{2.3}$$

E is the Modulus of Elasticity or Young's modulus, and a large E reflects a stiff material. With this type of deformation, the material will resume its original form when the applied force is removed. The graph in Figure 2.1 represents the relationship between stress and strain. Past the point of yielding (Y), stress and strain are no longer proportional. Permanent, non-reversible plastic deformation strikes. The stress increases to continue the plastic deformation to a maximum, and then decrease to a fracture. Tensile strength (TS) corresponds to the maximum stress; if the stress is held at this point, fracture will occur. The results are dependent on variables such as the material's composition, microscopic imperfections, the way the component is manufactured, the rate of loading, and the temperature during the loading [30].
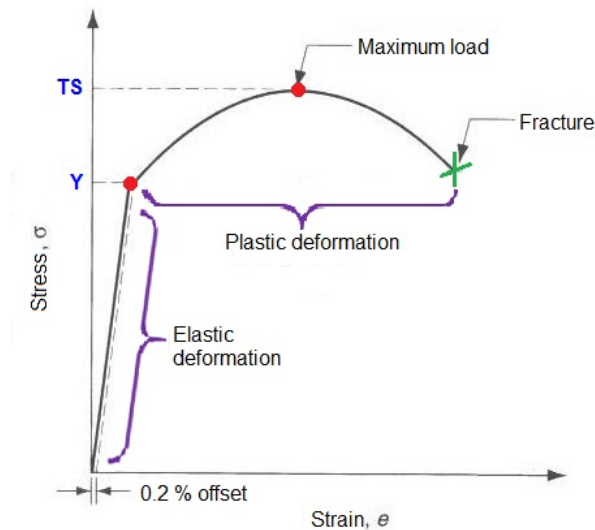
Figure 2.1: Engineering stress-strain-curve

2.1.2 Cracks

Ductility is a measure of the degree of plastic deformation before fracture [23]. Ductile materials often have high energy absorption and withstand substantial plastic

6

deformation before they fracture. A material that have low energy adsorption and tolerates very little or no plastic deformation before a fracture is called brittle. A ductile fracture is preferred if a fracture should occur, because such fractures are easier to detect due to the time domain of the plastic deformation. Prevention methods can then be performed when these types of cracks are detected. It is said to be a "stable" crack. In contrast, a brittle fracture occurs suddenly due to rapid crack propagation and are therefore called "unstable" cracks.

The measured fracture strengths for the majority of brittle materials are significantly lower than those predicted by theoretical calculations based on atomic bonding energies. This is because of the existence of microscopic flaws or cracks that exist under normal conditions at the surface or within the body of a material. A stress may be amplified or concentrated at a crack tip, and these flaws are therefore sometimes called stress raisers. However, stress amplification is not restricted to microscopic defects; it may occur at macroscopic internal discontinuities, at sharp corners, and at notches in large structures.

2.1.3 Fatigue

Fatigue is fracture which occurs during dynamic and variable loading. Under these circumstances, the fracture may appear at a stress level which is lower than the yield and tensile strength. The fracture often happens after a long period of cyclic tension. Fatigue is estimated to be the cause of about 90% of all metal failures [23]. It occurs suddenly, without any warning, and it is cut as a brittle fracture, even for ductile materials. There is seldom any plastic deformation before such a failure.

In order to specify a safe strength for metallic material under repeated loading, it is necessary to determine a limit below which no failure can be detected after applying a load for a specific number of cycles. By using a testing machine, a series of specimens can each be subjected to a predetermined stress and cycled to failure. The results are plotted as a graph representing the stress S on the vertical axis and the number of cycles to failure N on the horizontal axis. The graph is called a S-N diagram. The fatigue behaviour can be classified into two domains. One is associated with relatively high loads that produce not only elastic strain but also some plastic strain during each cycle. As a result, fatigue lives are relatively short; this domain is called low-cycle fatigue (LCF) and occurs at less than approximately 10^4 to 10^5 cycles [23]. For lower stress levels creating totally elastic deformations, longer life result. This is termed high-cycle fatigue (HCF) where large numbers of cycles are required to produce fatigue failure. It is related to fatigue lives greater than about 10^4 to 10^5 cycles.

Cracks related to fatigue failure almost always initiate on the surface of a component at some point of stress concentration. Crack nucleation sites include sharp fillets, surface scratches, threads, keyways, dents, and the like. In addition, cyclic loading can produce microscopic surface discontinuities as a consequence of dislocation slip of atoms that may also act as stress raisers, and thereby as crack initiation sites.

The design of a component can have a huge influence on its fatigue characteristics. The sharper the geometrical discontinuity on a surface, the more severe the stress concentration. Probability of fatigue failure might be reduced by avoiding (when possible) structural irregularities or by making modifications in design where sudden contour changes leading to sharp corners are eliminated - for example, designing rounded fillets with large radii of curvature at the point where there is a change in diameter. Also, it has been observed that improving the surface finish by polishing, imposing residual compressive stresses within a thin outer surface layer, and conducting case hardening, all are techniques that will enhance fatigue life significantly [23].

2.2 Energy generation

For more than 150 years, hydropower has been a significant contributor to energy generation. It is by far the most efficient method of large scale electric power production. Dependent on which type of turbine being employed in a power plant, the conversion efficiency can be as high as 95% for large installations [10]. Common to hydropower aggregates is that they can provide rapid effect grants and should thereby be able to meet fluctuations in energy consumption in the electrical system. This applies in particular to high pressure stations with large magazines [19].

2.2.1 Synchronous generators

The primary function of a hydropower generator is to convert the rotation of the shaft into electric power [52]. The basic process of generating electricity is to rotate a series of coils inside a magnetic field or vice versa. This leads to movement of electrons inside conductors, which produces electrical current. A synchronous generator have synchronized waveform of the generated voltage and rotation of the generator. Each peak of the sinusoidal waveform corresponds to a physical position of the rotor. The frequency is governed by Equation (2.4), where f is the frequency, N is the rotor speed, and po is the number of poles formed by the stator windings.

$$f = \frac{N \cdot po}{120} \tag{2.4}$$

2.2.2 The Nordic system

The Norwegian energy system is unique in that approximately all electricity is generated through hydropower. In 2010, this share was 95%, which means that Norway is the sixth largest hydropower producer in the world [16]. Norway have more than 800 magazines corresponding to 85 TWh. And with a high share of power installed, 30.1 GW, the Norwegian energy system have a relative large flexibility when it comes

to production based on demand [9]. In 1991, the energy system and energy market in Norway became liberalized. This implied that all got the right to choose their electricity supplier, and that the electricity market became competitive. Characteristics such as efficiency enhancement and greater cost consciousness in the operation of the power grid followed.

The Norwegian grid is connected with Sweden, Finland and east Denmark, and forms a joint synchronous system, the Nordic power system [36]. However, the electricity production differs considerably among the Nordic countries. As mentioned, in Norway nearly all electricity is generated from hydropower. Sweden and Finland use a combination of conventional thermal power, hydropower and nuclear power, with hydropower stations located mainly in northern areas and thermal power in the south [28]. Denmark relies primarily on conventional thermal power, but wind power is contributing with an increasing part of the demand for energy. The Nordic system is tuned to a frequency of 50.0 Hz, which means that the machines connected to the grid must be set so that they deliver/use a power of 50 Hz [16]. The system frequency is a continuously changing variable which is determined and controlled by real time balance between system demand and total generation. It indicates the "health condition" of the power grid. If the frequency is lower than 50 Hz, this is a sign of insufficient production. If the frequency is higher than 50 Hz, it implies that the production should be adjusted down. Should the deviation from 50 Hz become too large, components connected to the grid may automatically disconnect or be damaged.

Electricity needs to be produced in the same moment as it is used, and the consumption varies every minute as electrical apparatus are being adopted. Generally, the consumption of electricity is especially high in the morning and in the afternoon, and lower during night-time. The consumption is also significantly higher during the winter than the summer, since Norwegians use electricity for heating [16]. Statnett is Norway's transmission system operator (TSO). This means that the company facilitates the power market by making it physically possible to transport power from sellers to buyers. They are also responsible for keeping the Norwegian system in balance. To ensure that production of power at any given time is equal to consumption, Statnett demands that all electricity producers inform about their expected production one day in advance.
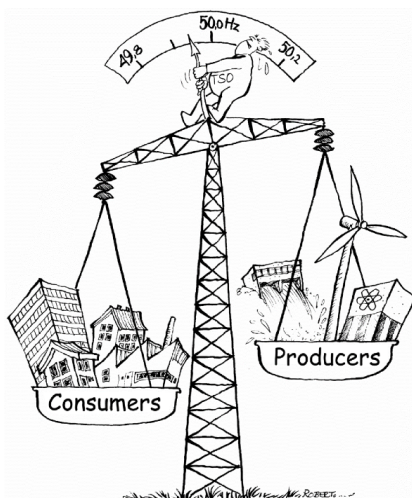
Figure 2.2: Coordinating production and consumption [43]

2.2.3 Implementation of renewable energy sources

The change towards a more environmental friendly future have led to replacement of many non-renewable energy sources like oil and gas with renewable energy sources. In July 2005, the European Economic Area (EEA) committee decided to include the Renewable Directive of the European Union (EU) into the EEA agreement [31]. The directive states that the share of renewable energy in EU should increase up to 20% from 2005 to 2020. Norway and Sweden have close collaboration on the power system development and are committed by the deal. Furthermore, in 2012, the electricity certificate market was established, where green certificates are intended to stimulate expansion of new renewable energy production equivalent to 24.6 TWh yearly within 2020 [31].

When it is desired to phase in electricity from renewable sources to the grid, a number of new challenges turn up. Renewable energy production is often characterized by variations over time in supply, tends to be unpredictable, and is hard to regulate. This implies in particular to solar and wind energy, where electricity produced from solar cells and wind turbines is characterized through production which seldom can be planned. Wind energy as a contributor to the electrical system will vary from hour to hour, while sun energy may vary within a couple of hours, due to the varying access dependent on weather conditions. Consequently, the information requirement from Statnett pose difficulties for renewable energy producers which only can predict their production a few hours ahead of time.

In addition does the renewable electricity generation behave quite different from traditional, centralized generation facilities, in that most of these sources do not contribute to systems reserves and to the total system inertia [47]. Inertia in the

rotating masses of synchronous aggregates decides the instant frequency response with respect to differences in the total power balance. When a frequency incident occurs, the synchronous machines will absorb or inject kinetic energy from or into the grid to correct the frequency deviation. The lower the system inertia is, the easier the grid frequency reacts on changes in generation and load patterns. The quality of the Nordic grid frequency has gradually become worse during the last years, meaning that an increase in frequency variations outside the normal range of 49.9 - 50.1 Hz has been observed [43]. This trend can be seen in Figure 2.3 and is most likely related to the utilization of new non-regulated energy sources, among other reasons.
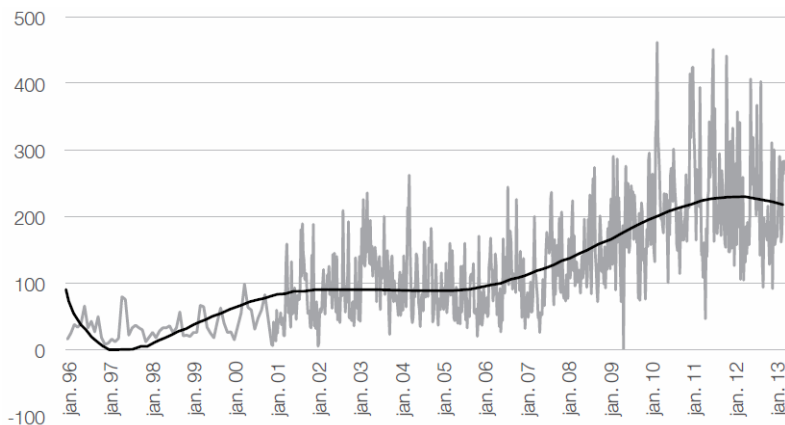
Figure 2.3: Number of minutes outside 49.9 - 50.1 Hz per week [43]

2.2.4 Frequency control

After the day-ahead trade is settled and the production plans are decided by the TSOs, imbalances can occur due to changes in the predicted consumption and production, faults in the systems or outages of transmission lines and plants. Balancing within the hour is therefore necessary to be able to maintain a sufficient system quality. This is done through intraday trade or through the use of reserves. Intraday trade (Elbas) was implemented in Norway in 2009, and makes it possible for balance responsible entities to adjust their plans closer to real time [53]. Instantaneous changes are handled by reserves for frequency control. In the Nordic system, one can distinguish between primary, secondary and tertiary control.

Frequency control in a power system can actually be divided into two phases. In the first phase, inertial response, the frequency controllers of the power plants are not activated. Instead, the generators release or absorb their kinetic energy to adjust the change in frequency. In a second phase, the frequency is first stabilized and then restored to the nominal frequency by the reserves. If a large frequency

disturbance occur, additional measures, like automatic load shedding, can be taken into consideration [47].

Inertial response

The frequency variation directly after a generation-load imbalance (ΔP) is determined by Equation (2.5), where P_{gen} is the generated power, P_{load} is the power demand, w_{el} is the electrical angular frequency, and J_{sys} is the total inertia of the system [47]. The right-hand side represents the derivative of the kinetic energy stored in all the generators of the power system.

$$P_{gen} - P_{load} = \frac{d(\frac{1}{2}J_{sys} \cdot w_{el}^2)}{dt} \tag{2.5}$$

The system inertia is dependent on two things: the number of operating generators and the inertia of each of these generators. Synchronous machines found in the standard power plants can contribute to this inertia based on the direct coupling between their rotational speed and the electrical frequency. On the other hand, wind turbines and photovoltaic units are equipped with converters that decouples the motion of the generator from the grid frequency, and therefore do not deliver any inertial response [38]. Replacing conventional generation by wind and solar power will thus result in a lower system inertia, which can lead to a high initial rate of change of frequency.

Primary frequency control

Primary frequency control plays a role between the first seconds (<30 s) after a frequency disturbance [24]. It is a result of automatic control of the synchronous machines, and immediately opposes frequency deviations without intervention through supervisory control or operator action. The frequency is regulated using a device called governor which regulates the power input of the turbine according to the rotational speed, in order to ensure stable operation of the generator. The governor action is dependent on two parameters, the dead band and the speed droop. The dead band of the governor decides the minimum amount of change in frequency needed before the governor action is activated [51]. While the speed droop is the ratio of the relative change in frequency to the relative change in power output. The mathematical expression for permanent speed droop, b_p is presented in Equation (2.6), where Δf is the change in frequency, f_{nom} is the nominal frequency (50 Hz on the Nordic grid), ΔP is the change in power at the power plant, and P_{nom} is the nominal power at the power plant. The droop is always positive to ensure stable operation, and the maximum value for the speed droop in the Nordic region is currently set to 6% [45]. The formula indicates that a drop in frequency gives increased

output.

$$b_p = \frac{\Delta f / f_{nom}}{\Delta P / P_{nom}} \tag{2.6}$$

Primary frequency control results in a new stationary position of the frequency that differs from the nominal value. Therefore, additional power must be added so that the frequency reaches its set-point value of 50.0 Hz. This is done by the secondary frequency control.

Secondary frequency control

Secondary frequency control governs the allocation of loading among the accessible power plants. It follows after the primary frequency control, and reacts in the time scale of minutes (15 s - 15 min) [24]. Typically, it adjusts utilization of load after generation. The secondary reserves have been manually controlled in the Nordic market for a long period. But since the quality of the electrical grid frequency has gone down during the last decade, Statnett implemented a new market for automatic secondary governing in 2013 [45].

Tertiary generation control

Tertiary generation control dominates minutes to hours (>15 min) after a frequency disturbance, and it is usually a planned event in anticipation of expected load changes [24]. It ensure combination of optimal energy production that minimizes costs while power demand in the market becomes saturated. The tertiary reserve is retrieved from the regulated electricity market, a common balance market for the Nordic electricity market. System administrators buy the power needed to balance the power system, and the providers gives a proce to regulate the power production up or down, and then have 15 minutes before the trade must be implemented.
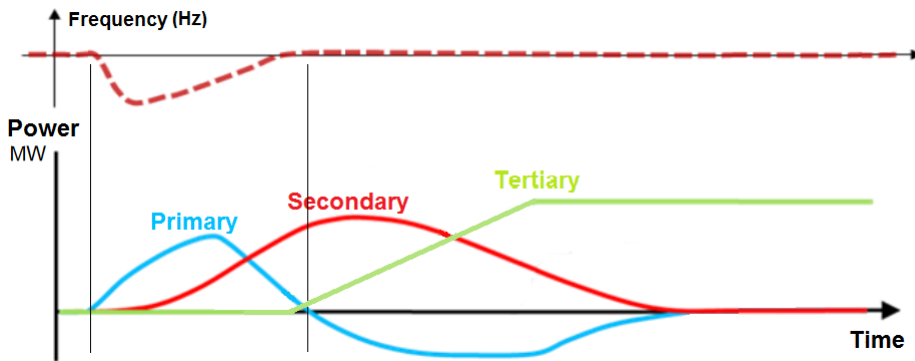
Figure 2.4: How different reserves balance the system

2.3 The Francis turbine

With approximately 60% of the global hydropower capacity in the world, Francis turbines are the most widely used type of hydro turbines [3]. The Francis turbine operates at heads between 15 and 700 meters and medium volume flow. It can quickly switch from pump to generation mode during changes in power demand, and the turbine is widely used to stabilize power grid operation [19].

2.3.1 Main components

Many of the components in a turbine construction are tailor made, and not all of them are found in every turbine. Manufacturers may also construct some details different. Moreover, the turbine constructions depend on the turbine size [33]. Below is a list of the main components found in a Francis turbine.

1. The scroll casing
3. Runner
4. Shaft
5. Draft tube cone
8. Stay vanes
9. Guide vanes
12. Upper cover
13. Sealing box
14. Guide bearing
14a. Bracket for the bearing(14)

15. Regulating ring
17. Lower cover
21. Replaceable wear and labyrinth rings
22. Link
23. Lever
24. Lower bearing for guide vane
25. Upper bearing for guide vane
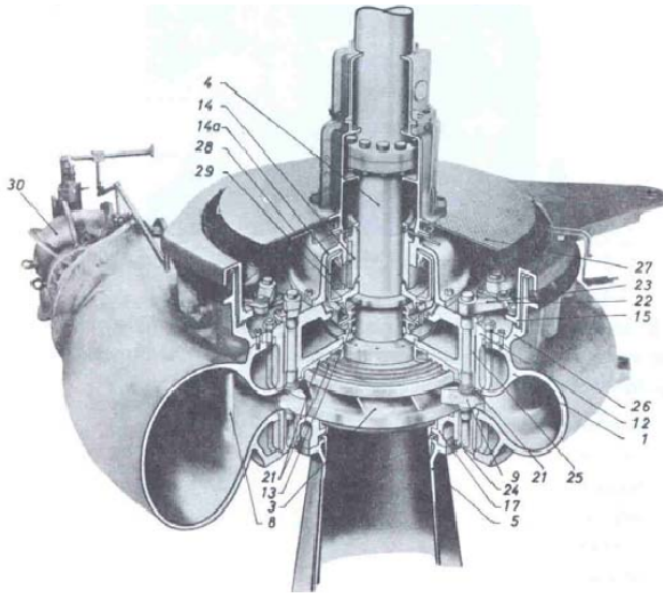
26. Bearing for the regulating ring
27. Floor
28. Rotating oil cylinder
29. Oil scoop fastened to (14a) and (14) with the opening against the rotating oil in rotating oil cylinder (28)

Figure 2.5: Illustration of a Francis turbine [33]

- **Spiral casing:** The spiral casing works as the water conduit between the penstock and the regulating mechanism. It serves to distribute the water equally around the circumference through the stay vanes and in towards the guide vanes. Since the cross-sectional area of the spiral casing is decreasing, the passing water is constantly accelerating and obtains a larger rotation.

- **Stay ring and stay vanes:** The stay ring consists of an upper and lower ring connected by the stay vanes. The purpose of the fixed stay vanes is to absorb the axial forces on the inside of the spiral casing, and they are shaped such that they almost don't affect the water flow.

- **Guide vanes:** The purpose of the adjustable guide vanes is to achieve a best possible uniform flow pattern with increasing rotation in towards the runner. In addition are the guide vanes used to regulate the water volume.

- **Covers:** The covers are fastened to the stay ring of the spiral casing. They

15

are designed with a high stiffness to assure minimum deformations caused by the water pressure. This is very important for achieving a small clearance gap between the guide vanes and the facing plates of the covers. The gap between the runner and the covers is also made as small as possible. Turbine covers support the guide vane trunnion bearings. In addition, the upper covers supports the regulating ring bearing, the labyrinth ring, the turbine bearing and the shaft seal box, while the lower cover supports the lower labyrinth ring and the draft tube cone.

- **Labyrinth seals:** Undesirable water leakage through the gaps between the runner and the covers cause reduced efficiency, but by placing labyrinth obstacles in the water way the amount of lost water can be reduced by creating a drop in pressure. The labyrinth consist of two parts, a static seal attached to the covers and a rotating part attached to the runner. For high head turbines, the leakage flow can by used as cooling water after it has been filtered through the labyrinth seal, which will increase the overall efficiency.

- **Runner:** The runner consists of a hub, a shroud and several blades connecting them together. The whole power output takes place in the turbine runner, as the runner transfers torque and power from the water to the turbine shaft through its rotation.

- **Draft tube:** The draft tube work as the water conduit from the runner to the outlet gate. It gradually reduces the velocity due to an increase of its cross-section, and thereby converting kinetic energy at the runner outlet to pressure energy at the draft tube outlet.

2.3.2   Operation

The Francis turbine is a type of reaction turbine, meaning that the turbine is completely submerged in water and experience a drop in pressure from the inlet to the outlet of the runner [19]. About half of the the specific energy at the inlet is kinetic energy and the other half is pressure energy. Through the runner, the energy is converted to mechanical energy partly due to the pressure drop and partly from the impulse forces caused by changes in the direction of the relative velocity vectors.

The flow pattern at an operating point is created by the inflow towards the runner blades and the outflow from the runner into the draft tube. Flow characteristics are idealistic only in a limited part of the operating range, which includes high efficiency and low fluctuations of pressure and output power. Off-design operating conditions with an inflow angle that deviates from the ideal angle comes with swirl, flow separation and backflow in the draft tube [41]. The velocity triangles of a Francis runner is shown in Figure 2.6, where $\vec{w}$ is directed in relative direction along the blades and $\vec{u}$ is directed in tangential direction. The absolute velocity is the sum of the two, $\vec{c} = \vec{u} + \vec{w}$ [19].
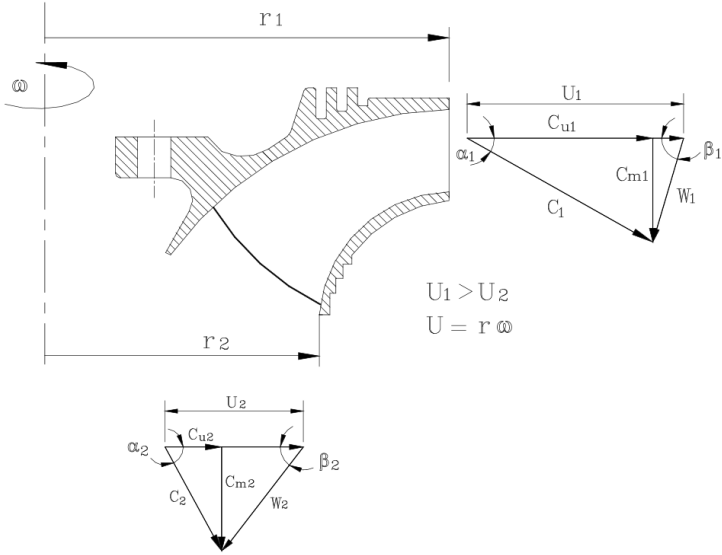
Figure 2.6: Velocity diagrams at the inlet and outlet of the runner [19]

2.3.3 Turbine performance

During both project planning and operation of plants, turbine performance characteristics of output and efficiency are needed to estimate the number and size of units required, quality of the production, and economic feasibility. The equations below are used for computation of the important quantities hydraulic efficiency η (Equation (2.7)) and head H (Equation (2.9)). τ is the turbine torque, ω is the angular velocity of the runner, and ρ is the density of water. Δp represents the pressure difference from inlet of the spiral casing to the outlet of the draft tube, while A is the cross sectional area at those specific locations.

$$\eta_M = \frac{\tau \cdot \omega}{p_M \cdot Q} \tag{2.7}$$

$$p_M = \Delta p + \frac{\rho \cdot Q^2}{2} \cdot \left(\frac{1}{A_1^2} - \frac{1}{A_2^2}\right) \tag{2.8}$$

$$H = \frac{p_M}{\rho \cdot g} \tag{2.9}$$

17

2.3.4 Francis runner

The shape of a runner blade cross-section is like a thin airfoil. So when water flows over it, a low pressure is induced on one side (suction side) and a high pressure on the other side (pressure side). The Francis runner has fixed blades, usually between seven and thirteen dependent on the operating head [48]. High head turbines are required to have a higher number of runner blades based on strength considerations. By increasing the number of blades, the pressure loading on the blades will be reduced, cavitation is avoided, and separation is prevented at the runner inlet during low loads. However, it also increases friction losses due to a larger amount of contact surfaces. Overall, the runner blades experience more stresses than other turbine parts because of the small distance between them and the large pressure variation from pressure side to suction side. They are therefore shaped in such a way that the main part of the hydraulic energy is utilized at the beginning of the blade, meaning that it's thicker at the inlet than at the outlet of the runner.

2.3.5 Material and design

The Francis components can be divided into pressurized static parts and movable stressed parts. The pressurized static parts includes the spiral casing, top and bottom cover, stay ring and draft tube, while the movable stressed parts includes the guide vanes, shaft, runner and labyrinth seals. For high head turbines, the stress carrying guide vanes and runner blades are often made of "fine grain high tensile strength carbon steel" [20]. The choice of material is based upon maximum stress and number of pressurized cycles experienced during operation. In contrast are components that require much welding, such as the covers and the draft tube, usually made of "fine grain low tensile stress with low carbon content steel". The development of new material technology over the years have improved cavitation resistance and increased the ductility of Francis turbines. Consequently, a higher stress level is tolerated in the stationary pressurized components. But for materials used in rotating parts with high frequency loads and on wet surfaces exposed to high flow rate, it is important that the residual stress level is held low to achieve a long turbine lifetime. When manufacturing a turbine, the weld quality must be perfected in order to avoid defects and brittleness in the heat affected zones of the material. Thus, in addition to improvements in casting and welding controls, limitations are often made in the chemical compositions as a safety procedure [21]. The advent of CAD and manufacturing occurred at the end of the 1970s and 1980s, and made many of the advances seen today possible. The use of CAD enhances the ability of an organization to work in a competitive environment to design site specific turbines. Modern CFD flow analysis, FEA techniques for engineering, and computer numerically controlled (CNC) in the industry, have significantly improved turbine efficiency and output accuracy. CFD analysis is today conducted by all turbine manufacturers as a part of the design process, and turbine geometry is now very close to design geometry thanks to CNC.

2.4 Loads on a Francis turbine

The operation regime of a hydraulic turbine can be divided into steady and transient state. The steady state is defined as stable operation at a fixed operational point, either BEP, part load or overload [35]. The turbine operates at a constant head, speed, load, and guide vane opening, while forces such as the static weight of the runner including the water weight, residual stresses and dynamic forces acts on the turbine. Residual stresses can be generated during construction and assembly of the turbine, but also during operation of the turbine due to bad welding and uneven heating. The effect of residual stress is amplified on complex shapes or in certain turbine components. Dynamic forces occurs with rotation of the unit as a result of the combination of unbalance and misalignment with other transient perturbations, like intermittent water flow or unwanted objects in the water. Static forces are constant in magnitude, direction and frequency, while dynamic forces are random, non-periodic forces with different directions, amplitude and frequencies. The transient state is characterized by change in head, load or guide vane opening related to starting, synchronization, changing load, stopping, load rejections, and runaway speed. During such operation, vibrations do not follow a specific pattern but develop depending on the amount of water going through the turbine.

2.4.1 Torque oscillations

In a hydropower plant, the turbine runner and the generator rotor are connected by the shaft and are rotating in the same direction. During operation, the hydraulic torque T_h from the water acting on the runner will try to accelerate the turbine, while the magnetic torque T_m acting on the generator will try to decelerate the turbine [25]. The summation of the different torques result in a net torque pulling on the turbine runner. As expressed in Equation (2.10), Newton's second law claims that a net torque is proportional to a change in angular velocity. In the equation, the right side consists of the mass moment of inertia J and the change in angular velocity of the runner ω. The left side is the summation of torques T, where T_d is the dampening torque from a mechanism in the generator that can cause both acceleration and deceleration. If the summation is equal to zero, the angular velocity will be constant. But when the accelerating torques are larger than the decelerating torques, the angular velocity will increase, or vice versa.

$$J\frac{d\omega}{dt} = \sum T = T_h - T_m - T_d \qquad (2.10)$$
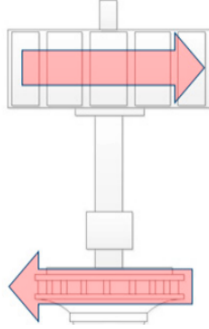
Figure 2.7: Net torque on the turbine [25]

The grid frequency determines how fast the generator stator magnetic field rotates. When power is generated, the magnetic field of the rotor pulls on the magnetic field of the stator. In phase, these fields are separated by the magnetic torque angle δ. If the grid frequency increases, the stator magnetic field catches up with the rotor field, decreasing δ and thereby decreasing the torque acting on the rotor from the stator. Equation (2.11) expresses how the torque acting on the rotor is connected to the magnitude of δ. Here, T_{nom} is the nominal torque and δ_{nom} is the nominal torque angle. As variations in grid frequency leads to variations in δ, generators are often equipped with a dampening mechanism to dampen these variations in magnetic angle. This counteraction is described in Equation (2.12), where m_d is a constant linking the magnitude of torque to the magnitude of the time derivative of the magnetic angle.

$$T_m = T_{nom} \frac{sin(\delta)}{sin(\delta_{nom})} \qquad (2.11)$$

$$T_d = m_d \frac{d\delta}{dt} \qquad (2.12)$$

The hydraulic torque T_h is a function of the hydraulic power P_h and angular velocity ω, as expressed in Equation (2.13) [25]. H represents the net head over the runner, Q is the volume flow, ρ is water density, g is the gravitational constant, and η_h is the hydraulic efficiency.

$$T_h = \frac{P_h}{\omega} = \frac{\rho g Q H \eta_h}{\omega} \qquad (2.13)$$

A variation in grid frequency will lead to changes in both ω and T_h. This is due to the fact that ω changes with frequency since generators are synchronous machines, and T_h changes based on the permanent speed droop. A decrease in frequency means a decrease in ω and this will reduce T_h according to Equation (2.13). The permanent

speed droop in the governor will work against the decrease in frequency by opening the guide vanes such that Q and P_h increases, thus reducing T_h even more. Hence, the speed droop mechanism amplifies the changes in T_h. If T_h increases while T_m is kept constant, the rotational speed of the turbine will increase. This means that the generator rotor will rotate faster than the magnetic field in the stator given by the grid frequency. δ and the induced torque in the generator will then increase until the hydraulic torque and the induced torque are equal once again. An increase in grid frequency will lead to an increase in rotational speed of the magnetic field in the generator stator. δ will then be reduced, which reduces the magnetic torque and the decelerating torque. The turbine's speed of rotation will further increase until the torques are equal and the grid frequency is proportional to the speed of rotation.

Even if the unit is operating at steady state, the influence of grid frequency variations leads to unsteady torque oscillations. The frequency varies much and relatively fast. These oscillations become dynamic loads on the rotating masses and increases material stresses in the turbine parts. They are characterized as slow oscillations and come in addition to all the other dynamic loads explained further below [45].

2.4.2 Pressure pulsations

When a Francis turbine is running at BEP, it will normally be influenced by oscillations caused by RSI [32]. However, when the operation moves outside of BEP, additional phenomena such as vortex breakdown and separation around curved lines appear. Off-design pressure pulsations can have large amplitudes that may cause serious damage to the structural runner. The magnitude of these oscillations is dependent on design, operational patterns and dynamic response of the system. They can occur periodically or stochastically. Experimental results have shown that low load oscillations often have a stochastic nature, while high load oscillations occur periodically [40]. Pressure pulsations can be divided into two categories; pulsations based on rotational oscillations from the turbine rotation (linked to the guide vanes, runner vanes, runner and draft tube) or pulsations based on elastic oscillations [29]. The elastic oscillations are a result of the flow changing through the turbine and causing a dynamic pressure difference, either an acceleration or retardation of the flow. This pressure wave will travel through the waterways of the plants and is dependent on adjustment of valves or vanes.

Rotor-stator interaction

Rotor-stator interaction can be characterized by two different phenomena: wake/rotor interaction and potential rotor/stator interaction [34].

- Wake/rotor interaction can be assumed steady in the stator reference frame, while they are unsteady in the rotor reference frame because the rotor is passing through wakes which are leaving the stator.

- Both stator and rotor experience non-uniform pressure components which results in unsteadiness from potential rotor/stator interaction.

The combination of these two phenomena creates a non-uniform velocity field entering the runner. As the radial clearance between the runner inlet and guide vane outlet (the vanless space) decreases, the level of pressure pulsations will increase.
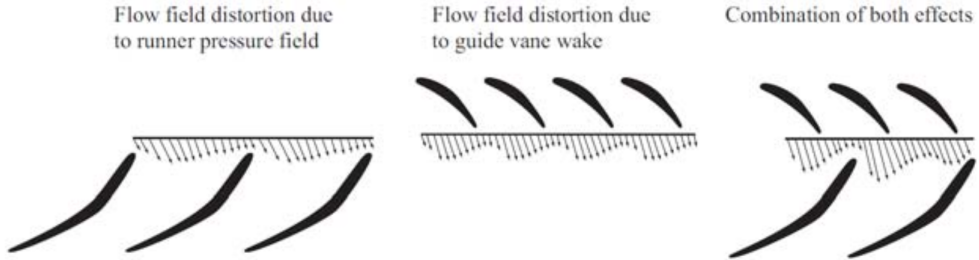
Figure 2.8: Flow field at inlet of runner [34]

Draft tube surge

Draft tube pressure pulsations in Francis turbines is a familiar phenomena. The flow pattern in the draft tube is determined by the direction of the flow exiting the rotating runner. At BEP, the direction is almost parallel to the shaft axis. But at points differing from BEP, a tangential velocity component is present, which is the source of several phenomena [34]:

- At loads below BEP, the direction of the tangential flow is in the same direction as the runner rotation.

- At some loads, a cavitating rotating vortex rope with helical shape can be observed.

- At loads above BEP, the direction of the tangential flow is in opposite direction of the runner rotation.

- At even higher loads, this results in a cavitated vortex core.

The part load vortex rope lead to forces fluctuating radially in the draft tube. This may cause vibrations in the system, and fatigue after a while. At some hydropower plants, the rotating vortex rope is so strong that it results in a pressure fluctuation which can propagate upstream the runner, creating mass flow fluctuations in the waterway. These fluctuations will increase elastic pressure waves. And if they coincide with resonance frequencies in the system, they can cause major fluctuations. The overload vortex core may cause mass flow fluctuations that can propagate through the entire waterway, causing power from the unit to fluctuate.

Vortex shedding

Von Kármán vortex shedding comes from unsteady flow separation off bluff bodies in a fluid stream and creates alternating low-pressure vortices on the downstream side of the body [34]. As a consequence, the body is subjected to an oscillating force perpendicular to the flow direction. Such vortices are one of the components of the guide vane wake, and is also known to result in severe noise from Francis runner blade trailing edges.

2.4.3 Reduction of turbine lifetime

Turbine components experience individual wear and tear during operation and the sustainability of these components may vary on type of loads they are experiencing. Main causes for turbine damage are fatigue, material defects, cavitation, and erosion, and these are well known issues for high head turbines due to high pressure and the pressure variation under dynamic load. Even though each unit is designed with a sufficient margin of safety to withstand normal stresses, high vibrations and dynamic stresses result in gradual development of cracks. In Francis runners, fatigue cracks tends to occur either relative early in life or after decades of operation. The failure mechanism is said to be a combination of LCF and HCF [27]. LCF originates from start-stop cycles, which can propagate fatigue cracks from manufacturing defects or initiate fatigue cracks at areas of high stress concentration. With rotational speed up to several hundreds RPM, the amount of vibration or HCF cycles caused by wakes behind the stay- and guide vanes increases to many millions per day. Consequently, when a crack has reached the fatigue crack growth critical size with respect to HCF loading, it may cause catastrophic failure very fast compared to the design life of the turbine runner. During steady state, several analyses have shown that the largest stresses appear where the blade is fixed to the hub or shroud near the trailing edge [27] [35] [18]. At this T-joint geometry, the level of stress and strain is further intensified due to notch effects. They are thereby the most critical locations for fatigue. Figure 2.9 presents statistics of cracks in Francis runners during the last 50 years collected from 368 Francis aggregates. It shows a clear improvement from the 1960s to the 1990s due to upgrades in design techniques. However, the amount of runners which have experienced cracking have increased over the last 20 years. The reasons for this is most likely that the runners are not designed to withstand the dynamic loads exerted on them during frequent variations in operation.
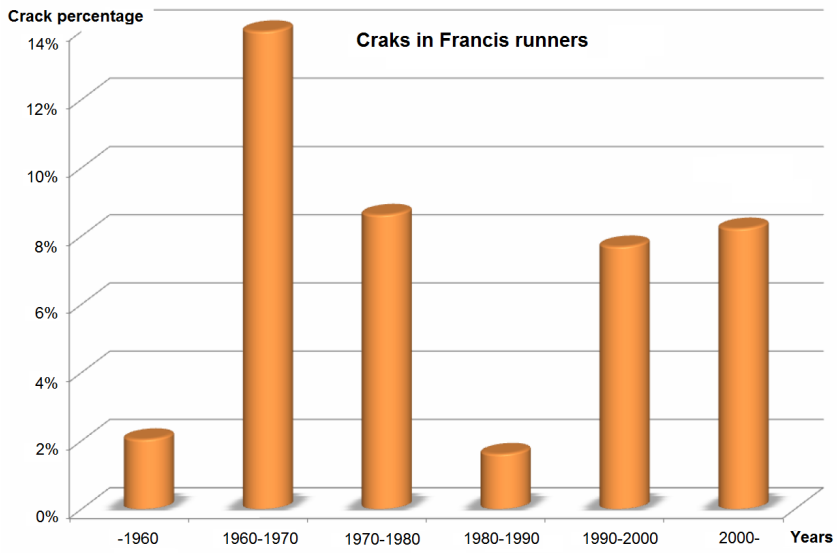
Figure 2.9: Statistics of cracks in Francis runners from 1960 to 2000 [22]

Chapter 3

Investigation tools

Experimental measurements of transients combined with a numerical analysis can provide reasonable research outputs together. Detailed experiments on transients are often limited due to the risk of damaging the machine. Therefore, a necessary set of experimental results can be used for validation of a numerical model, and further analysis can be carried out numerically. The uncertainty of the numerical results will increase or decrease with increasing or decreasing deviation from the nearest known physical model.

3.1   Model testing

On-site testing can be complicated and costly, and most prototype machines are too large to be tested in a laboratory. Therefore, it is very valuable to have the ability to perform tests on downscaled models of prototypes. It gives a greater flexibility to do repeated measurements at different operation points. For model testing of hydraulic turbines, an international standard IEC 60193 have been developed which is used as guidelines for measurements, calibration, and uncertainty analysis [42]. Prior to a model test, calibration of measurement equipment is necessary to make sure that the readings from the instrument are consistent with other measurements, to determine the accuracy of the instrument reading, and to establish if the instrument can be trusted. The resulting uncertainty in a measurement is a numerical estimate of the dispersion of values that could reasonably be attributed to the quantity [6]. It provides the quality of a measurement and offer the opportunity to assess and minimize the risks and possible consequences of bad decisions [6]. Further information about calibration and uncertainty analysis can be found in Appendix C.

3.1.1 Sensor fundamentals
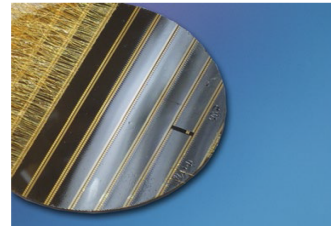
Pressure measurement

A pressure measurement can be described as either static or dynamic, and also by the type of measurement being performed where one can distinguish between three types: absolute, gauge, and differential [13]. Pressure sensors, or transducers, have a sensing element of constant area and respond to force applied to this area by the fluid pressure. The force deflects a bellows, diaphragm, or Bourdon tube. In turn, these deflections, tensions, or strains are transformed to electrical outputs proportional to the pressure through a transduction method. Common outputs are mV, V, mA, and frequency.

Strain measurement

The most common way to measure strain is with a strain gage, a device whose electrical resistance varies in proportion to the amount of strain in the device [14]. The resistance change occurs during all conditions of static and dynamic strain. Usually, the magnitude of measured strain is very small and is therefore often expressed as micro strain ($\epsilon \cdot 10^{-6}$). This is also the reason for why strain gages almost always are used in a bridge configuration with a voltage excitation source.

(a) Pressure transducer   (b) Strain gage

Figure 3.1: Measurement sensors

3.1.2 Discrete sampling and sampling rate

Digital data-acquisition systems record signals at discrete times, resulting in a deduction of actual measured behaviour between samples. The rate of the measurements is called the sampling rate. By choosing a poor sampling rate, the results can turn out misleading when analysing time-varying data. Information from the original signal can be lost, and unwanted components can appear during the reconstruction of the signal. It is therefore important to choose a fitting sampling rate based on which result sizes that one wants to analyse and which rate the sensors being used are able to perform at.

3.1.3 Filtering and smoothing of data

A moving average filter smooths the given data by replacing each point with the average of the neighbouring data points within a specific range [8]. The response of the smoothing is calculated by the difference equation,

$$y_s(i) = \frac{1}{2N+1}[y(i+N) + y(i+N-1) + ... + y(i-N)] \qquad (3.1)$$

where $y_s(i)$ is the smoothed value for the ith data point, N is the number of neighbouring data points on each side of $y_s(i)$, and 2N+1 is the span.

Savitzky-Golay filtering is a generalization of the moving average method. The filter coefficient are derived by performing an unweighted linear least-square fit using a polynomial of a certain degree. A high degree polynomial makes it possible to achieve a high level of smoothing without attenuation of data features. The method is very effective for frequency data since it preserves the high-frequency components of the data, but it can be less successful than a moving average filter at rejecting noise.
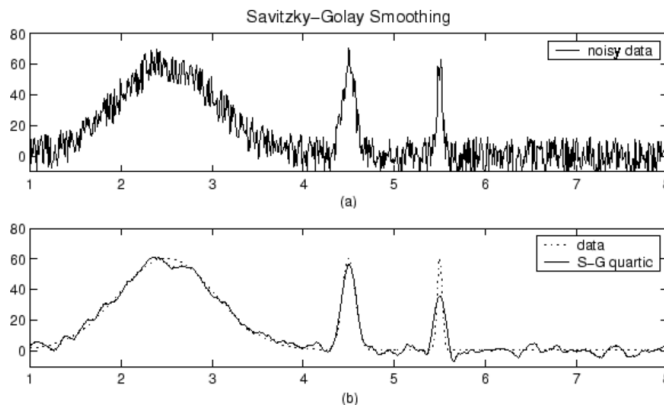
Figure 3.2: Attempt at smoothing data using the Savitzky-Golay method [8]

3.2 Numerical analysis

As the computational power of computers increases, the application of high-end numerical methods continues to grow. CFD has emerged as a reliable tool due to its great accuracy and flexibility in simulating various and complex three-dimensional (3D) flow phenomena. It has become a standard method to evaluate the feasibility of hydro turbines, and minimize much of the time and money spent for experimental investigations. In combination with FEA, CFD can be used to investigate fluid-structure interaction, which have shown to be a crucial analysis for risk reduction

27

during the design process of turbines. FSI problems play prominent roles in many scientific and engineering fields, yet a comprehensive study of such problems remains a challenge due to their strong non-linearity and multidisciplinary nature.

3.2.1 Computational fluid dynamics

Computational fluid dynamics is the science of predicting fluid flow, heat and mass transfer, chemical reactions, and related phenomena by the means of computer-based simulation. The most common CFD technique used in commercially available programs is the finite volume method [17]. It has an advantage in memory use and speed for major problems, turbulent flows, higher speed flows, and source term dominated flows. The finite volume procedure starts with dividing the regions of interest into small control volumes. Integration of the governing differential equations of fluid flow (the Navier-Stokes equations, the mass and energy conservation equations, and the turbulence equations) over the set of control volumes, in additions to application of the divergence theorem, follows. To evaluate the derivative terms, values at the control volume faces are needed. The result is a set of linear algebraic equations, one for each control volume, which are further solved iteratively or simultaneously. Turbulence modelling is a key issue in the majority of CFD simulations. Most engineering applications are turbulent and therefore require a suitable turbulence model.

ANSYS CFX

ANSYS CFX is a high-performance CFD software tool based on the finite volume method that gives out accurate and reliable solutions across a wide range of CFD and multi-physics applications. It is known for its outstanding robustness, accuracy and speed when it comes to rotating machinery such as pumps, fans, compressors, and turbines [4]. The software have been applied to solve a variety of fluid problems for over 20 years.

3.2.2 Computational structural mechanics

Structural mechanics is computation of deflections, deformations and internal forces or stresses within structures, either for design purposes or performance evaluation of existing structures. The finite element method is the dominant discretization technique in structural mechanics, where partial differential equation (PDE) problems are translated into a set of linear algebraic equations for steady state problems and a set of ordinary differential equations for transient problems [1]. The basic method involves decomposition of the domain into non-overlapping elements of simple geometry. The response of each element is expressed in terms of a finite number of degrees of freedom characterized as the value of an unknown function or functions, at a set of nodes. Systematically recombination of all elements at the nodes, thus forming a global system of equations, follows for the final calculation of the model

solution. FEM is a good choice for solving PDEs over complicated domains when the domain changes, when the desired precision varies over the whole domain, or when the solutions is missing smoothness.

ANSYS Mechanical

ANSYS Mechanical is a FEA tool that enables the user to analyse complex models and solve advanced mechanical problems. It is used for structural analysis, including linear, non-linear and dynamic studies [5]. Both steady and transient problems can be solved in Mechanical. A static analysis is used for static loading conditions, and non-linear behaviour such as large deflections, large strain, contact, plasticity, hyper-elasticity, and creep. A dynamic analysis includes mass and damping effects. In ANSYS, one can distinguish between three different dynamic analyses: modal, harmonic and transient dynamic.

3.2.3   Fluid-structure interaction

Fluid-structure interaction is a multi-physics coupling between the laws that express fluid dynamics and structural mechanics. This phenomena is characterized by stable or oscillatory interactions between a deformable or moving structure and an internal or surrounding fluid flow. When a fluid flow encounters a structure, stresses and strains appear in the solid body, which are forces that can lead to permanent deformations. Dependent on the pressure and velocity of the flow and the material properties of the structure, these deformations can be very large or quite small [7]. If the deformations of the structure are small and variations in time are slow, the behaviour of the fluid will not be largely affected by the deformations, and the focus can be on the resultant stresses in the solid parts (one-way FSI). However, if the variations in time are fast, pressure waves can appear in the fluid even for small structural deformations. For large structural deformations, the velocity and pressure fields of the fluid will change as a result, and the problem needs to be treated as a bidirectionally coupled multi-physics analysis (two-way FSI).

ANSYS software provides several ways to perform a FSI simulation. One way is to combine CFX and Mechanical through ANSYS Workbench. When dealing with an unidirectional coupling (one-way FSI), the dominating field can be simulated without considering the other physical field. As for transient fluid flow through a Francis turbine, it can be simulated without considering the structural motion and without significant loss of accuracy. The transient pressure distribution from the CFD analysis can then be used as surface load for the structure dynamic analysis.

ACT Transient FSI

ACT Transient is a numerical method that can be used to conduct a one-way FSI simulation in ANSYS. The method is an advantage when the work is shared between

two persons, since the fluid and structural analyses can be performed on separate computers. It does not create one giant project with enormous amounts of data, but instead the CFD calculation is closed and is a pure one-way coupling. Three data files are created for result transfer to ANSYS Mechanical containing the mesh, the step end times and the nodal load values of each time step [26]. This enables the user to interpolate transient CFD results from the CFD mesh to the FEM mesh in each time step of a transient structural analysis. To get a consistent workflow the extension automatically creates the same time step settings as used in the underlying CFD simulation. The CFD results from one calculation can be used for many Mechanical runs. However, the downside with using this numerical method is that the viscous forces/shear forces are not accounted for in the analysis.

3.2.4 Numerical errors and uncertainties

When identifying and validating modelling and simulation results, evaluation of errors and uncertainties is very important. Error is defined as a recognisable deficiency in a numerical model that is not caused by lack of knowledge, while uncertainty is defined as a potential deficiency in a numerical model that is caused by lack of knowledge [50]. The amount of errors and uncertainties decides the quality of the results obtained. One can distinguish between different errors and uncertainties based on how they occur:

Causes of errors:

- Numerical errors and round of errors, discretization errors and iterative convergence errors

- Coding errors and mistakes or "bugs" in the software

- User errors and human errors through incorrect use of the software

Causes of uncertainties:

- Input uncertainties and inaccuracies due to limited information or approximate representation of geometry, boundary conditions, material/fluid properties, etc.

- Model uncertainties and discrepancies between real flow and the numerical model due to insufficient representation of physical or chemical processes, or due to simplified assumptions in the modelling process

Mesh grid

The solution of numerical models is dependent on the mesh grid. It is therefore always recommended to adapt the grid until the solution is independent of the mesh. However, this is sometimes difficult due to limited computational resources.

When grid independence is obtained, the most coarse and independent mesh should be chosen for further analysis.

When dealing with a CFD model, fine grid resolution is required close to the walls to obtain an accurate solution for the boundary layer. The non-dimensional wall distance value y+ defined in Equation (3.2) is used as a requirement, where u_r is the friction velocity at the nearest wall, y is the distance from the node to the nearest wall, and ν is the local kinematic viscosity [18]. Different turbulence models have different y+ requirements, and for example, the k-epsilon model uses 30<y+<300.

$$y+ = \frac{u_r \cdot y}{\nu} \tag{3.2}$$

As a general rule of thumb, it is desirable with fine grids in areas of interest. And elements with very slender proportions should be avoided.

Time step

A sufficient time step is important in transient CFD simulations. The time step should be small enough to capture the transient phenomena occurring and small enough for the simulation to converge. Devices with many blades should have small times step size to resolve the interaction between the blades and surrounding, non-rotating geometry. However, a small time step increases the complexity of the simulation and needs more time and computer resources to achieve a full solution.

Chapter 4

Facilities and methods

Pressure and strain measurements on a Francis turbine model and a FSI simulation of the same turbine have been carried out to investigate how variable rotational speed affect the load pattern and corresponding stresses in the turbine runner. The FSI analysis was performed in the software program ANSYS by combining ANSYS CFX and ANSYS Mechanical. Results from the laboratory measurements were used as inputs in the CFD and FEM analyses, and further used for validation of the solutions.

4.1 The Waterpower Laboratory

The Waterpower Laboratory at NTNU is built around a main piping system and include three test rigs: test rig for Francis, Kaplan and reversible pump turbines, test rig for Pelton turbines, and test rig for micro-, mini-, and small turbines [46]. There are installed two pumps in the basement that operates separately, in parallel or series to achieve a broad area of volume flow and head. Each pump is driven by a 315 kW motor and a frequency converter [2]. Available pumping power is 700 kW and the maximum flow rate is 1.1 m^3/s. It is possible to obtain different run conditions by utilizing different piping systems, and the different operating modes include both open and closed loop. The closed loop system can be pressurized to maximum 100 m, while the open loop system has a maximum head of 16 m. A section of the open loop system with the Francis test rig can be seen in Figure 4.1.

A lower reservoir is situated under the floor in the laboratory and has a capacity of 450 m^3. An upper reservoir is situated on the top floor of the building and consists of two large tanks with an u-shaped channel between them. This is used when running an open loop. The laboratory also have two main tanks, one high pressure and one low pressure tank, situated upstream and downstream of the Francis rig, respectively. The high pressure tank is used as a pressure reservoir when running

closed and open loop, dampening pump effects and delaying the influences on the turbine from changes in pump speed. The tank may also function as an air cushion when running the rig from the upper reservoir. The low pressure tank acts as the tail water in the system.
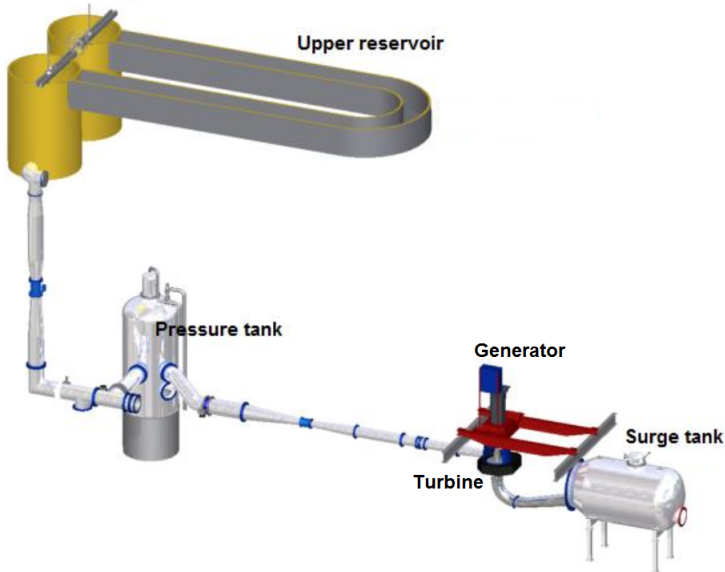

Figure 4.1: A section of the open loop system at NTNU

4.1.1 Francis test rig

A model of Tokke hydropower plant is installed as a part of the Francis test rig in the laboratory. The arrangement from the spiral case to the draft tube is set to be a true model of the hydropower plant, and the model is scaled down to 1:5.1 of the prototype [2]. Cross sectional areas at the turbine inlet and outlet sections are 0.0872 m^2 and 0.236 m^2 respectively, while the reference diameter of the model runner is 0.349 m [49]. Additional dimensions of the model runner designed by the Waterpower Laboratory can be found in Figure 4.2. The Francis turbine is installed with a vertical shaft and a DC generator of 352 kW. It is equipped with 14 fixed stay vanes, 28 adjustable guide vanes and an elbow-type draft tube. The runner consists of both half and full-length blades, and sum up to 30 blades in total. They are twisted 180 degrees around from inlet to outlet, and the blade thickness at the trailing edge is 3 mm [11].
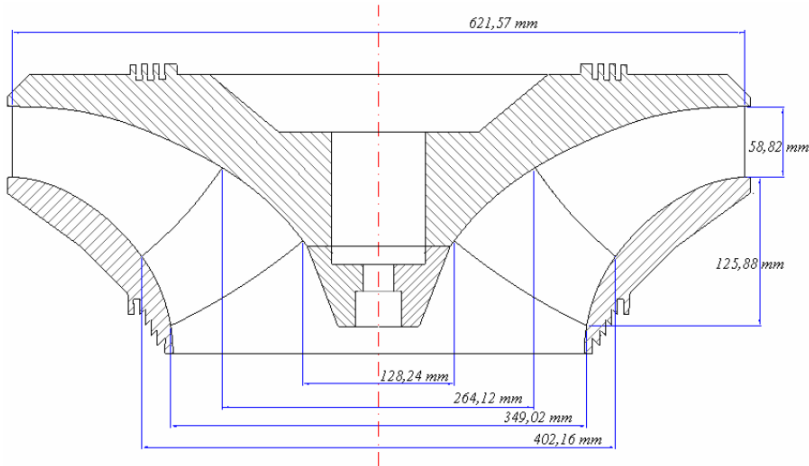
Figure 4.2: Dimensions of the Tokke model runner

The Francis runner is constructed out of different bronze materials, where the blades are made of cast tin-bronze JM 3, while hub and shroud are made of bronze JM 7 [39]. The JM 3 alloy consists of 88% copper and 12% tin, and the JM 7 alloy consist of 80% copper, 10% aluminum, 5% iron, and 5% nickel [12]. Properties of the two materials are found in Table 4.1. Both are well suited for construction of turbine runners. By adding tin in the alloy, one gets a harder and more durable bronze. Tin-bronze is resistant to corrosion in water, and is often used in marine industry. Aluminium bronze alloy is characterized by good impact strength, excellent corrosion resistance to acids and salt water, and is malleable. The main concern when manufacturing the runner blades was to make sure they would withstand different temperatures and pressures, and thereby not deform during operation. In addition to financial reasons, tin-bronze was chosen as material based on this requirement.

Material	JM 3	JM 7
Density [g/m^3]	8.8	7.6
Yield strength [MPa]	> 150	> 260
Tensile strength [MPa]	> 270	> 590
Young's modulus [MPa]	10^5	1.1×10^5
Poisson's ratio	0.34	0.32
Thermal conductivity [W/m°C]	50	65
Resistivity [nΩm] (20°C)	200	190

Table 4.1: Mechanical properties of the Tokke runner [12]

4.1.2   Generator parameters

The Francis test rig includes a IGG6258 generator manufactured by Siemens [37]. It has the following technical parameters:

Parameter	Value
Rated speed [rpm]	1560
Rated armature voltage [V]	420
Rated output [kW]	352
Rated torque [Nm]	2150
Maximum field weakening speed [rpm]	2000
Rated current [A]	890
Efficiency [%]	92
Maximum speed [rpm]	2600

Table 4.2: Technical generator parameters [37]

The output wire from the generator is connected to a rectifier cabinet/DC converter of type Simoreg 6RA70 DC Master, also manufactured by Simens [44]. Next, the converter is connected to the power grid, which supplies and demands power to and from the generator to maintain the chosen operating point. The rotational speed of the generator is fixed by the converter.

4.2   Laboratory experiment

The Francis test rig was operated with an open loop water circuit to obtain a condition similar to the prototype without significant variation of the effective head during transients. Risk assessment of the experiment is found in Appendix A. A script constructed in the software program LabVIEW from National Instruments (NI) made it possible to control the runner speed while the guide vane angle was held constant. Pressure at several points in the turbine and strain in one of the runner blades were measured. Wiring of the total laboratory set-up was completed by master student Einar Agnalt.

4.2.1   Instrumentation

Pressure sensors

Recently, five new pressure sensors were flush-mounted into the hub of the Tokke model runner for better durability during operation of the rig. They are placed right in the middle of two hydraulic channels. The placement, with sensor notations, can be seen in Figure 2. Pressure sensor PT11 is mounted close to the inlet of the

runner and sensor PT14 close the outlet. Likewise, sensor PT12 is placed upstream the splitter blade and sensor PT13 downstream. The fifth sensor, PT10, is mounted in the neighbouring hydraulic channel. Pulsations from RSI, the change in channel cross section, and phase difference in pressure pulses will be accounted for when the pressure sensors are placed like this.
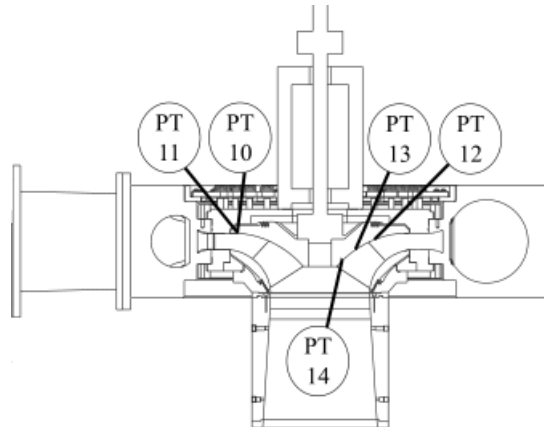

Figure 4.3: Onboard pressure sensors mounted into the runner hub

Two pressure sensors, PT20-21, were flush-mounted in the vaneless space between the guide vanes and the runner blades. Another four pressure sensors, PT30-31, were mounted into the draft tube cone. The latter pressure sensors are piezoelectric, suitable for measuring dynamic curves or pulsations. Figure 3 illustrates were all these sensors can be found on the turbine, and the placement is set to register pressure pulsations from RSI and draft tube surge.
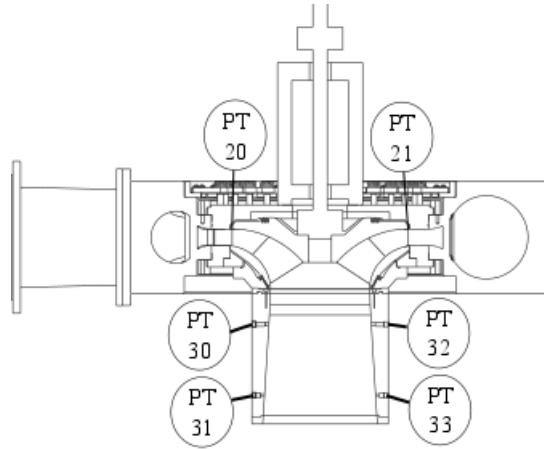
Figure 4.4: Pressure sensors in the vaneless space and in the draft tube cone

In addition, three pressure sensors, PT01, PT02, and PT03, were flush-mounted to the penstock, the inlet of the spiral casing, and the draft tube outlet, respectively.
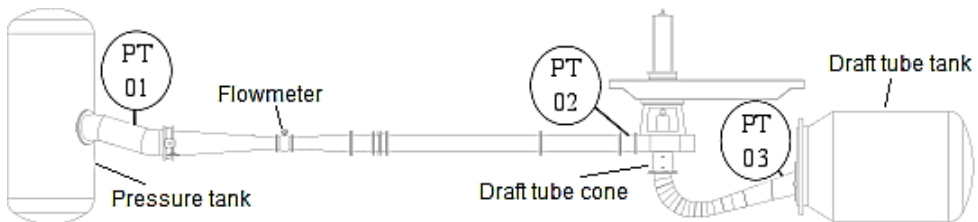

Figure 4.5: Pressure sensors in pipe line

Notation	Transducer	Type	Range
PT10-14	Kulite XTM-190S(M)	Piezoresistive sensor	0-3.5 bara
PT20-21	Kulite XTL-190(M)	Piezoresistive sensor	0-10 bara
PT30-33	Kistler 701A	Piezoelectric sensor	0-250 bar
PT01-03	Kulite HKM-375(M)	Piezoresistive sensor	0-1.7 bara

Table 4.3: Measuring equipment

Operation point sensors

Sensors recording operating conditions are placed around on the Francis test rig. A magnetic flow meter, FT40, is mounted at the turbine inlet pipeline to measure the discharge to the turbine. Pressure sensor PT40 is used to measure the pressure at the

38

casing inlet, while pressure sensor PT41 is used to measure differential pressure (Δ p) across the turbine. Other sensors are included to register the generator torque (WT40), friction bearing on shaft (WT41), RPM on shaft (ST40), and angle of guide vane (ZT40). The ST40 measuring system contains a photocell (in the form of an optical fork) and a circular disc with one cut fixed to the generator shaft, and measures 1024 pulse per rotation.
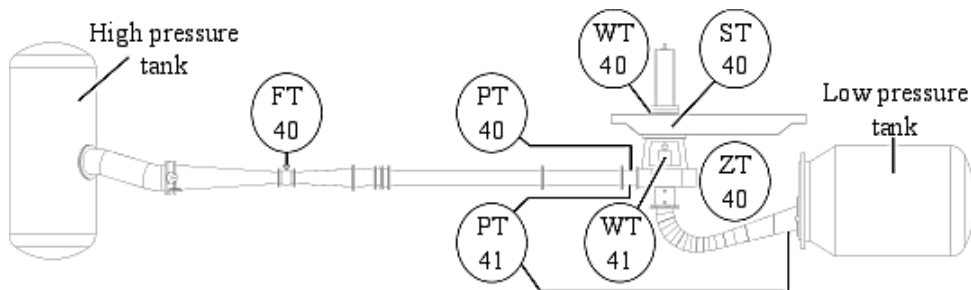

Figure 4.6: Sensors for calculating running point

Notation	Instrument	Type	Range
FT40	Krohne Aquaflux IFS 4000	Flow meter	0.15-500 l/s
PT40	Fuji Electric FHCW36W1-AKCAY	Diff. pressure transducer	0-1000 kPa
PT41	Fuji Electric FHCW36W1	Diff. pressure transducer	0-1000 kPa
WT40	Hottinger Z6FC3	Load cell	0-2000 Nm
WT41	Hottinger Z6FC3	Load cell	0-16 Nm
ST40	OPB 960T51	Optical fork	1024 pulse
ZT40	Stegman AG612	Angle transducer	1 pulse

Table 4.4: Measuring equipment [37]

Strain gage

A semiconductor strain gage was used to measure strain in one of the full-length runner blades. This is placed on the pressure side of the runner blade, up towards the joint between blade and hub, as pointed out in the Figure 4.7. This position is based on earlier FEA results showing where the highest stresses usually occurs. It have been glued on with a quick-drying glue, and further covered with the same glue to assure a reliably working strain gage. The attachment method is temporarily, and should be improved before similar measurements shall be conducted in the laboratory.
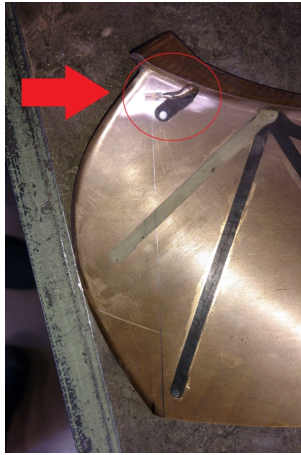
Figure 4.7: Strain gage attached to one of the runner blades

4.2.2 Calibration

Calibration of the instruments used in the experiment were performed before the measurements were conducted. This included calibration of the magnetic flow meter, the weighing tank, generator- and friction-torque measurement sensors, and pressure sensors. In the Waterpower Laboratory, pressure head is calibrated with a manometer, flow by weighing and torque by weights on the level arm. The set up for the rotational speed measurement system does not need calibration since the only value that is measured is time. Achieved calibration reports are found in Appendix D. Uncertainties from the calibrations were further used to perform an uncertainty analysis, which is presented in Chapter 5.

The dynamic pressure transducers mounted in the draft tube cone were not calibrated due to lack of dynamic calibration equipment. Instead, factory calibration data was used. Furthermore, calibration constants for the strain gage had to be theoretically calculated. Output voltages with corresponding strain were plotted and fitted with a calibration curve created by the use of a third degree function. The estimated uncertainty of this calibration curve is 0.25%. Because the strain gage only has been theoretically calibrated, the absolute values provided by the measurements should be handled with caution.

4.2.3 Variation in rotational speed

To control the rotational speed of the turbine runner, a script was designed in Lab-VIEW. This script can be further studied in Appendix F. It uses a single sinusoidal oscillation given by Equation (4.1), that is suppose to represent a quick decrease in

turbine speed caused by a variation in grid frequency.

$$y(t) = A \cdot [\frac{1}{2}sin(\pi ft + \phi) + \frac{1}{2}] + (y1 + A) \qquad (4.1)$$

A is the amplitude of the runner speed oscillation, f is the ordinary frequency of the oscillation, and ϕ specifies where in its cycle the oscillation is at t = 0.
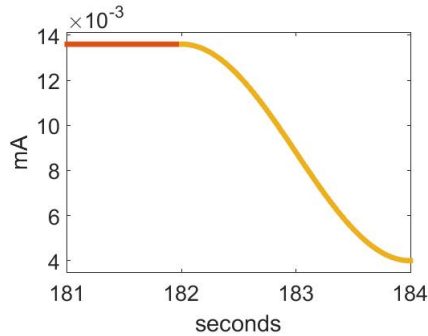

Figure 4.8: Variation in RPM

The LabVIEW values were transferred to a current output card NI 9265, connected to a NI cDAQ, which created a 4-20 mA signal. This signal was sent to the "Francis Generator signal"-box (located near the Francis runner in the laboratory) by connecting cables to the "disturbance RPM" input channels. The box further sends the signal down to a rectifier cabinet/DC converter in the basement. Then, DC power is transmitted up to the turbine generator, deciding how the generator should act. Figure 4.9 describes the set-up of the system in the laboratory.
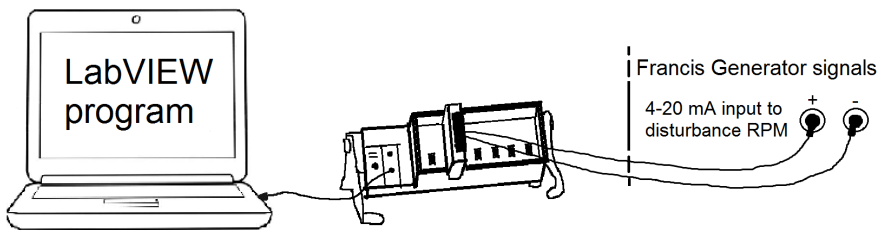
Figure 4.9: Schematic representation of RPM disturbance system

The sine curve started at 273 RPM and increased up to the synchronous speed of 333 RPM. To stabilize the system characteristics, operation at this point was run for approximately three minutes before the runner speed was decreased down to 273 again. Only the performance during the decrease was of interest for this master thesis. The decrease of 60 RPM had a time period of 2 seconds, which was limited

41

by how quick the laboratory machines can be run and how long time it would take to simulate the same change in ANSYS. The generator in the Waterpower Laboratory have a maximum torque limit of 2150 Nm at stationary operation, and can tolerate a change of +10% to -20% in rotational speed during a short time period.

4.2.4   Data acquisition

Measurement data were acquired through LabVIEW and a NI cDAQ 9178 with eight modules, including:

- Five NI 9239 modules connected to PT10-14, PT30-33, FT40, PT40-41, WT40-41, and ZT40.

- Two bridge NI 9237 modules connected to PT20-21 and PT01-03.

- One NI 9401 module connected to ST40.

Due to the mounting of new pressure sensors in the runner, a slip-ring have been installed on the turbine shaft to ensure synchronous sampling of both rotating and stationary domain. The onboard sensors, which are wired through the slip ring, are connected to an amplifier to increase the voltage range going into the module. The draft tube pressure sensors are connected to a converter that transforms the signal from resistance per bar to voltage per bar.

A new logging program was made in LabVIEW with help from PhD Candidate Carl Bergan in order to sample all signals simultaneously. Every signal, except from the rotational speed, was sampled at 5 kHz. In total, 10 repetitions of the same transient measurement were carried out to be able to estimate the random uncertainty. The values written to file were un-calibrated voltage values which afterwards were manipulated to give a qualitative representation of the behaviour of the measured quantities.

4.3   Computer simulation

All the geometries used in the numerical analyses were drawn in the CAD program PTC Creo. The geometries represents a true copy of the Tokke turbine model in the Waterpower Laboratory. The FSI analysis is a combination of a transient fluid analysis of the flow passage done in ANSYS CFX and a transient structural analysis of the turbine runner done in ANSYS Mechanical. It is a one-way interaction, meaning that deformations in the structure caused by the fluid were not taken into account in the flow analysis. To run the simulations, one of NTNU's supercomputers was used, providing a quicker process.

4.3.1 CFD

A transient and turbulent CFD simulation was perfomed in ANSYS CFX by Postdoc. Fellow Chirag Trivedi. Since it was conducted by another person than the author of this thesis, only the basics of the analysis will be explained in the upcoming sections. Further explanation can be found from the Francis-99 workshop 2 and corresponding papers [2].

Geometry

The CFD simulation of the Tokke turbine model included the wetted surfaces of the spiral casing, stay vanes, guide vanes, runner vanes, and draft tube. The CAD model can be seen in Figure 4.10. When including the whole flow passage of the Francis turbine, it is easier to obtain accurate predictions of the pressure distributions and pressure pulsations on the runner blades. The turbine model was divided into four domains: stationary domain 1 consisting of the spiral casing, stationary domain 2 consisting of the guide vanes, rotating domain consisting of the runner, and stationary domain 3 consisting of the draft tube. These domains were connected by using appropriate interfaces.
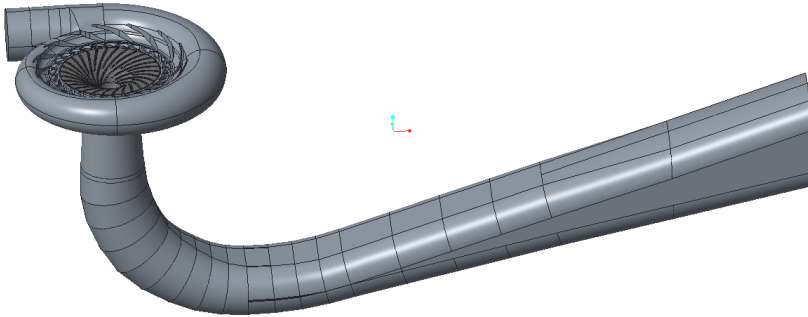

Figure 4.10: Wet CAD model of the Tokke turbine

Labyrinths seals were not included due to the fact that modelling of fluid flow in the labyrinth seals require very fine meshing and substantial computational power. The flow leakage losses in the turbine are thereby not investigated through CFD.

Mesh

The mesh was prepared using ICEM CFD with a tolerance $\geq 10^{-4}$. On all the domains, a hexahedral mesh grid was created by using 3D structured multi-blocks. The total number of elements is 8128515 for the complete turbine, with 1 338 645, 2 579 790, 3 477 600, and 732 480, for the spiral casing, runner, guide vanes, and draft

tube, respectively. Fine mesh was created close to the boundaries and in complex passages of the turbine.

Fluid properties and boundary conditions

An incompressible Newtonian fluid was defined as the medium, with density, viscosity, and temperature consistent with water properties. Buoyancy Model was set to "Non Buoyant" and Reference Pressure to 1 atm. The standard $k - \epsilon$ model was used, which is one of the most common turbulence models. It includes two extra transport equations to represent the turbulent properties of the flow: the turbulent kinetic energy, k, and the rate of dissipation of kinetic energy, epsilon. The model applies the y+ method where a logarithmic overlap law is used to describe the boundary layer nearby the wall. The Turbulent Wall Functions were set to "Scalable" for all the domains. In addition, all the walls were defined with no-slip and smooth wall boundary conditions.

Pressure at the inlet of the spiral casing and the runner speed were defined as boundary conditions by using average measurement values from one of the experimental measurements. Instead of using a sine curve to describe the runner speed, a straight line was created between the two speeds of 333 RPM and 273 RPM. This was mainly to simplify the simulation, however, it creates a small difference between the results from the laboratory and the results from the simulation.

Time	T [s]	Casing inlet pressure [kPa]	Runner speed [rpm]
Start time	0	135	333
Transient start time	1	135	333
Transient end time	3	133	273
End time	4	133	273

Table 4.5: Boundary conditions

It needs to be mentioned that the pressure boundaries in the table above were taken from a single measurement performed early in the semester and reflect pressure results from a RPM variation over 3 seconds. In contrast, the transient time domain in the CFD simulation is 2 seconds. This was caused by incorrect information flow between the different persons involved in this thesis. The CFD simulation had already started running with these boundaries when the error was detected, leading to conduction of new laboratory measurements with a time domain of 2 seconds.

Time step size

In this case, the transient component in the simulation is the turbine runner, thus the time step is defined through the runner speed. The time step size is given

by Equation (4.2), where the value 0.1592 represents the conversion factor between radians and revolutions. Each time step is equivalent to 0.5° of the runner revolution, and results were recovered every 100th time step during the CFD simulation.

$$timestep = \frac{\frac{1}{runnerspeed} \times 0.1592}{360} \qquad (4.2)$$

Validation of CFD model

A validation of the CFD model was performed to check if the model is adequate for practical purposes. This was done by comparing the results with the available experimental data to check if the reality was represented accurately enough. Plots from different pressure sensors were compared to pressure plots from specific coordinate points in the CFD model. These coordinates, with related location uncertainties, can be found in Appendix B and are illustrated with red crosses in the figure below.
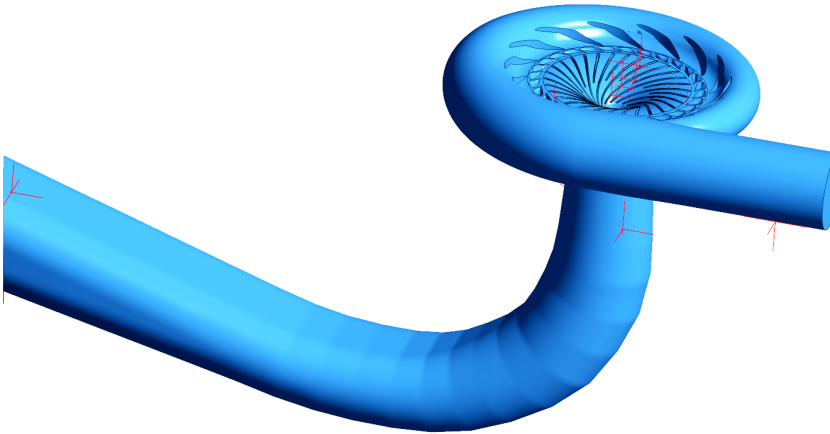

Figure 4.11: Locations of pressure sensors in the CFD model

4.3.2 FEA

The structural analysis of the turbine runner was performed in ANSYS Mechanical through the Transient Structural model system. The runner stand out as the most vulnerable component since it is exposed to many sources of dynamic excitation. To avoid failure, it is therefore of great interest to predict its dynamic behaviour.

Geometry

The 3D model consists of hub and shroud with labyrinth seals, cone, full length runner blades, and splitter blades. It is shown in Figure 4.12. By using the whole runner geometry, the influence of all the components and the neighbouring blades will be accounted for in the transient analysis. Holes for bolts were removed to simplify the model, assuming that this would not significantly influence the results. In ANSYS DesignModeler, all the parts were connected by creating one multibody part, which ensures connection between all parts without using separate connection regions.
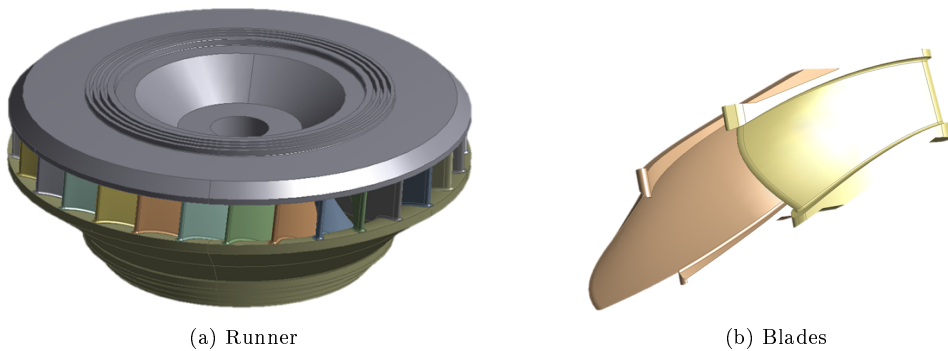

(a) Runner　　　　　　　　　　　　　　　　(b) Blades

Figure 4.12: Structural CAD model of the Tokke runner

A feature called Virtual Topology in Mechanical lets the user group faces and/or edges together, allowing to form virtual cells in order to reduce or improve surfaces. Instead of permanently changing the geometry, virtual cells were generated automatically with a low search intensity and then slightly modified. This provided nicer surfaces to work with when creating the mesh.

Material properties

A new material library was created under Engineering Data in ANSYS Workbench. JM 3 and JM 7 were characterized with the material properties from Table 4.1. Material selection for each structural part was done in ANSYS Mechanical. By using the correct material instead of using the default material "Structural steel", it creates an improved foundation to compare experimental results with the computer simulation.

Mesh

Since the author decided to create one multibody part, the runner parts share the same mesh nodes in the connecting regions. Tetrahedral shaped mesh elements were

created on all of the runner bodies as this provided the best possible solution for this specific model. On narrow faces, local sizing controls were implemented to decrease the size of the elements. It is important with a fine mesh grid on areas where high stresses are expected, like the fillets and trailing edge of the runner blades. Complex areas like the labyrinth seals also require small mesh elements to achieve a satisfying mesh quality. These areas were therefore targeted. The smallest element size used was 2 mm. Pinch Control were also inserted to repair a bad surface edge on the leading edge of the runner blades.

To be able to conduct a mesh independence test, several different mesh grids were created in separate modules. The Relevance and Span Angle centres were changed from Coarse to Medium, and the Advanced Size Function called Curvature was turned off and on to provide additional control over the global mesh sizing. Maximum element size was set to 7 mm. A list of the mesh grids included in the independence analysis are presented in Table 4.6. Stress probes, which outputs the specific stress of the point where it is placed, were attached to one blade to compare the quality of the mesh grids. Finer mesh grids than the one mentioned were created in the process, but had to be rejected due to time and computation limitations.

Mesh	# nodes	Functions applied
1	1 786 521	Coarse Relevance Center and Coarse Span Angle Center
2	2 024 838	Medium Relevance Center and Medium Span Angle Center
3	2 582 903	Medium Relevance Center and Medium Span Angle Center, in addition to a smaller element size for the blade, hub and shroud surfaces
4	3 526 317	Curvature, Coarse Relevance Center, and Coarse Span Angle Center

Table 4.6: Mesh independence test

Boundary conditions

To ensure that the structural 3D model acts the same way as the physical model, constraints and appropriate boundary conditions were applied to the runner. The boundary conditions implemented are listed below:

- Fixed support on the surfaces connecting the hub and the shaft

- Acceleration due to gravity (g)

- Variable rotational speed implemented as modified data from the laboratory log

The boundary condition Fixed support locks the displacement of the mesh nodes on the related surfaces and replicates the impact a shaft would have had on the

structure. Standard earth gravity defined by ANSYS was added in negative z-direction. Further, the same tabular data as used in the CFD analysis was used as transient rotational velocity. It was important that the velocity functions were equal for the two models to make sure that the pressure loads would map onto the correct surfaces at each time step. The rotational velocity (rotational inertia) and gravity (runner weight) together increases the load picture by imparting inertia force on the runner. Axial pressure forces on the outer hub, shroud and labyrinth seals were neglected from the analysis due to the complexity of the transient pressure distribution and insufficient information.

4.3.3 FSI

A one-way transient simulation was conducted. In contrast, a two-way FSI analysis is time consuming and require a huge amount of computer resources. With the current stiff materials in the Tokke runner, it is also possible that the deformations caused by the fluid pressure would not have had a large impact on the fluid flow behaviour.

The ACT Transient FSI method was applied since the work was shared between two persons, the author and Chirag Trivedi. First of all, the ACT extension had to be downloaded, installed and implemented into ANSYS. Further, macros were run via the CFD Post Macro calculator to create the CFD data files in the right format. Then a FSI surface macro was used to export surface pressures from the hub, shroud, blades and cone. In ANSYS Mechanical - Transient Structural, pressure was imported as a load through the ACT extension and mapped onto the corresponding surfaces of the structural runner model. Figure 4.13 presents an overview of the boundary conditions, including the surface pressure, imparted on the runner.
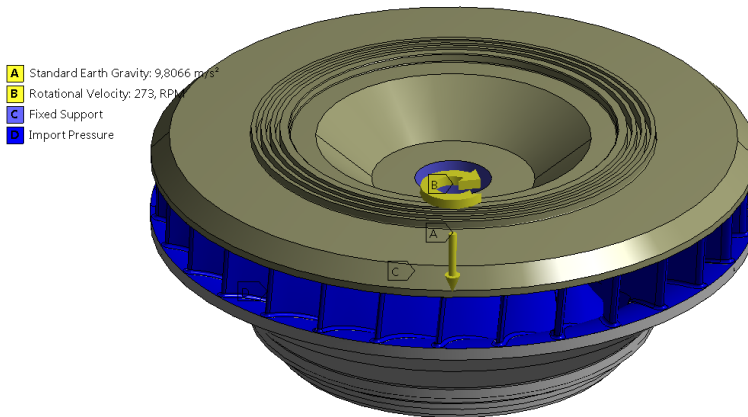

Figure 4.13: Conditions and loads on structural model

Equivalent stress and strain were inserted as solver outputs to analyse stresses and strain in the runner caused by fluid-structure interaction. In addition, different probes were added to extract results at specific coordinates and surfaces.

Validation of FSI

A validation of the FSI analysis was performed by comparing the results from the strain gage measurements with strain results from the computational model. Strain gage measurements are a powerful validation method because their results represent area integral measures of the effect of pressure fields onto the structure. Coordinate systems were added at the strain gage coordinates, which can be found in Appendix B. Then, a path was created between the two points and snapped to the nearest mesh nodes to follow the blade during rotation of the runner.

Chapter 5

Uncertainty analysis

The different sources of errors that contribute to uncertainty during model tests are listed in Table C.1 and Table C.2 in Appendix C. This chapter provides the most important uncertainties related to the results presented further on. The total uncertainties are calculated to give a picture of how trustworthy the laboratory results are. The experiment was repeated 10 times to be able to retrieve a standard deviation.

The author have chosen to present the uncertainties related to the pressure, torque and rotational speed measurements. Uncertainty analysis of the strain measurement is not included since the strain gage only was calibrated theoretically, and thereby lack information to perform a complete analysis. But as mentioned in subsection 4.2.2, the estimated uncertainty of the strain gage calibration curve is 0.25%.

5.1 Uncertainties in the calibrations

5.1.1 Static pressure transducers

The total systematic uncertainties of the pressure transducer calibrations were calculated with 95% confidence through the use of the calibration LabVIEW program in the Waterpower Laboratory. This uncertainty includes the randomness in the calibrated instrument during the calibration, systematic uncertainty in the instrument (dead weight manometer), and due to regression analysis to fit the calibration points to a linear calibration equation. The uncertainties are listed in Table 5.1 below.

Sensor	$\max(f_{p_{reg}})[\%]$	Sensor	$\max(f_{p_{reg}})[\%]$
PT10	± 0.4128	PT21	± 0.0527
PT12	± 0.3989	PT20	± 0.0396
PT13	± 0.3901	PT02	± 0.1942
PT14	± 0.3972	PT03	± 0.0488

Table 5.1: Total calibration uncertainties of pressure transducers

5.1.2 Torque

The uncertainties of the instruments used in the torque calibrations were not included in the calibration LabVIEW program, and thus the total calibration uncertainties have to be calculated theoretically. To calibrate the torques, weights calibrated by the Norwegian Metrology Service were applied.

- The systematic uncertainty in the weights used for the calibrations, f_{τ_W}, is taken into account by using the calibrated kilogram values instead of the stated kilogram values of the weights.

- **Generator torque**: The length of the torque arm was measured to be 0.9979 m. The related uncertainties of the shaft diameter, the rod, the calliper, and the band width, are assumed to be ± 0.5 μm, ± 0.5 μm, ± 5 μm, and ± 5 μm, respectively [44]. By combining the uncertainties one obtains $f_{\tau_{G_{arm}}} = \pm 0.0005\%$ as the systematic uncertainty in the length of the arm.
  Friction torque: The length of the torque arm was measured to be 0.1469 m. The related uncertainties of the shaft diameter, the calliper, and the block width, are assumed to be ± 5 μm, ± 5 μm, and ± 5 μm, respectively [44]. By combining the uncertainties, one obtains $f_{\tau_{F_{arm}}} = \pm 0.0042\%$ as the systematic uncertainty in the length of the arm.

- The systematic and random uncertainties in the instruments, f_{τ_c} and f_{τ_d}, are included in $f_{\tau_{reg}}$. The maximum uncertainties in the regression lines were $\max(f_{\tau_{G_{reg}}}) = 0.9298\%$ for a generator torque of 62.23 Nm and $\max(f_{\tau_{F_{reg}}}) = 6.1554\%$ for a friction torque of 0.9454 Nm.

Combining the listed uncertainties above gives the total random uncertainties of:

$$max(f_{\tau_{G_{cal}}}) = \pm\sqrt{+(f_{\tau_{G_{arm}}})^2 + max(f_{\tau_{G_{reg}}})^2} = \pm 0.9298\% \qquad (5.1)$$

$$max(f_{\tau_{F_{cal}}}) = \pm\sqrt{(f_{\tau_{F_{arm}}})^2 + max(f_{\tau_{F_{reg}}})^2} = \pm 6.1554\% \qquad (5.2)$$

These are the maximum uncertainties, and do not fully represent the actual uncertainties of the operating torque ranges.

### 5.1.3   Rotational speed sensor

The rotational speed measurement system is not calibrated since it is assumed to be accurate. However, there is a systematic uncertainty of $\pm 0.025\%$ linked to the rotational speed in the Waterpower Laboratory [42].

5.2   Uncertainties in the tests

Figure 5.1 illustrates how the 10 measurements were merged/synchronized together to find the average curve and related 95% confidence interval. This is done for all of the measurement results.
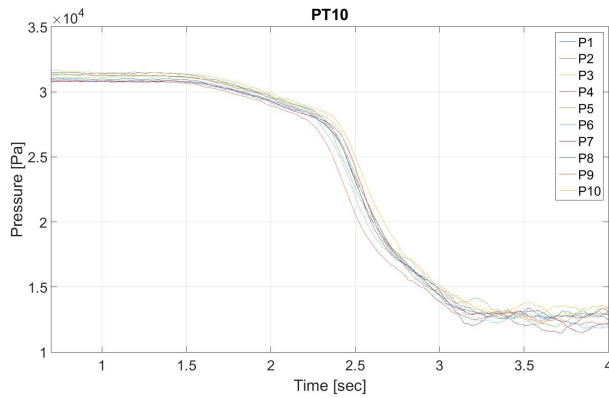
(a) Synchronized measurement results
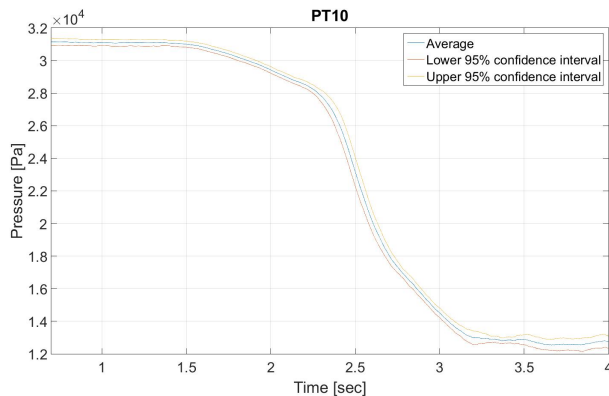
(b) Average measurement with 95% confidence interval

Figure 5.1: Confidence interval of repeated measurement

5.2.1 Static pressure transducers

- f_{p_g} is equal to $f_{p_{cal}}$, and is found in Table 5.1.

- f_{p_h} is caused by the drift of the output signal over time. This error is ignored here.

- f_{p_k} may be ignored since the calibrations of the static pressure transducers were conducted using the same data acquisition system planned for the experiment.

- f_{p_l} is found by using the 95% confidence interval for the logged data from the tests. The maximum random uncertainties during the test are presented in Table 5.2. A major part of this uncertainty may come from unsynchronized measurements in time.

Sensor	max(f_{p_l})[%], 0-1 s	max(f_{p_l})[%], 1-3 s	max(f_{p_l})[%], 3-4 s
PT10	±0.007	±0.012	±0.024
PT12	±0.015	±0.016	±0.017
PT13	±0.030	±0.024	±0.019
PT14	±0.090	±0.067	±0.057
PT21	±0.003	±0.004	±0.003
PT20	±0.002	±0.003	±0.003
PT02	±0.001	±0.001	±0.001
PT03	±0.045	±0.037	±0.032

Table 5.2: 95% confidence interval uncertainties

5.2.2 Torque transducers

- max($f_{\tau_{G_{cal}}}$)=±0.9298% and max($f_{\tau_{F_{cal}}}$)=±6.1554%

- The calibration from the manufacturer is assumed to be correct, and therefore is the uncertainty f_{τ_h}, caused by drifting of the output signal over time, ignored.

- None physical sizes exists, as the torque is given directly by the voltage signal from the weight cell. f_{τ_j} can therefore be ignored.

- f_{τ_k} may also be ignored since the conditions during the test were the same as during the calibration.

- max($f_{\tau_{G_l}}$) and max($f_{\tau_{F_l}}$) are found in Table 5.3.

Sensor	max(f_{G_l})[%], 0-1 s	max(f_{G_l})[%], 1-3 s	max(f_{G_l})[%], 3-4 s
WT40	±0.004	±0.005	±0.003
WT41	±0.022	±0.022	±0.023

Table 5.3: 95% confidence interval uncertainties

5.2.3   Rotational speed sensor

The maximum random uncertainty for the rotational speed measurements can be found in Table 5.4.

Sensor	$\max(f_{n_l})$[%], 0-1 s	$\max(f_{n_l})$[%], 1-3 s	$\max(f_{n_l})$[%], 3-4 s
ST40	± 0.003	± 0.002	± 0.001

Table 5.4: 95% confidence interval uncertainties

Chapter 6

Results

6.1 Turbine torque

In the laboratory, the torque on the generator and friction torque on the axial bearing were measured. The torque that the runner is able to deliver is the sum of these two since they both act on the same shaft. In Figure 6.1, the normalised rotational speed, turbine torque and power of the unit during operation is seen. As the speed of rotation decreases with 60 RPM, the torque on the turbine increases with approximately 157 Nm, stating an increase of 25%.

$$P = \omega(\tau_G + \tau_F) \tag{6.1}$$
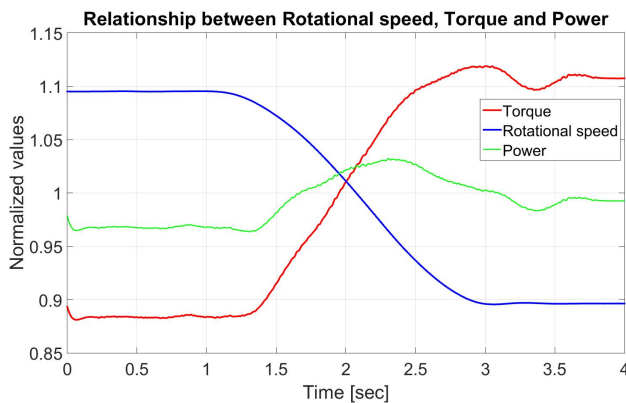
Figure 6.1: Correlation between rotational speed, turbine torque and power output

6.2 CFD

The CFD simulation results received from Chirag starts at 0.7007 seconds, and not at 0 seconds, due to unsatisfying results in-between that time range. To compare pressure and strain results from the experiment and the simulations, the sensors co-ordinates and structural model runner had to be rotated approximately 340 degrees before use to account for the missing time steps in the CFD simulation. In addition, the FSI results have only included 2/3 of the CFD pressure results due to reasons explained further on in the upcoming sections.

6.2.1 Validation of CFD

The experimental pressure plots represents the average of 10 equal measurements. As shown by the figures below, there is a difference of around 20 kPa between the results from the pressure sensors in the laboratory and the results from the CFD simulation, where the CFD simulation gives the highest pressure. The inlet pressure in the CFD simulation was set by the boundary condition of 135 kPa. This was given by the average value of pressure sensor PT40 from a single measurement conducted in the beginning of this work, which in turn was replaced by new measurements later on. But when finding this boundary pressure value it was not taken into account that one have to subtract the pressure height, $\rho gZ = 20.3$ kPa, from the pressure retrieved directly from the measurement for sensor PT40, due to the way the sensor is connected to the pipe. The new measurements gave an inlet pressure of 137.4 kPa, which is equal to 117.1 kPa when subtracting the pressure height. One can therefore say that most of the difference between the results lays in the pressure size of 137.4 - 135 kPa = 2.4 kPa plus the pressure height of 20.3 kPa. However, it is clear that the majority of the pressure results follow the same trend. Pressure is here given as static relative pressure in all the plots, expect for the dynamic representation of the experimental pressure in the draft tube cone.

Spiral casing inlet, PT02

Figure 6.2 shows that the CFD plot miss out on some distinct changes in pressure compared to the measurement plot, especially at around 2.5 seconds and after 3 seconds. This may be based on the time step size, boundary conditions, and/or solution models defined in the simulation. The pressure difference on the vertical axis at the starting point is approximately 17.7 kPa. Even so, the total variation in pressure during the decrease in rotational speed is approximately 2.5 kPa for both result plots. This imply a sufficient correlation between the measurements and the simulation.
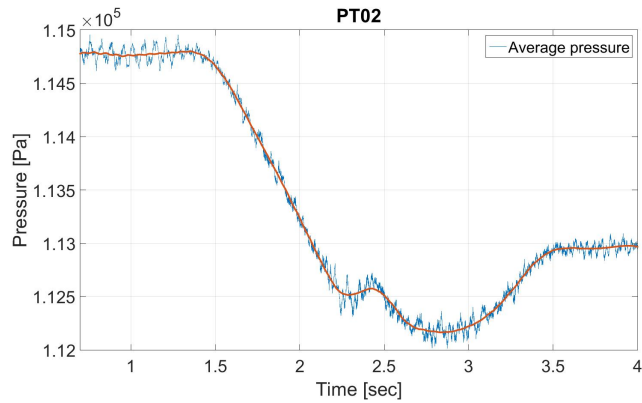
(a) LAB
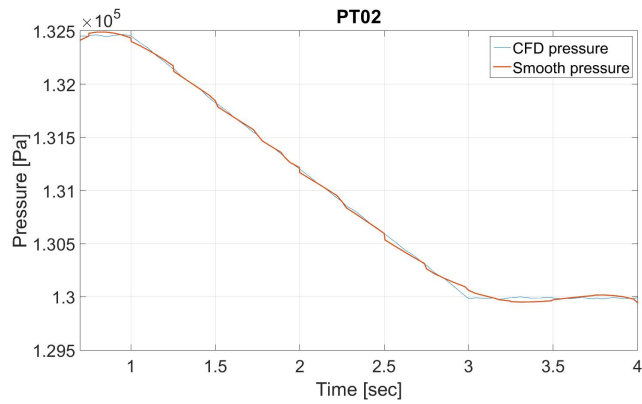
(b) CFD

Figure 6.2: Comparison of pressure results from sensor PT02

Runner, PT10-14

Figure 6.3 shows the placement of each pressure transducer mounted into the runner hub. Sensor PT11 stopped working right before the experiment was performed, but that was not crucial for the validation of the CFD model.
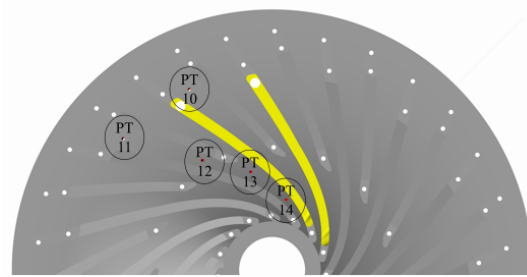
Figure 6.3: Sensors mounted in the runner hub

At the inlet of the runner between a full length blade and a splitter blade, one can find sensor PT10. While decreasing the runner speed, the pressure at the runner inlet also decreases, as seen in Figure 6.4. The change in the experimental result is equal to a drop of approximately 19.5 kPa in contrast to the pressure variation of approximately 9 kPa for the CFD result. This is a difference of considerable size. The vertical difference between the pressure plots is approximately 21 kPa.

It can be seen that the pressure is not fully stabilized before 3.5 seconds, and not after 3 seconds, which is the time when the rotational speed variation stops. The shape change in the end of the CFD plot is probably bases on the coarse plot distribution, and do not represent an actual increase in pressure.
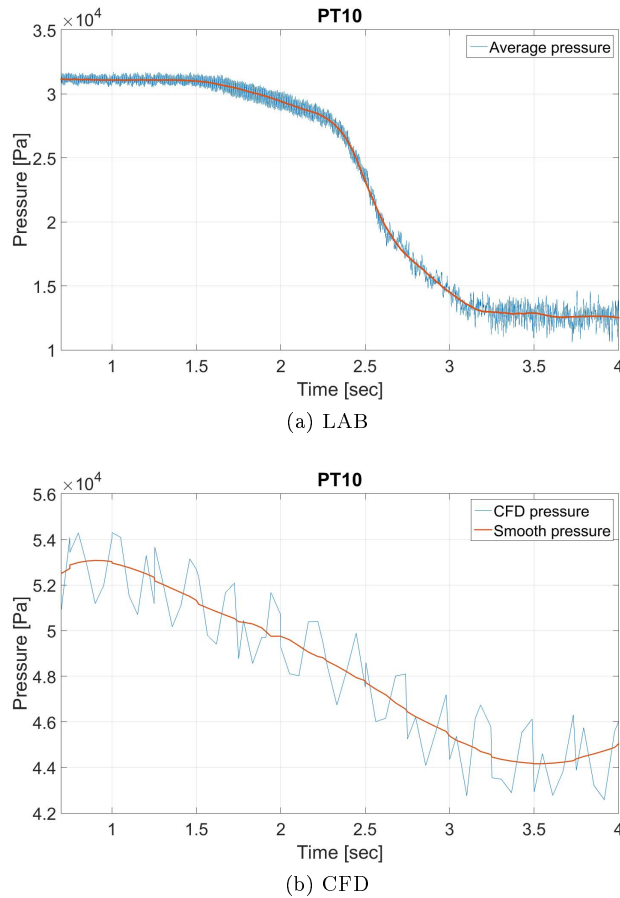
(a) LAB

(b) CFD

Figure 6.4: Comparison of pressure results from sensor PT10

Downstream the splitter blade towards the outlet of the runner, the pressure is increasing as the rotational speed is decreasing. Here, the increase for both plots is approximately 1.1 kPa. The vertical difference between the pressure plots is approximately 16.5 kPa. The changes in the curve shape at the beginning and the end of the CFD plot are also most likely based on the coarse result distribution caused by few time steps. Pressure plots from sensor PT12 and PT14 can be found in Appendix G if further study of pressure in the runner is of interest.
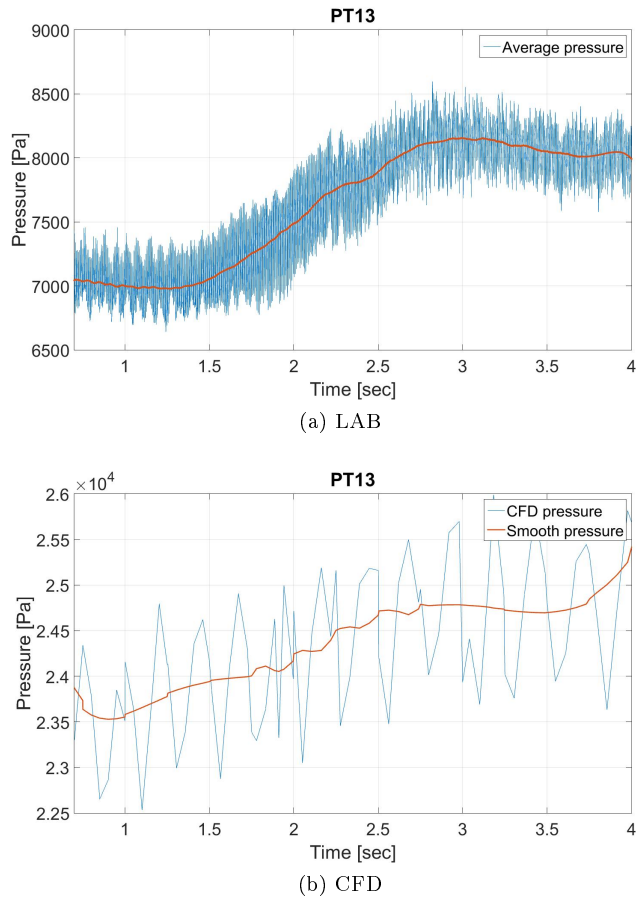
(a) LAB

(b) CFD

Figure 6.5: Comparison of pressure results from sensor PT13

Vanless space, PT20-21

In the vaneless space, there is a pressure drop of approximately 10.5 kPa when the runner speed decreases. The plots have a satisfying trend correlation. Ant the vertical difference between the pressure plots is approximately 20 kPa, which is a good fit with the PT40 input error.
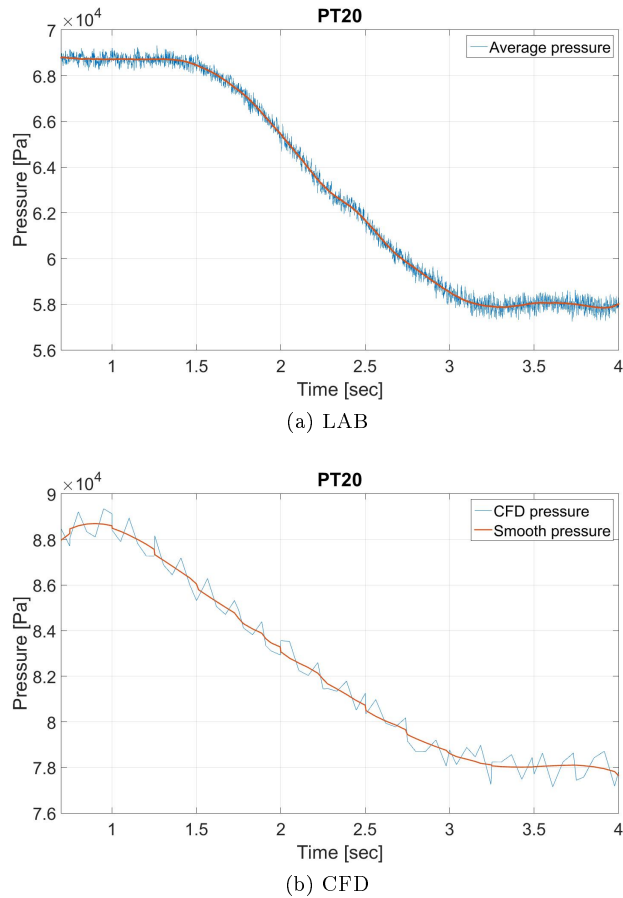
(a) LAB

(b) CFD

Figure 6.6: Comparison of pressure results from sensor PT20

Draft tube cone, PT30-33

The pressure sensors used in the draft tube cone are dynamic sensors, which means that they only react to pressure changes, and do not measure static pressure. It is therefore not correct to compare Figure 6.7a and Figure 6.7b by looking at the difference in Pa. But the plots follow the same trend, which can imply that the simulated flow in the draft tube is acceptable and captures the most important disturbances.
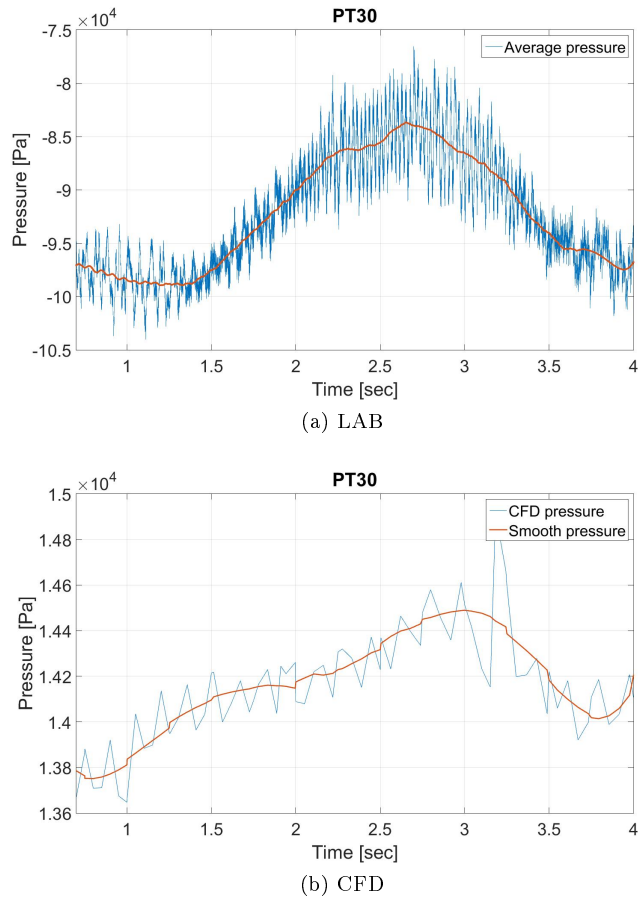
(a) LAB

(b) CFD

Figure 6.7: Comparison of pressure results from sensor PT30

Draft tube outlet, PT03

Figure 6.8 represents the pressure distribution near the outlet of the draft tube, and shows a phase shift between the two plots. This is most likely because the placement of the read-off point on the CFD model is incorrect. The pressure difference between the two plots is approximately 9.7 kPa when considering the highest peaks in the plots.
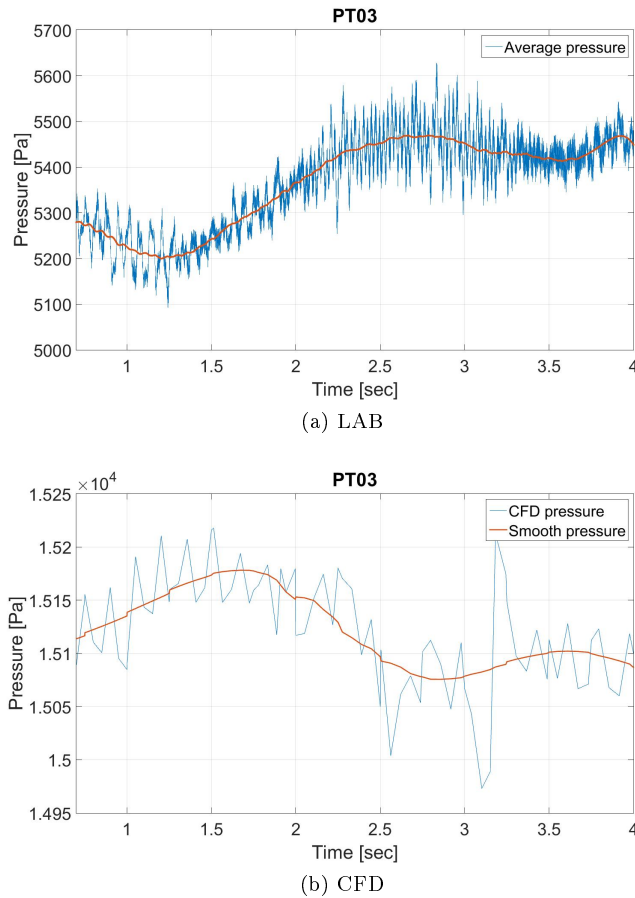
(a) LAB

(b) CFD

Figure 6.8: Comparison of pressure results from sensor PT03

6.3 FSI

6.3.1 Mesh independence test

Figure 6.9 presents the mesh independence test conducted by the author, where Figure 6.9b illustrates results at time 0.9 seconds. The test was performed over a time range of approximately 0.4 seconds; the first few seconds of the total analysis. Results are achieved from a stress probe placed at a point of high stress on the leading edge of a runner blade. By studying the plots one can see that mesh number 1 clearly stands out from the other mesh grids, and it is concluded to be an insufficient mesh with low credibility. Mesh number 3 outputs the highest stress overall, however, it peaks to a stress value that might be misleading. This is further illustrated in Figure

G.2 in Appendix G.
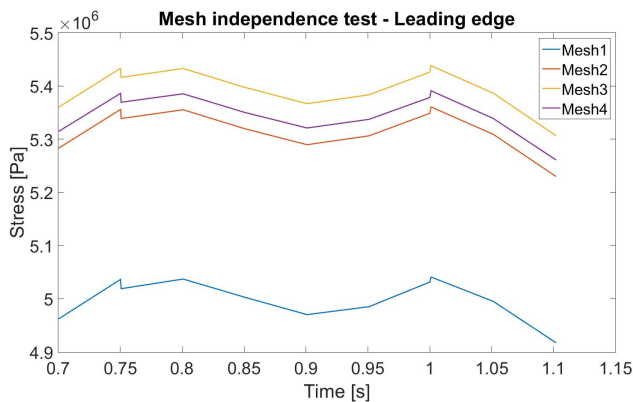
(a) Stress vs. time
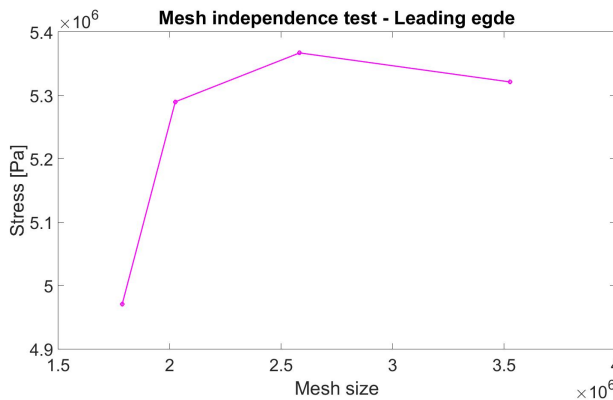
(b) Stress vs. mesh size

Figure 6.9: Mesh independence test - Leading edge

Mesh independence was unfortunately not reached, and the author had to base the selection of mesh mainly on the quality of the mesh grids. Mesh number 4 was thereby chosen for further analysis, with 3 526 317 elements and 5 225 788 nodes. Figure 6.10 shows how a part of the turbine runner is meshed. The mesh quality was checked by inspecting the Element Quality diagram, where 0 represents a bad element and 1 is a perfect element. This diagram can be found in Appendix G. The majority of the elements for mesh 4 were good, with a average element quality of 0.81645 and a standard deviation of 0.11483. The worst shaped elements were found on the labyrinths seals and on some of the leading edges of the splitter blades towards the shroud. Since the labyrinth flow was neglected from the analysis, the mesh at the labyrinth seals is not critical for the FSI results. The worst mesh element has a quality of 0.015, while the best has a quality of 1.
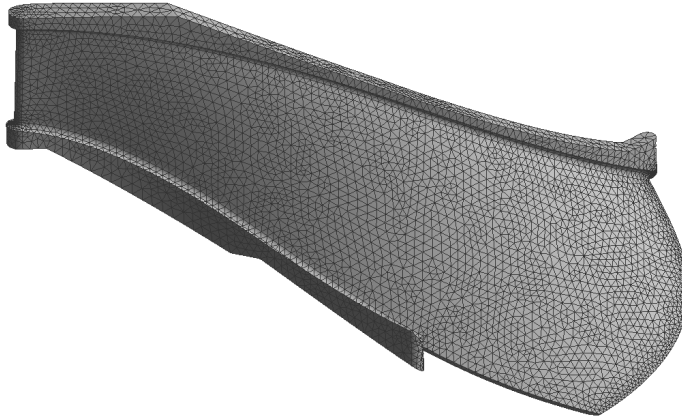
Figure 6.10: Mesh on runner blade

6.3.2 Validation of FSI

Due to concerns about the reability of the strain gage, the strain gage baseline was measured before and after the the test rig was run, while the runner was at rest and filled with water. The first measurement result showed an offset of approximately -85×10^{-6}. This continued to increase during the time the test rig was in operation, and in the end, the strain gage measurement showed a baseline of -100×10^{-6}. However, this last offset was logged after an additional 10 runs that not are included in this thesis. As a consequence, it is difficult to decide how much the strain gage output has changed between each measurement. The author chose therefore to only present the result from the first measurement, and subtract the offset of -85×10^{-6}.
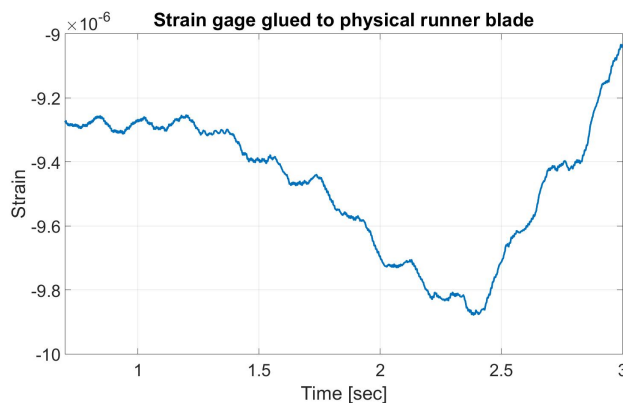

Figure 6.11: Strain gage results from laboratory measurement

The strain result shown in Figure 6.11 indicate compression of the material since the values are negative, and have a strain range of 2.8×10^{-6} over the time period 0.7 to 2.4 seconds. The author was not able to predict what are causing the increase in the curve after 2.4 seconds, but the compression is decreasing.

The best way to compare measured and simulated stresses for a Francis runner is to compare the strain components in direction of the strain gage [40]. A path that followed the direction of the actual strain gage was attached to the surface mesh, but this only solved strain along the length of the path, and not versus time. A picture of the strain path is shown in Figure 6.12. The author managed to get solutions from the first and last time step, which have average strain values of 6.4×10^{-6} and 3.68×10^{-6}, respectively. The positive values imply a decreasing tension in the runner blade, which is a contradiction to what the strain gage results are showing. Lack of time caused this validation to remain incomplete. Further work have to be conducted to get a proper validation of the stress and strain in the runner.
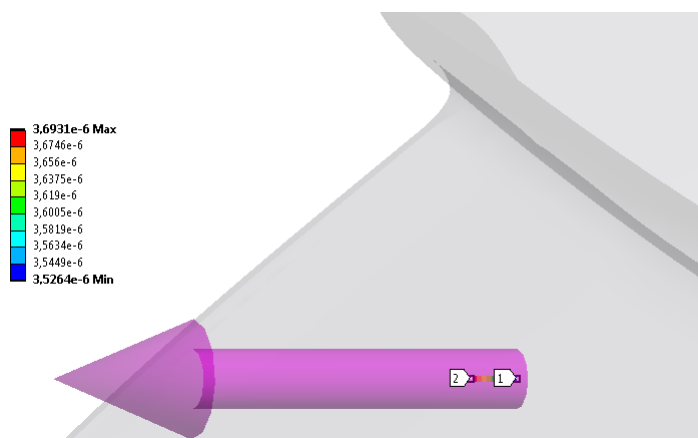

Figure 6.12: Strain path

6.3.3 FSI results

The pressure mapped onto the structural runner only represents fluid pressure from 0.7 seconds to 3 seconds. The last part from 3 to 4 seconds was difficult to implement in a continuous transient analysis with the specific FSI method applied. This was because the CFX results were handed over to the author in three separate result files, where the last time range had been set as the first solver steps of the solution since this part was finished solving first. When trying to merge the solutions, the last time range was interpreted as the first time range which is obviously wrong, so this part of the CFD solution had to be rejected. Another problem appearing when trying to merge the result files, was that only the full time steps could be used, not the partial time steps. As a consequence, the FSI simulation has been conducted

with as few as 11 time steps over a time period of 2.3 seconds.

Figure 6.13 illustrates how the pressure from the CFD simulation is mapped onto the structural runner. The pressure distribution shows the range for the last time step. As expected, the pressure decrease through the runner due to energy conversion. The maximum pressure input at the last time step has a magnitude of 71.5 kPa.
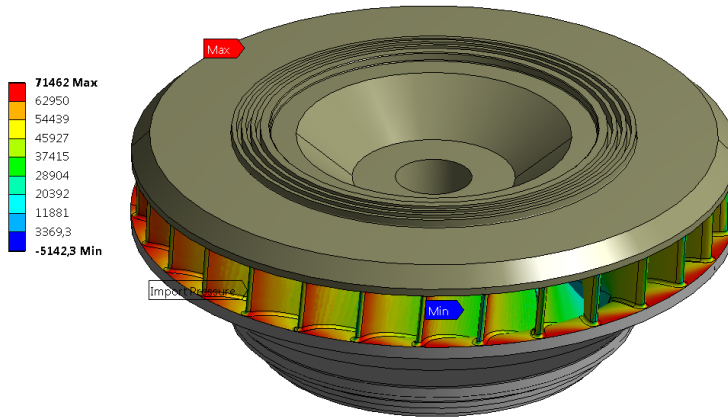

Figure 6.13: Imported pressure in ANSYS Mechanical

Equivalent stress

The stress results were analysed as von-Mises equivalent stress. Von-Mises stress is widely used by designers to check if their design can withstand a given load condition. The design will fail if the maximum value of von-Mises stress induced in the material is higher than the strength of the material. Further information on the von-Mises stress criterion is found in Appendix G.
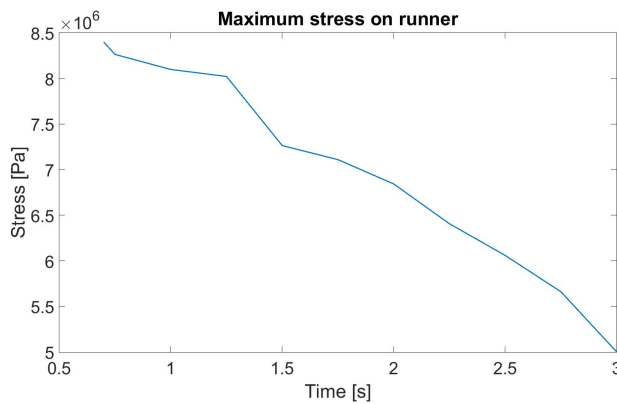

Figure 6.14: Maximum stress on runner over time [Pa]

Results from the FSI simulation shows that the material stresses in the runner decreases as the rotational speed decreases. The maximum stress found in the runner decreases from 8.4 MPa to 5 MPa, equal to a stress decrease of 40.4% during the time period of 2.3 seconds. The runner blades experience the highest stress, while the minimum stress is found in the cone.
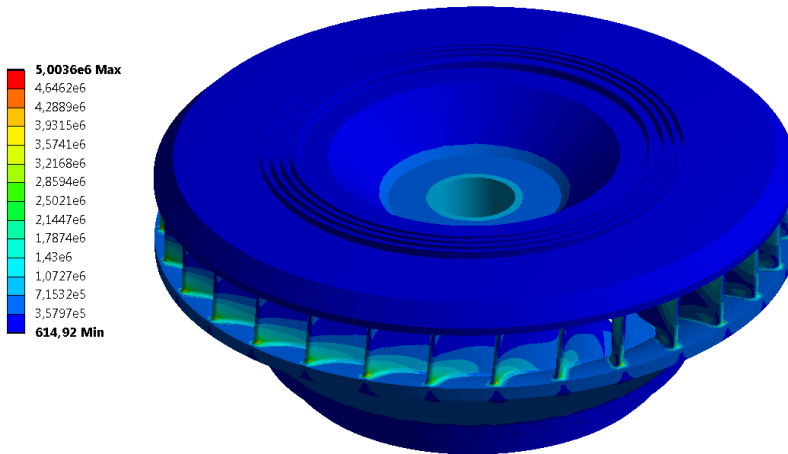
Figure 6.15: Maximum stress in runner at last time step [Pa]

Figure 6.16: Maximum stress in blades at last time step [Pa]

The materials JM 7 and JM 3 have yielding limits of 260 Mpa and 150 MPa. As explained in section 2.1, this is defined as the stress at which a material begins to deform plastically. With maximum stress of 8.4 MPa in the turbine runner, it is very unlikely for the runner to deform as a result of the pressure forces acting on the runner during variation in rotational speed.

Figure 6.17: Stress distribution on pressure side of runner blade [Pa]
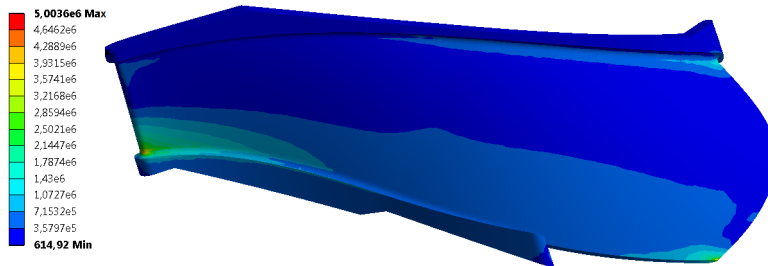
Figure 6.18: Stress distribution on suction side of runner blade [Pa]
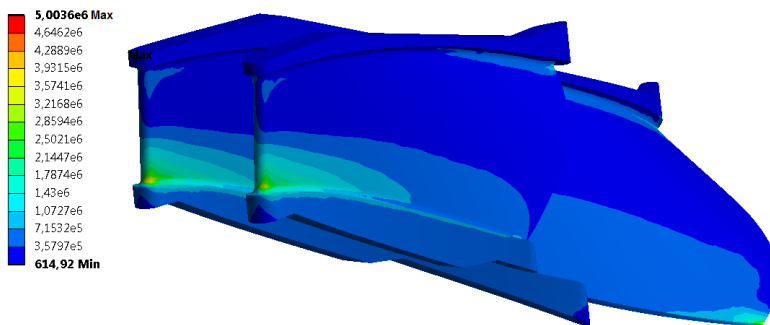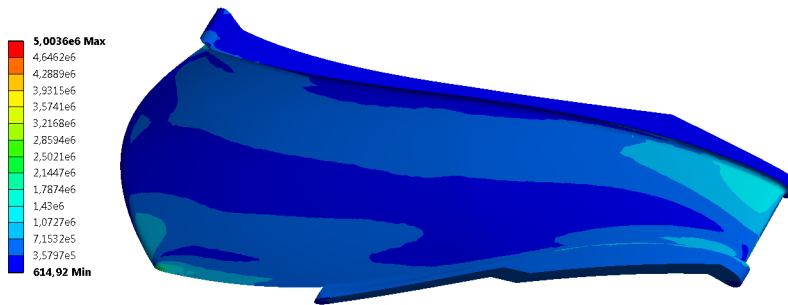
On the runner blades, the highest stresses appear at the leading and trailing edges. The maximum stress is found at the trailing edges at the distinct tip towards the shroud. This is not a surprise, as the blade is at its thinnest here. For the leading edges, the stress is especially high in the joint between blade and shroud on the pressure side of the blade. Table 6.1 presents results extracted from specific placements around on a runner blade at the start and the end time of the simulation. Edge 1 is the lower edge towards the shroud, while edge 2 is the upper edge towards the hub.

Leading egde 1	Leading edge 2	Trailing egde 1	Trailing egde 2
4.97 MPa	2.84 MPa	7.07 MPa	2.28 MPa
3.62 MPa	1.49 MPa	4.09 MPa	1.76 MPa

Table 6.1: Probe results from different surfaces/edges on a runner blade

Chapter 7

Discussion

7.1 Known error sources

7.1.1 Rotational speed functions

As mentioned, the rotational speed functions used in the laboratory and in the simulations are different. The one used for the laboratory measurements have a smooth transition in the change between steady and transient operation. It uses a sine wave to illustrate the variation in RPM. This was mainly to conduct safe operation of the test rig, thus sparing the generator for drastic changes, in addition to the fact the the grid frequency act in a way similar to a sine curve. To simplify the CFD analysis, the runner speed variation was constructed from four points, instead of using a direct input from the measurements. By looking at Figure 7.1, it is clear that the pressure results will be affected by this difference during the transient change. Before 2.25 seconds, the runner speed is highest for the sine curve, while after 2.25 seconds, the straight curve gives out the highest speed. By drawing a link between pressure and rotational speed, one can say that the pressure will change faster for the CFD simulation, which is clearly seen in Figure 6.2, Figure 6.4, and Figure 6.6.
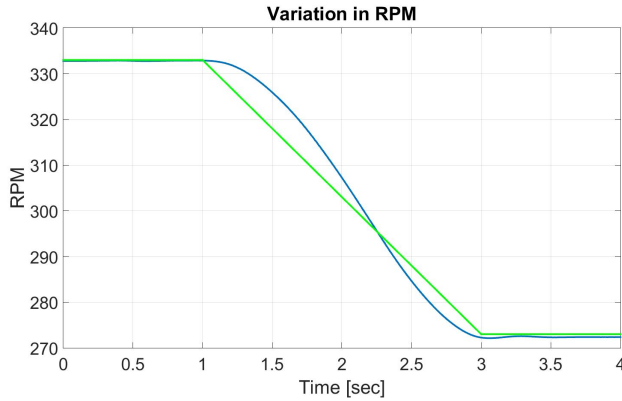
Figure 7.1: Rotational speed functions

7.1.2 Operation points

Table 7.1 shows the difference in experimental and computational operating values at the starting point. In the laboratory, the guide vane angle and the runner speed were set to 9.84° and 333 RPM, respectively. But fluctuations and uncertainties in the laboratory LabVIEW program caused the average values to get small offsets.

Parameter	CFD	Laboratory
Guide vane angle [°]	9.84	9.87
Net head [m]	13.97	12.63
Discharge [m^3/s]	0.2	0.197
Runner angular speed [rpm]	333	332.8
Hydraulic efficiency [%]	82.09	85.9
Atmospheric pressure [kPa]	101.3	100.7
Casing inlet pressure-abs [kPa]	236.33	217.8
Draft tube outlet pressure-abs [kPa]	116.57	96.0

Table 7.1: Operating points

Net head and efficiency of the Francis turbine is calculated by using Equation (2.9) and Equation (2.7). The experimental value of Δp in the equations is provided by pressure sensor PT41 and represents the difference in pressure from inlet to outlet of the model turbine. The difference in the boundary pressures between the CFD and the laboratory measurements was discussed in the the previous chapter and is the basis for the majority of the deviations in pressure and strain results. It is important also to remember that the numerical estimation of the parameters is influenced by many other factors such as turbulence modelling, combined performance of the domains, interface modelling, and performance of the mesh grid under different flow conditions.

7.1.3   Time synchronization of measurements

The measurements were logged without using a triggering time system, meaning that the author decided when each measurement series should start and stop. As a consequence, the measurement series starts at different times, and it has been difficult to decide exactly when the change in RPM starts for each measurement. When synchronizing the measurements to find the average measurement result, the 10 equal measurements do not lie exactly on top of each other, thus increasing the uncertainty of the laboratory result.

7.1.4   Sensor positions

The sensor coordinates found in Appendix B comes with uncertainties provided in mm. The surveying of the sensor locations in the laboratory have not been accurately executed. This cause differences in the results from the experimental measurements and the computational simulations. Since the first deciseconds of the CFD simulation was removed, the coordinates related to the runner had to be rotated approximately 340 degrees around the vertical axis, which may have increased the uncertainty of the coordinate placements in the computational models.

7.2   Computer simulations

7.2.1   Time step

The pressure measurements conducted in the laboratory have a sampling rate of 5 kHz which gives an accurate representation of the results, independent of revolutions of the runner. In contrast, the CFD simulation have a time step given by Equation 4.2, leading to jagged and less accurate pressure results. However, a simulation with many time steps over a long time range takes much time and requires enormous computer capacity to calculate.

7.2.2   y+ values from CFD simulation

The use of scalable wall functions in ANSYS CFX leads to production of consistent results for grids of varying y+. They activate the local usage of the log-law in regions where the y+ is sufficiently small, in connection with the standard wall function approach in coarser y+ regions. Table 7.2 presents an overview of different y+ values in the turbine runner at different times. They represents the average y+ values from each node on the specified surface. All the y+ values are well below the maximum y+ requirement of 300, thus should be able to give an accurate prediction of boundary layer flow.

Region	0.75	1	2	3	4
Hub	66.8	66.8	84.5	110.8	111.6
Full-length blades	47.5	47.5	52.0	58.5	59.1
Splitter blades	25.0	25.0	27.7	29.3	29.6
Shroud	155.1	155.2	148.7	134.0	133.7

Table 7.2: y+ values for the CFD model runner

7.2.3 Computational model geometry

Areas which do not affect the result values should have been smoothed out to simplify the meshing process and avoid increasing mesh densities for the structural model. This applies in particular to the labyrinth seals, due to the fact that the labyrinth flow was neglected in the CFD simulation and the axial thrust forces were neglected from the FEM simulation. Furthermore, the author could have given more thought to the idea of looking at only 1/15 of the turbine runner to reduce the complexity of the analysis.

7.2.4 Mesh independence test

A mesh grid independent of the results was not achieved in this work. As a consequence, the magnitudes of result values are uncertain. However, the author created mesh grids based on knowledge from previous similar studies, with finer mesh cells in areas where it was expected to see high stress and strain. Lack of computer capacity and time to perform a simulation with a large number of mesh elements, made it more difficult to gain a perfect mesh.

7.3 FSI

There are several ways to perform a FSI analysis in ANSYS. If the CFX and Mechanical analyses are performed in the same ANSYS Workbench, the modules could be directly connected and results would be able to be transferred back and fourth. This was not the case for this project. The author received three CFX result files which together supplied the total solution. Then, there were two possible ways to conduct the FSI analysis; either save separate pressure files for each component and each time step and import into Mechanical as external data, or use the ACT Transient FSI extension and save three files to import into Mechanical. For transient analysis, the ACT Transient method is much easier and less time consuming than using external data. But for this case, the solver steps of the CFX result files were saved in the wrong order, in addition to separated in three files, which made it more difficult to create the needed load files.

7.3.1 Pressure mapping

Since the mesh grids (fluid and solid) on the runner were created in separate workspaces, it is not ensured that the mesh elements corresponds at the fluid-solid interface for accurate transmission of the pressure loads. The CFD runner consist of 2 579 790 mesh elements while the FEM model consist of 3 526 317 mesh elements. Unfortunately, the author was unable to retrieve mapping statistics due to problems with the simulation.

7.3.2 Deformation of runner

Compared to a prototype turbine runner, the small model runner dimensions gives out very low stresses. The model runner in the Waterpower laboratory also have stiff materials to ensure a long lifetime, which increases the resistance towards deformation. However, it is worth noting that the curved trailing edge of the runner blades in the model runner makes it more sensitive to dynamic pressure loading compared to a runner with straight cut trailing edges.

Chapter 8

Conclusion

In this thesis, a transient FSI analysis of a Francis runner has been carried out. The runner was subjected to a decrease in rotational speed of 60 RPM over a time period of 2 seconds while the guide vane opening was held constant. The aim was to investigate how variations in grid frequency impact stresses in the turbine. Results were validated against measured values from an experiment conducted on the same turbine model in the Waterpower Laboratory. The simulation results showed that the overall equivalent stress in the runner decrease as the speed decreases. The highest stress was found at the blade trailing edge towards the shroud, where the blade is at its thinnest. At the beginning of the simulation, the magnitude of this stress value was 8.4 MPa. It decreased down to 5 Mpa, stating a stress change of 40.4%.

Validation of the CFD simulation showed a satisfying correlation between measured and simulated pressure through the turbine. This conclusion is drawn when looking beyond the fact that the input boundary conditions to the CFD simulation had an error of known size. However, the author did not manage to validate stress and strain in the structural model due to difficulties with the FSI simulation and uncertainties related to the physical strain gage. Therefore, further work is needed to fully investigate the complete result history.

Chapter 9

Further work

- Proper validation of the stress results in the runner is needed. Using a strain gage is good way to conduct this validation even though the author did not manage to do so within the time limit given by this thesis.

- In order to obtain a more detailed picture of the dynamic behaviour of the turbine, realistic oscillations of the runner should be examined, allowing to gain insight into more complex fluid-structure interaction phenomena that might occur.

- Additional operating points outside BEP could be of interest, where several flow characteristic are more active.

- Conducting a frequency analysis on the laboratory results allow detection of pulsations from RSI and other disturbances in the flow. This makes it easier to conclude on what the results are based upon.

- A mesh grid that is independent of the results should be achieved. This will give a more accurate computational solution.

- Conducting a two-way FSI simulation would provide more trustworthy results. The optimal way to perform such an analysis is to conduct both FEM and CFD in the same workspace to make sure the geometries and mesh grids are corresponding.

- Leakage flow through the labyrinth seals and additional axial forces on hub, shroud and labyrinth seals should be included in the FSI analysis.

Bibliography

[1] Filtering and smoothing data. `http://www.me.berkeley.edu/~lwlin/me128/FEMNotes.pdf`. Accessed: 17.02.2016.

[2] Francis-99, second workshop (2016), test case. `https://www.ntnu.edu/nvks/test-case`. Accessed: 18.04.2016.

[3] Francis hydro turbine. `https://renewables.gepower.com/hydro-power/large-hydropower-solutions/hydro-turbines/francis-turbine.html`. Accessed: 03.02.2016.

[4] Ansys cfx. `http://www.ansys.com/Products/Fluids/ANSYS+CFX`, . Accessed: 25.01.2016.

[5] Ansys mechanical. `http://www.ansys.com/Products/Structures/ANSYS+Mechanical`, . Accessed: 25.01.2016.

[6] Purpose of a calibration? `https://msl.irl.cri.nz/services/temperature-and-humidity/humidity-calibration-service/calibration-certificate/purpose-of-a-`. Accessed: 22.05.2016.

[7] Defining fluid-strucutre interactions. `https://www.comsol.com/multiphysics/fluid-structure-interaction`. Accessed: 05.05.2016.

[8] Introduction to finite element modeling. `http://se.mathworks.com/help/curvefit/smoothing-data.html`. Accessed: 25.04.2016.

[9] Kraftmarkedet. `http://www.fornybar.no/kraftmarkedet`. Accessed: 27-01-2016.

[10] Hydroelectric power. `http://www.mpoweruk.com/hydro_power.htm`. Accessed: 01.06.2016.

[11] Francis-99. `https://www.ntnu.edu/web/norwegian-hydropower-center/francis-99`. Accessed: 15.02.2016.

[12] Eo stÅl as - tekniska data. `http://www.eostal.se/Templates/SearchResult1.aspx?CMS_SearchString=teknisk+data+bronser`. Accessed: 11.05.2016.

[13] Pressure measurement overview. `http://www.ni.com/white-paper/13034/en/`. Accessed: 04.05.2016.

[14] Measuring strain with strain gages. `http://www.ni.com/white-paper/3642/en/`. Accessed: 04.05.2016.

[15] What is von mises stress? `http://www.learnengineering.org/2012/12/what-is-von-mises-stress.html`. Accessed: 05.06.2016.

[16] Stine Andersen, Martha Marie Øberg, Siri Veila, and Helene Sundheim. *Energiskolen, Lærehefte*. Statnett, 8 2014.

[17] André Bakker. Lecture 5 - solution methods. applied computational fluid dynamics, 2002. http://www.bakker.org, Fluent Inc.

[18] Jonas Bergmann-Paulsen. Fsi-analysis of a francis turbine. 2012.

[19] Hermod Brekke. Pumper og turbiner. *NTNU, Vannkraftlaboratoriet*, 2003.

[20] Hermod Brekke. Konstruksjon av pumper og turbiner. *Waterpower laboratory, NTNU*, 2008.

[21] Hermod Brekke. Design, performance and maintenance of francis turbines. *Global Journal of Research In Engineering*, 13(5), 2013.

[22] Bjarne Børresen. Sprekker i løpehjul. analyser, forebygging og erfaringer.

[23] William D Callister, David G Rethwisch, et al. *Materials science and engineering: an introduction*, volume 7. Wiley New York, 2007.

[24] A Deepak, CJ Roger, and J Gerald. The impact of hydroelectric power and other forms of generation on grid frequency stability for the wecc region. *HydroVision International, Sacramento, CA, July*, pages 19–22, 2011.

[25] Rakel Ellingsen and Pål-Tore Storli. Simulations of the dynamic load in a francis runner based on measurements of grid frequency variations. *International Journal of Fluid Machinery and Systems*, 8(2):102–112, 2015.

[26] Christopher Frey. One-way fluid-structure-interaction enhanced by act, 2014.

[27] D Frunzaverde, S Muntean, G Marginean, V Campian, L Marşavina, R Terzi, and V Şerban. Failure analysis of a francis turbine runner. In *IOP Conference Series: Earth and Environmental Science*, volume 12, page 012115. IOP Publishing, 2010.

[28] Ove S Grande, G Doorman, and BH Bakken. Exchange of balancing resources between the nordic synchronous system and the netherlands/germany/poland. *SINTEF Energy Research, Project*, (12X535):02, 2008.

[29] Sigurd Tangerud Haga. Dynamic load on high head francis turbines during start/stop. 2014.

[30] Russell C Hibbeler. *Statics and mechanics of materials*. Pearson Higher Ed, 2013.

[31] Frida Holand. Fremtidens frekvensstabilitet i kraftsystemet: roterende reserver, primærreserver og ny uregulerbar kraft i synkronområdet norden i 2020. 2014.

[32] Julie Marie Hovland. Pressure pulsations and stress in a high head francis model turbine. 2013.

[33] Arne Kjølle. Mechanical equipment. *Waterpower laboratory, NTNU*, 2001.

[34] Einar Kobro. Measurement of pressure pulsations in francis turbines. 2010.

[35] Alberto Luna-Ramírez, Alfonso Campos-Amezcua, Oscar Dorantes-Gómez, Zdzislaw Mazur-Czerwiec, and Rodolfo Muñoz-Quezada. Failure analysis of runner blades in a francis hydraulic turbine—case study. *Engineering Failure Analysis*, 59:314–325, 2016.

[36] Camilla Odelbrink. Design of an alternative frequency controller for hydropower stations: Reducing the 60-second floating in the grid frequency of the nordic power system. 2014.

[37] Jørgen Ramdal and Ole Gunnar Dahlhaug. *Procedures for the Francis Turbine Test Rig*. Waterpower Laboratory, NTNU, 2006.

[38] Trent Ratzlaff. *Effects Future Renewable Installations Will Have on System Synchronous and Synthetic Inertia*. PhD thesis, TU Delft, Delft University of Technology, 2012.

[39] Kristoffer Rundhaug. Development of new mechanical design of model turbines. 2014.

[40] U Seidel, B Hübner, J Löfflad, and P Faigle. Evaluation of rsi-induced stresses in francis runners. In *IOP Conference Series: Earth and Environmental Science*, volume 15, page 052010. IOP Publishing, 2012.

[41] U Seidel, C Mende, B Hübner, W Weber, and A Otto. Dynamic loads in francis runners and their impact on fatigue life. In *IOP Conference Series: Earth and Environmental Science*, volume 22, page 032054. IOP Publishing, 2014.

[42] IEC Standard. 60193. *IEC: International Electrotechnical Commission. Hydraulic turbines, storage pumps, and pump-turbines. Model acceptance tests. Publication data*, pages 11–01, 1999.

[43] *Systemdrifts- og Markedsutviklingsplan 2014-2020. Tiltaksplan for sikker og effektiv drift av kraftverksystemet*. Statnett, 2014.

[44] Pål-Tore Storli. Modelltest av francis turbin i vannkraftlaboratoriet ved ntnu. 2006.

[45] PT Storli and TK Nielsen. Dynamic load on a francis turbine runner from simulations based on measurements. In *IOP Conference Series: Earth and Environmental Science*, volume 22, page 032056. IOP Publishing, 2014.

[46] Andrea Stranna. Testing of rpt in pumping mode of operation. 2013.

[47] Pieter Tielens and Dirk Van Hertem. Grid inertia and frequency control in power systems with high penetration of renewables. *status: published*, 2012.

[48] Chirag Trivedi, Bhupendra Gandhi, and Cervantes J Michel. Effect of transients on francis turbine runner life: a review. *Journal of Hydraulic Research*, 51(2): 121–132, 2013.

[49] Chirag Trivedi, Michel J Cervantes, and Ole G Dahlhaug. Experimental and numerical studies of a high-head francis turbine: A review of the francis-99 test case. *Energies*, 9(2):74, 2016.

[50] Henk Kaarle Versteeg and Weeratunge Malalasekera. *An introduction to computational fluid dynamics: the finite volume method*. Pearson Education, 2007.

[51] Pierre JC Vogler-Finck and Wolf-Gerrit Früh. Evolution of primary frequency control requirements in great britain with increasing wind generation. *International Journal of Electrical Power & Energy Systems*, 73:377–388, 2015.

[52] Hermann-Josef Wagner and Jyotirmay Mathur. *Introduction to hydro energy systems: basics, technology and operation*. Springer Science & Business Media, 2011.

[53] Ivar Wangensteen. Power system economics: the nordic electricity market. 2012.

Appendix A

Risk assessment

NTNU

SINTEF

Risikovurderingsrapport

FRANCIS riggen

Prosjekttittel	Stasjonære og transiente trykkmålinger på Francis riggen
Apparatur	FRANCIS riggen
Enhet	NTNU
Apparaturansvarlig	Bård Brandåstrø
Prosjektleder	Pål-Tore Storli/Ole Gunnar Dahlhaug
HMS-koordinator	Morten Grønli
HMS-ansvarlig (linjeleder)	Olav Bolland
Plassering	Vannkraftlaboratoriet
Romnummer	11
Risikovurdering utført av	Ingebjørg Valkvæ, Rakel Ellingsen, Einar Agnalt og Katarina Kloster

Godkjenning:

	Navn	Dato	Signatur
Prosjektleder	Pål-Tore Storli/ Ole Gunnar Dahlhaug	5/4 -16	
HMS koordinator	Morten Grønli		
HMS ansvarlig (linjeleder)	Olav Bolland		

INNHOLDSFORTEGNELSE

1   INNLEDNING

Stasjonære og transiente trykkmålinger skal gjennomføres flere steder i Francis riggen. Forsøket skal forgå i April 2016.

2   KONKLUSJON

Riggen er bygget til god laboratorium praksis (GLP).

Apparaturkortet får en gyldighet på **4 måneder**
Forsøk pågår kort får en gyldighet på **4 måneder**

3   ORGANISERING

Rolle	NTNU
Prosjektleder	Pål-Tore Storli/ Ole Gunnar Dahlhaug
Apparaturansvarlig	Bård Brandåstrø
Romansvarlig	Halvor Haukvik
HMS koordinator	Morten Grønli
HMS ansvarlig (linjeleder):	Olav Bolland

4   RISIKOSTYRING AV PROSJEKTET

Hovedaktiviteter risikostyring	Nødvendige tiltak, dokumentasjon	DTG
Prosjekt initiering	Prosjekt initiering mal	x
Veiledningsmøte	Skjema for Veiledningsmøte med pre-risikovurdering	x
Innledende risikovurdering	Fareidentifikasjon – HAZID Skjema grovanalyse	x
Vurdering av teknisk sikkerhet	Prosess-HAZOP Tekniske dokumentasjoner	x
Vurdering av operasjonell sikkerhet	Prosedyre-HAZOP Opplæringsplan for operatører	x
Sluttvurdering, kvalitetssikring	Uavhengig kontroll Utstedelse av apparaturkort Utstedelse av forsøk pågår kort	

5   TEGNINGER, FOTO, BESKRIVELSER AV FORSØKSOPPSETT

Vedlegg:
Prosess og Instrumenterings Diagram, (PID) skal inneholde:
- *Alle komponenter i forsøksoppsetningen*
- *Komponentliste med spesifikasjoner*
- *Tegninger og bilder som beskriver forsøksoppsetningen.*

Hvor oppholder operatør seg, hvor er gassflasker, avstegningsventiler for vann/luft.
Annen dokumentasjon som beskriver oppsett og virkemåte.

6 EVAKUERING FRA FORSØKSOPPSETNINGEN

Evakuering skjer på signal fra alarmklokker eller lokale gassalarmstasjon med egen lokal varsling med lyd og lys utenfor aktuelle rom, se 6.2
Evakuering fra rigg området foregår igjennom merkede nødutganger til møteplass, (hjørnet gamle kjemi/kjelhuset eller parkeringsplass 1a-b.)
Aksjon på rigg ved evakuering: Slå av luft og vanntilførsel

7 VARSLING

7.1 Før forsøkskjøring

Varsling per e-post, til **Liste iept-experiments@ivt.ntnu.no**
I e-posten skal det stå::
- Navn på forsøksleder:
- Navn på forsøksrigg:
- Tid for start: (dato og klokkelslett)
- Tid for stop: (dato og klokkelslett)

All forsøkskjøringen skal planlegges og legges inn i aktivitetskalender for lab. Forsøksleder må få bekreftelse på at forsøkene er klarert med øvrig labdrift før forsøk kan iverksettes.

7.2 Ved uønskede hendelser

BRANN
Ved brann en ikke selv er i stand til å slukke med rimelige lokalt tilgjengelige slukkemidler, skal nærmeste brannalarm utløses og arealet evakueres raskest mulig. En skal så være tilgjengelig for brannvesen/bygningsvaktmester for å påvise brannsted.
Om mulig varsles så:

NTNU	SINTEF
Morten Grønli, Mob: 918 97 515	
Olav Bolland: Mob: 918 97 209	
NTNU – SINTEF Beredskapstelefon	800 80 388

GASSALARM
Ved gassalarm skal gassflasker stenges umiddelbart og området ventileres. Klarer man ikke innen rimelig tid å få ned nivået på gasskonsentrasjonen så utløses brannalarm og laben evakueres. Dedikert personell og eller brannvesen sjekker så lekkasjested for å fastslå om det er mulig å tette lekkasje og lufte ut området på en forsvarlig måte.
Varslingsrekkefølge som i overstående punkt.

PERSONSKADE
- Førstehjelpsutstyr i Brann/førstehjelpsstasjoner,
- Rop på hjelp,
- Start livreddende førstehjelp
- **Ring 113** hvis det er eller det er tvil om det er alvorlig skade.

ANDRE UØNSKEDE HENDELSER (AVVIK)
NTNU:
Rapportering av uønskede hendelser, Innsida, avviksmeldinger
https://innsida.ntnu.no/wiki/-/wiki/Norsk/Melde+avvik

SINTEF:
Synergi

8　VURDERING AV TEKNISK SIKKERHET

8.1　Fareidentifikasjon, HAZOP

Se kapittel 13 "Veiledning til rapport mal.
Forsøksoppsetningen deles inn i følgende noder:

Node 1	Rørsystem med pumpe
Node 2	Roterende utstyr (turbin og gir)
Node 3	Hydraulikk

Vedlegg, skjema: Hazop_mal

Vurdering
Node1:
- Overtrykksventil som slår ut dersom trykket i systemet blir for høyt.
- Rørelementer er eksternt levert og godkjent for aktuelt trykk.

Node2:
- Roterende utstyr står utilgjengelig for folk. Dvs det er innkapslet eller man må klatre for å nå opp til det.

Node3:
- Trykk i slanger og rør (olje/vann) Hydraulikkslanger er ikke egenprodusert
- Trykksatt utstyr er sertifisert og kjøpt inn av eksterne leverandører

8.2　Brannfarlig, reaksjonsfarlig og trykksatt stoff og gass

Se kapittel 13 "Veiledning til rapport mal.
Inneholder forsøkene brannfarlig, reaksjonsfarlig og trykksatt stoff

| JA | Trykksatt hydraulikkolje, trykksatt vann |

Vurdering: Arbeidsmedium er vann. Alle rør er levert av eksternt firma med prøvesertifikat
Hydraulikk til hydrostatisk lager. Hyllevare komponenter, de er dermed ikke egenprodusert

8.3　Trykkpåkjent utstyr

Inneholder forsøksoppsetningen trykkpåkjent utstyr:

| JA | Utstyret trykk-testes i henhold til norm og dokumenteres |

Vurdering: Prøvesertifikat for trykktesting finnes i labperm.

8.4 Påvirkning av ytre miljø (utslipp til luft/vann, støy, temperatur, rystelser, lukt)

Se kapittel 13 "Veiledning til rapport mal..

NEI	

8.5 Stråling

Se kapittel 13 "Veiledning til rapport mal.

NEI	

Vedlegg:
Vurdering:

8.6 Bruk og behandling av kjemikalier

Se kapittel 13 "Veiledning til rapport mal.

JA	Hydraulikkolje

Vedlegg: Sikkerhetsdatablad
Vurdering: Hydraulikkolje, mineralsk olje. Datablad er vedlagt.

8.7 El sikkerhet (behov for å avvike fra gjeldende forskrifter og normer)

NEI	

9 VURDERING AV OPERASJONELL SIKKERHET

Sikrer at etablerte prosedyrer dekker alle identifiserte risikoforhold som må håndteres gjennom operasjonelle barrierer og at operatører og teknisk utførende har tilstrekkelig kompetanse.

9.1 Prosedyre HAZOP

Se kapittel 13 "Veiledning til rapport mal.
Metoden er en undersøkelse av operasjonsprosedyrer, og identifiserer årsaker og farekilder for operasjonelle problemer.
Vedlegg: HAZOP_MAL_Prosedyre
Vurdering:

9.2 Drifts og nødstopps prosedyre

Se kapittel 13 "Veiledning til rapport mal.
Driftsprosedyren er en sjekkliste som skal fylles ut for hvert forsøk.
Nødstopp prosedyren skal sette forsøksoppsetningen i en harmløs tilstand ved uforutsette hendelser.
Vedlegg: Procedure for running experiments
Nødstopp prosedyre:

9.3 Opplæring av operatører

Dokument som viser Opplæringsplan for operatører utarbeides for alle forøksoppsetninger.
- *Kjøring av pumpesystem*

Vedlegg: Opplæringsplan for operatører

9.4 Tekniske modifikasjoner

9.5 Personlig verneutstyr

- *Det er påbudt med vernebriller i sonen anlegget er plassert i.*

9.6 Generelt

9.7 Sikkerhetsutrustning

9.8 Spesielle tiltak

10 TALLFESTING AV RESTRISIKO – RISIKOMATRISE

Se kapittel 13 "Veiledning til rapport mal.
Risikomatrisen vil gi en visualisering og en samlet oversikt over aktivitetens risikoforhold slik at ledelse og brukere får et mest mulig komplett bilde av risikoforhold.

IDnr	Aktivitet-hendelse	Frekv-Sans	Kons	RV
1	Lekkasje i Hydraulikk	1	A	A1
2	Fremmedlegemer i vannet	1	A	A1
3	Rørbrudd	1	A	A1
4	Roterende Aksling	1	B	B1

Vurdering restrisiko: *Det er liten restrisiko ved forsøkene, foruten at trykk-satt vann og olje fordrer bruk av vernebriller. Fremmedlegemer i vannet gir liten risiko for personskade, men kan føre til store skader på maskineri.*

11   LOVER FORSKRIFTER OG PÅLEGG SOM GJELDER

Se http://www.arbeidstilsynet.no/regelverk/index.html
- Lov om tilsyn med elektriske anlegg og elektrisk utstyr (1929)
- Arbeidsmiljøloven
- Forskrift om systematisk helse-, miljø- og sikkerhetsarbeid (HMS Internkontrollforskrift)
- Forskrift om sikkerhet ved arbeid og drift av elektriske anlegg (FSE 2006)
- Forskrift om elektriske forsyningsanlegg (FEF 2006)
- Forskrift om utstyr og sikkerhetssystem til bruk i eksplosjonsfarlig område NEK 420
- Forskrift om håndtering av brannfarlig, reaksjonsfarlig og trykksatt stoff samt utstyr og anlegg som benyttes ved håndteringen
- Forskrift om Håndtering av eksplosjonsfarlig stoff
- Forskrift om bruk av arbeidsutstyr.
- Forskrift om Arbeidsplasser og arbeidslokaler
- Forskrift om Bruk av personlig verneutstyr på arbeidsplassen
- Forskrift om Helse og sikkerhet i eksplosjonsfarlige atmosfærer
- Forskrift om Høytrykksspyling
- Forskrift om Maskiner
- Forskrift om Sikkerhetsskilting og signalgivning på arbeidsplassen
- Forskrift om Stillaser, stiger og arbeid på tak m.m.
- Forskrift om Sveising, termisk skjæring, termisk sprøyting, kullbuemeisling, lodding og sliping (varmt arbeid)
- Forskrift om Tekniske innretninger
- Forskrift om Tungt og ensformig arbeid
- Forskrift om Vern mot eksponering for kjemikalier på arbeidsplassen (Kjemikalieforskriften)
- Forskrift om Vern mot kunstig optisk stråling på arbeidsplassen
- Forskrift om Vern mot mekaniske vibrasjoner
- Forskrift om Vern mot støy på arbeidsplassen

Veiledninger fra arbeidstilsynet
se: http://www.arbeidstilsynet.no/regelverk/veiledninger.html

12   DOKUMENTASJON

- Tegninger, foto, beskrivelser av forsøksoppsetningen
- Hazop_mal
- Sertifikat for trykkpåkjent utstyr
- Håndtering avfall i NTNU
- Sikker bruk av LASERE, retningslinje
- HAZOP_MAL_Prosedyre
- Forsøksprosedyre
- Opplæringsplan for operatører
- Skjema for sikker jobb analyse, (SJA)
- Apparaturkortet
- Forsøk pågår kort

13   VEILEDNING TIL RAPPORTMAL

Kapittel 7 Vurdering av teknisk sikkerhet

Sikre at design av apparatur er optimalisert i forhold til teknisk sikkerhet.

Identifisere risikoforhold knyttet til valgt design, og eventuelt å initiere re-design for å sikre at størst mulig andel av risiko elimineres gjennom teknisk sikkerhet.

Punktene skal beskrive hva forsøksoppsetningen faktisk er i stand til å tåle og aksept for utslipp.

7.1 Fareidentifikasjon, HAZOP

Forsøksoppsetningen deles inn i noder: (eks M*otorenhet, pumpeenhet, kjøleenhet.)*

Ved hjelp av ledeord identifiseres årsak, konsekvens og sikkerhetstiltak. Konkluderes det med at tiltak er nødvendig anbefales disse på bakgrunn av dette. Tiltakene lukkes når de er utført og Hazop sluttføres.

(eks "No flow", årsak: rør er deformert, konsekvens: pumpe går varm, sikkerhetsforanstaltning: måling av flow med kobling opp mot nødstopp eller hvis konsekvensen ikke er kritisk benyttes manuell overvåkning og punktet legges inn i den operasjonelle prosedyren.)

7.2 Brannfarlig, reaksjonsfarlig og trykksatt stoff.

I henhold til Forskrift om håndtering av brannfarlig, reaksjonsfarlig og trykksatt stoff samt utstyr og anlegg som benyttes ved håndteringen

Brannfarlig stoff: Fast, flytende eller gassformig stoff, stoffblanding, samt stoff som forekommer i kombinasjoner av slike tilstander, som i kraft av sitt flammepunkt, kontakt med andre stoffer, trykk, temperatur eller andre kjemiske egenskaper representerer en fare for brann.

Reaksjonsfarlig stoff: Fast, flytende, eller gassformig stoff, stoffblanding, samt stoff som forekommer i kombinasjoner av slike tilstander, som ved kontakt med vann, ved sitt trykk, temperatur eller andre kjemiske forhold, representerer en fare for farlig reaksjon, eksplosjon eller utslipp av farlig gass, damp, støv eller tåke.

Trykksatt stoff: Annet fast, flytende eller gassformig stoff eller stoffblanding enn brann- eller reaksjonsfarlig stoff, som er under trykk, og som derved kan representere en fare ved ukontrollert utslipp.

Nærmere kriterier for klassifisering av brannfarlig, reaksjonsfarlig og trykksatt stoff er fastsatt i vedlegg 1 i veiledningen til forskriften "Brannfarlig, reaksjonsfarlig og trykksatt stoff"

http://www.dsb.no/Global/Publikasjoner/2009/Veiledning/Generell%20veiledning.pdf

http://www.dsb.no/Global/Publikasjoner/2010/Tema/Temaveiledning_bruk_av_farlig_stoff_Del_1.pdf

Rigg og areal skal gjennomgås med hensyn på vurdering av Ex sone

- Sone 0: Alltid eksplosiv atmosfære, for eksempel inne i tanker med gass, brennbar væske.
- Sone 1: Primær sone, tidvis eksplosiv atmosfære for eksempel et fylle tappe punkt

- Sone 2: Sekundert utslippssted, kan få eksplosiv atmosfære ved uhell, for eksempel ved flenser, ventiler og koblingspunkt

7.4 Påvirkning av ytre miljø

Med forurensning forstås: tilførsel av fast stoff, væske eller gass til luft, vann eller i grunnen støy og rystelser påvirkning av temperaturen som er eller kan være til skade eller ulempe for miljøet.

Regelverk: http://www.lovdata.no/all/hl-19810313-006.html#6

NTNU retningslinjer for avfall se: http://www.ntnu.no/hms/retningslinjer/HMSR18B.pdf

7.5 Stråling

Stråling defineres som

Ioniserende stråling: Elektromagnetisk stråling (i strålevernsammenheng med bølgelengde <100 nm) eller hurtige atomære partikler (f.eks alfa- og beta-partikler) som har evne til å ionisere atomer eller molekyler
Ikke-ioniserende stråling: Elektromagnetisk stråling (bølgelengde >100 nm), og ultralyd[1], som har liten eller ingen evne til å ionisere.
Strålekilder: Alle ioniserende og sterke ikke-ioniserende strålekilder.
Ioniserende strålekilder: Kilder som avgir ioniserende stråling, f.eks alle typer radioaktive kilder, røntgenapparater, elektronmikroskop
Sterke ikke-ioniserende strålekilder: Kilder som avgir sterk ikke-ioniserende stråling som kan skade helse og/eller ytre miljø, f.eks laser klasse 3B og 4, MR[2]-systemer, UVC[3]-kilder, kraftige IR-kilder[4]
[1] Ultralyd er akustisk stråling ("lyd") over det hørbare frekvensområdet (>20 kHz). I strålevernforskriften er ultralyd omtalt sammen med elektromagnetisk ikke-ioniserende stråling.
[2] MR (eg. NMR) - kjernemagnetisk resonans, metode som nyttes til å «avbilde» indre strukturer i ulike materialer.
[3] UVC er elektromagnetisk stråling i bølgelengdeområdet 100-280 nm.
[4] IR er elektromagnetisk stråling i bølgelengdeområdet 700 nm – 1 mm.

For hver laser skal det finnes en informasjonsperm(HMSRV3404B) som skal inneholde:
- Generell informasjon
- Navn på instrumentansvarlig og stedfortreder, og lokal strålevernskoordinator
- Sentrale data om apparaturen
- Instrumentspesifikk dokumentasjon
- Referanser til (evt kopier av) datablader, strålevernbestemmelser, o.l.
- Vurderinger av risikomomenter
- Instruks for brukere
- Instruks for praktisk bruk; oppstart, drift, avstenging, sikkerhetsforholdsregler, loggføring, avlåsing, evt. bruk av strålingsmåler, osv.
- Nødprosedyrer

Se ellers retningslinjen til NTNU for laser: http://www.ntnu.no/hms/retningslinjer/HMSR34B.pdf

7.6 Bruk og behandling av kjemikalier.

Her forstås kjemikalier som grunnstoff som kan utgjøre en fare for arbeidstakers sikkerhet og helse.

Se ellers: http://www.lovdata.no/cgi-wift/ldles?doc=/sf/sf/sf-20010430-0443.html

Sikkerhetsdatablar skal være i forøkenes HMS perm og kjemikaliene registrert i Stoffkartoteket.

Kapittel 8 Vurdering av operasjonell sikkerhet

Sikrer at etablerte prosedyrer dekker alle identifiserte risikoforhold som må håndteres gjennom operasjonelle barrierer og at operatører og teknisk utførende har tilstrekkelig kompetanse.

8.1 Prosedyre Hazop

Prosedyre-HAZOP gjennomføres som en systematisk gjennomgang av den aktuelle prosedyren ved hjelp av fastlagt HAZOP-metodikk og definerte ledeord. Prosedyren brytes ned i enkeltstående arbeidsoperasjoner (noder) og analyseres ved hjelp av ledeordene for å avdekke mulige avvik, uklarheter eller kilder til mangelfull gjennomføring og feil.

8.2 Drifts og nødstopp prosedyrer

Utarbeides for alle forsøksoppsetninger.

Driftsprosedyren skal stegvis beskrive gjennomføringen av et forsøk, inndelt i oppstart, under drift og avslutning. Prosedyren skal beskrive forutsetninger og tilstand for start, driftsparametere med hvor store avvik som tillates før forsøket avbrytes og hvilken tilstand riggen skal forlates.

Nødstopp-prosedyre beskriver hvordan en nødstopp skal skje, (utført av uinnvidde),
hva som skjer, (strøm/gass tilførsel) og
hvilke hendelser som skal aktivere nødstopp, (brannalarm, lekkasje).

Kapittel 9 Risikomatrise Tallfesting av restrisiko

For å synliggjøre samlet risiko, jevnfør skjema for risikovurdering, plottes hver enkelt aktivitets verdi for sannsynlighet og konsekvens inn i risikomatrisen. Bruk aktivitetens IDnr. Eksempel: Hvis aktivitet med IDnr. 1 har fått en risikoverdi D3 (sannsynlighet 3 x konsekvens D) settes aktivitetens IDnr i risikomatrisens felt for 3D. Slik settes alle aktivitetenes risikoverdier (IDnr) inn i risikomatrisen.

I risikomatrisen er ulike grader av risiko merket med rød, gul eller grønn. Når en aktivitets risiko havner på rød (= uakseptabel risiko), skal risikoreduserende tiltak gjennomføres. Ny vurdering gjennomføres etter at tiltak er iverksatt for å se om risikoverdien er kommet ned på akseptabelt nivå.

KONSEKVENS	Svært alvorlig	E1	E2	E3	E4	E5
	Alvorlig	D1	D2	D3	D4	D5
	Moderat	C1	C2	C3	C4	C5
	Liten	B1	B2	B3	B4	B5
	Svært liten	A1	A2	A3	A4	A5
		Svært liten	Liten	Middels	Stor	Svært Stor
		SANSYNLIGHET				

Prinsipp over akseptkriterium. Forklaring av fargene som er brukt i risikomatrisen.

Farge		Beskrivelse
Rød		Uakseptabel risiko. Tiltak skal gjennomføres for å redusere risikoen.
Gul		Vurderingsområde. Tiltak skal vurderes.
Grønn		Akseptabel risiko. Tiltak kan vurderes ut fra andre hensyn.

Appendix B

Sensor locations and BEP from Francis-99

To compare pressure and strain results from the laboratory measurements and the simulations, accurate locations of the sensors are needed. The laboratory coordinates of each sensor are listed in the tables below:

Name	x [mm]	y [mm]	z [mm]	Uncertainty + - [mm]
PT10	100,3	218,5	21,7	0,1
PT11	180,5	158,8	21,7	0,1
PT12	84,3	132,8	-9,5	0,1
PT13	25,7	118,9	-31,6	0,1
PT14	-17,4	85,2	-59,6	0,1
PT20	213,9	246	-29,4	0,1
PT21	-320	62,2	-29,4	0,1
PT30	-101	149	-306	2
PT31	101	-149	-306	2
PT32	-109	162	-556	2
PT33	109	-162	-556	2
PT02	-880	688	-151	3
PT03	2553	99	-906	4

Figure B.1: Coordinates of pressure sensors

Name	x [mm]	y [mm]	z [mm]	Uncertainty + - [mm]
Strain1	-69,6	24	-87	0,1
Strain2	-69,9	22,9	-88	0,1

The strain gage lies in between point strain1 and strain2

Figure B.2: Coordinates of strain gage sensor

The following data is collected from the Francis-99 workshop 2 [2]. Figure B.3 shows acquired flow parameters during BEP operating point, with corresponding uncertainties. The uncertainty in hydraulic efficiency is the total uncertainty. This was used as a base when deciding on which operating point to run the experiment at.

Parameter	BEP	Uncertainty (%)
Guide vane angle ($^\circ$)	9.84	± 0.04-degree
Net head (m)	11.94	± 0.011%
Discharge ($m^3 s^{-1}$)	0.200	± 0.1%
Torque to the generator (Nm)	616.13	± 0.03%
Friction torque (Nm)	4.52	± 1.5%
Runner angular speed (rpm)	332.59	± 0.05%
Casing inlet pressure-abs (kPa)	215.57	± 0.047%
Draft tube outlet pressure-abs (kPa)	96.35	± 0.001%
Hydraulic efficiency (%)	92.39	± 0.14%
Water density (kg m^{-3})	999.8	± 0.01%
Kinematic viscosity ($m^2 s^{-1}$)	9.57E-7	--
Gravity (m s^{-2})	9.82	--

Figure B.3: Best efficiency point from the second Francis-99 workshop [2]

Appendix C

Error analysis

According to IEC60193 [42], the error in a measurement is defined as the difference between the measured value and the true, physical value of the measurement. All measurements of a physical size have an uncertainty that come from systematic and random errors. This uncertainty is defined as the area where the true value is expected to lie within. IEC60193 have set this probability to be the 95% confidence interval. There are three types of errors to be considered:

- Spurious errors
- Random errors
- Systematic errors

Spurious errors can be human errors or instrument malfunction, which invalidate a measurement. If the error is too small to make the results obviously invalid, the point should be repeated or some rejection criteria may be applied.

Random errors are caused by many, small, independent influences that prevent a set of measured values for a system with unchanged input value from delivering the same reading for the measured size. As a consequence, the measurements deviate from their mean value in accordance with the probability laws, such that the distribution normally approaches Gaussian distribution as the number of measurements increases. Random errors are dependent on the care taken during the measurements, the number of measurements and the operating conditions. The area of uncertainty for the random errors is estimated on the basis of statistical methods. When the number of measurements is low, the statistical results that are based on the assumption of a normal distribution, must be corrected by the means of the Student's t value. This is a factor which compensates for the increasing uncertainty in the standard deviation for a given confidence interval, when the sample size is reduced.

Systematic errors are errors which cannot be reduced by increasing the amount of measurements if the instruments used and the conditions for the measurements

stay unchanged. They are dependent on remaining errors of the instruments or the measurement system at the beginning of the tests. Estimation of uncertainty associated with systematic errors can not be experimentally evaluated without a change of equipment or by changing the conditions for the measurements. The alternative is to make subjective judgements based on experience and consideration of the equipment being used. To estimate the uncertainty, primarily the sources which can have affected the measured values needs to be identified. The main sources of uncertainty for an instrument are hysteresis, linearity, accuracy, zero offset, and drift. Next step is to assign limits for the uncertainty that can be accounted for in each single influence. Even so, the possible values of systematic components essentially have a Gaussian distribution, such that the calculation of the systematic uncertainty from the individual systematic uncertainties is done by the root-sum-square method.

Total uncertainty in a measurement is obtained by combining systematic and random uncertainties. Together these defines the range where the true value of the measurement lays with a 95% probability. Assuming that both the systematic and the random errors have the same probability distribution, they can be combined through the root-sum-square method.

C.1   Determination of uncertainties in model tests

The different sources of errors that contribute to the uncertainty during calibration of an instrument are listed in Table C.1, and are defined by IEC 60193. X indicates the property measured by the instrument.

Error	Description
$\pm f_{X_a}$	Systematic error of the primary calibration method
$\pm f_{X_b}$	Random error of the primary calibration method
$\pm f_{X_c}$	Systematic error (repeatability) of the secondary instrument
$\pm f_{X_d}$	Random error of the secondary instrument
$\pm f_{X_e}$	Physical phenomena and external influences
$\pm f_{X_f}$	Error in physical properties

Table C.1: Component errors in the calibration of an instrument

The uncertainties of the test itself may be separated into the errors given by Table C.2.

Error	Description
$\pm f_{X_{cal}}$	Systematic error in the calibration
$\pm f_{X_h}$	Additional systematic error in the instrument
$\pm f_{X_j}$	Error in physical properties
$\pm f_{X_{k_s}}$	Systematic errors due to physical phenomena and external influences
$\pm f_{X_{k_r}}$	Random errors due to physical phenomena and external influences
$\pm f_{X_l}$	Random error in the repeatability of the secondary instrument

Table C.2: Component errors in the test

Appendix D

Calibration reports

CALIBRATION REPORT

CALIBRATION PROPERTIES
Calibrated by: Katarina Kloster and Ingebjørg Valkvæ
Type/Producer: Kulite HKM-375M
SN: 8240-4-888
Range: 0-1.7 bar a
Unit: kPa

CALIBRATION SOURCE PROPERTIES
Type/Producer: Pressurements deadweight tester P3023-6-P
SN: 66611
Uncertainty [%]: 0,008

POLY FIT EQUATION:
Y= + 230.02390217E-3X^0 + 22.55034497E+3X^1

CALIBRATION SUMARY:
Max Uncertainty   : 0.194185 [%]
Max Uncertainty   : 0.221837 [kPa]
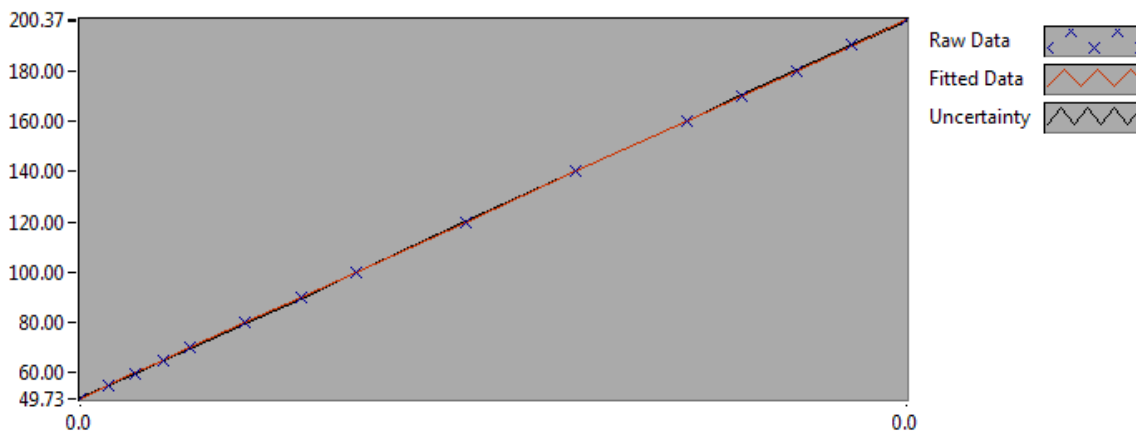RSQ   : 0.999991
Calibration points : 15
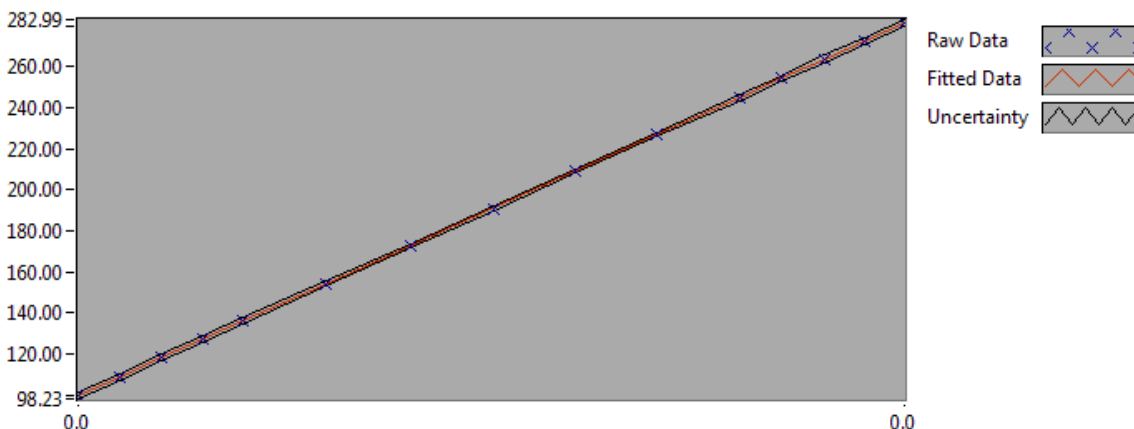
Figure 1 : Calibration chart (The uncertainty band is multiplied by 10)

_____
Katarina Kloster and Ingebjørg Valkvæ

CALIBRATION VALUES

Value [kPa]	Voltage [V]	Best Poly Fit [kPa]	Deviation [kPa]	Uncertainty [%]	Uncertainty [kPa]
100.000000	0.004422	99.947240	0.052760	0.194185	0.194185
110.015107	0.004868	110.002871	0.012236	0.164734	0.181233
120.030214	0.005313	120.051003	-0.020789	0.140486	0.168626
130.045321	0.005753	129.962240	0.083081	0.121674	0.158232
140.060428	0.006196	139.948236	0.112193	0.107029	0.149906
160.090643	0.007084	159.966808	0.123835	0.087311	0.139776
180.120857	0.007987	180.332795	-0.211938	0.069897	0.125899
200.151071	0.008875	200.374684	-0.223613	0.060147	0.120385
220.181285	0.009764	220.401110	-0.219825	0.051930	0.114340
240.211499	0.010638	240.128541	0.082958	0.052992	0.127294
260.241714	0.011522	260.050969	0.190744	0.071828	0.186926
270.256821	0.011970	270.157619	0.099202	0.059701	0.161345
280.271928	0.012439	280.722866	-0.450939	0.079151	0.221837
290.287035	0.012864	290.320206	-0.033171	0.070310	0.204100
300.302142	0.013289	299.898876	0.403266	0.064545	0.193829

COMMENTS:

The uncertainty is calculated with 95% confidence. The uncertainty includes the randomness in the calibrated instrument during the calibration, systematic uncertainty in the instrument or property which the instrument under calibration is compared with (dead weight manometer, calibrated weights etc.), and due to regression analysis to fit the calibration points to a linear calibration equation.The calculated uncertainty can be used as the total systematic uncertianty of the calibrated instrument with the given calibration equation.

CALIBRATION REPORT

CALIBRATION PROPERTIES
Calibrated by: Katarina Kloster and Ingebjørg Valkvæ
Type/Producer: Kulite HKM-375M
SN: 8240-4-887
Range: 0-1.7 bar a
Unit: kPa

CALIBRATION SOURCE PROPERTIES
Type/Producer: Pressurements deadweight tester P3023-6-P
SN: 66611
Uncertainty [%]: 0,008

POLY FIT EQUATION:
Y= -4.25163513E+0X^0 + 22.85839685E+3X^1

CALIBRATION SUMARY:
Max Uncertainty   : 0.048805 [%]
Max Uncertainty   : 0.047047 [kPa]
RSQ   : 1.000000
Calibration points : 15

Figure 1 : Calibration chart (The uncertainty band is multiplied by 10)

_____
Katarina Kloster and Ingebjørg Valkvæ

CALIBRATION VALUES

Value [kPa]	Voltage [V]	Best Poly Fit [kPa]	Deviation [kPa]	Uncertainty [%]	Uncertainty [kPa]
49.924465	0.002370	49.923452	0.001012	0.038917	0.019429
54.932018	0.002589	54.927796	0.004222	0.033517	0.018412
59.939572	0.002810	59.978672	-0.039100	0.048805	0.029253
64.947125	0.003027	64.940910	0.006215	0.025936	0.016845
69.954679	0.003245	69.933418	0.021261	0.021804	0.015253
79.969786	0.003683	79.944248	0.025538	0.022136	0.017702
89.984893	0.004122	89.979020	0.005873	0.038883	0.034989
100.000000	0.004560	99.989738	0.010262	0.011933	0.011933
120.030214	0.005437	120.039231	-0.009017	0.009671	0.011608
140.060428	0.006314	140.082665	-0.022237	0.011533	0.016153
160.090643	0.007191	160.120424	-0.029781	0.016164	0.025877
170.105750	0.007628	170.123544	-0.017795	0.027658	0.047047
180.120857	0.008066	180.119551	0.001306	0.024571	0.044258
190.135964	0.008503	190.124050	0.011914	0.012618	0.023991
200.151071	0.008941	200.120744	0.030327	0.012288	0.024594

COMMENTS:

The uncertainty is calculated with 95% confidence. The uncertainty includes the randomness in the calibrated instrument during the calibration, systematic uncertainty in the instrument or property which the instrument under calibration is compared with (dead weight manometer, calibrated weights etc.), and due to regression analysis to fit the calibration points to a linear calibration equation.The calculated uncertainty can be used as the total systematic uncertianty of the calibrated instrument with the given calibration equation.

CALIBRATION REPORT

_____

CALIBRATION PROPERTIES
Calibrated by: Katarina Kloster
Type/Producer: Kulite XTM-190SM
SN: 8317-1-201
Range: 0-3,5bar a
Unit: kPa

CALIBRATION SOURCE PROPERTIES
Type/Producer: Pressurements deadweight tester P3023-6-P
SN: 66611
Uncertainty [%]: 0,008

POLY FIT EQUATION:
Y= -6,79035476E+0X^0 + 37,37745937E+0X^1

CALIBRATION SUMARY:
Max Uncertainty   : 0,412824 [%]
Max Uncertainty   : 0,255793 [kPa]
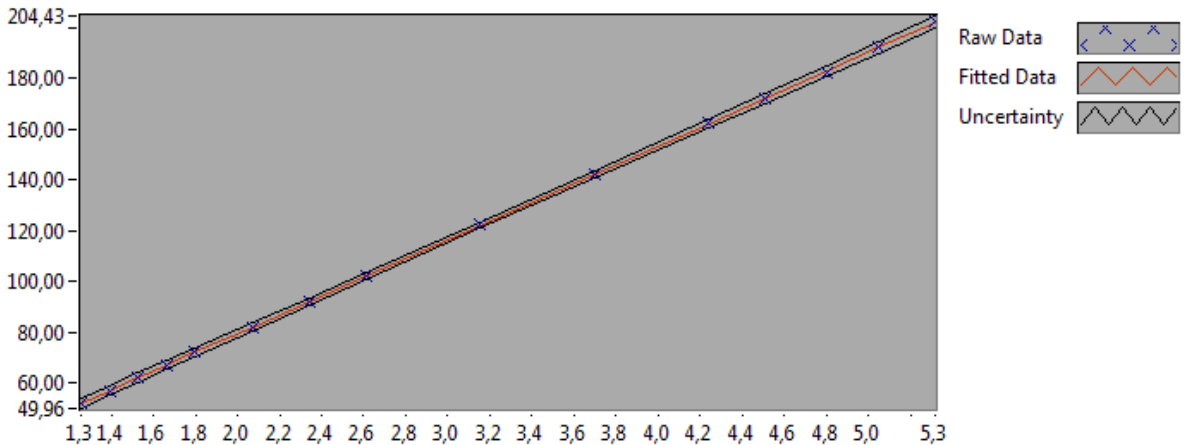RSQ   : 0,999978
Calibration points : 15
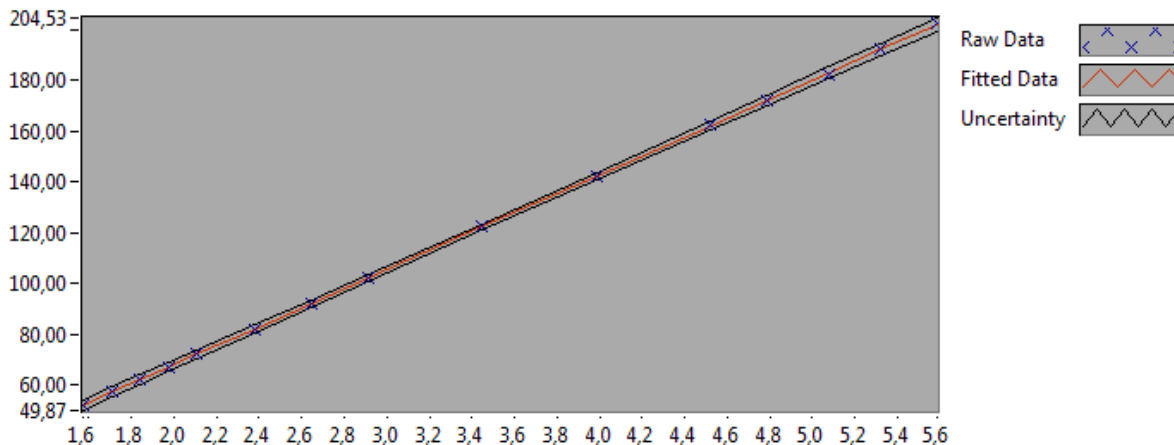
Figure 1 : Calibration chart (The uncertainty band is multiplied by 10)

_____
Katarina Kloster

_____

CALIBRATION VALUES

Value [kPa]	Voltage [V]	Best Poly Fit [kPa]	Deviation [kPa]	Uncertainty [%]	Uncertainty [kPa]
52,024465	1,573476	52,022183	0,002281	0,412824	0,214769
57,032018	1,707366	57,026649	0,005369	0,359201	0,204860
62,039572	1,841416	62,037098	0,002473	0,314763	0,195277
67,047125	1,975587	67,052056	-0,004930	0,277559	0,186095
72,054679	2,109498	72,057322	-0,002643	0,246191	0,177392
82,069786	2,377531	82,075730	-0,005944	0,196966	0,161649
92,084893	2,645303	92,084357	0,000536	0,161537	0,148751
102,100000	2,913199	102,097618	0,002382	0,136593	0,139461
122,130214	3,448776	122,116143	0,014071	0,110093	0,134457
142,160428	3,983703	142,110359	0,050069	0,104357	0,148355
162,190643	4,517960	162,079517	0,111125	0,109034	0,176843
172,205750	4,784111	172,027565	0,178184	0,113004	0,194600
182,220857	5,079663	183,074541	-0,853684	0,118517	0,215962
192,235964	5,318855	192,014942	0,221022	0,121911	0,234357
202,251071	5,585231	201,971383	0,279688	0,126473	0,255793

COMMENTS:

———————————

The uncertainty is calculated with 95% confidence. The uncertainty includes the randomness in the calibrated instrument during the calibration, systematic uncertainty in the instrument or property which the instrument under calibration is compared with (dead weight manometer, calibrated weights etc.), and due to regression analysis to fit the calibration points to a linear calibration equation.The calculated uncertainty can be used as the total systematic uncertianty of the calibrated instrument with the given calibration equation.

CALIBRATION REPORT

_____

CALIBRATION PROPERTIES
Calibrated by: Katarina Kloster
Type/Producer: Kulite XTM-190SM
SN: 8317-1-202
Range: 0-3,5 bar a
Unit: kPa

CALIBRATION SOURCE PROPERTIES
Type/Producer: Pressurements deadweight tester P3223-1
SN: 66256
Uncertainty [%]: 0,01

POLY FIT EQUATION:
Y= + 5,63531073E+0X^0 + 36,92939840E+0X^1

CALIBRATION SUMARY:
Max Uncertainty   : 0,397652 [%]
Max Uncertainty   : 0,246463 [kPa]
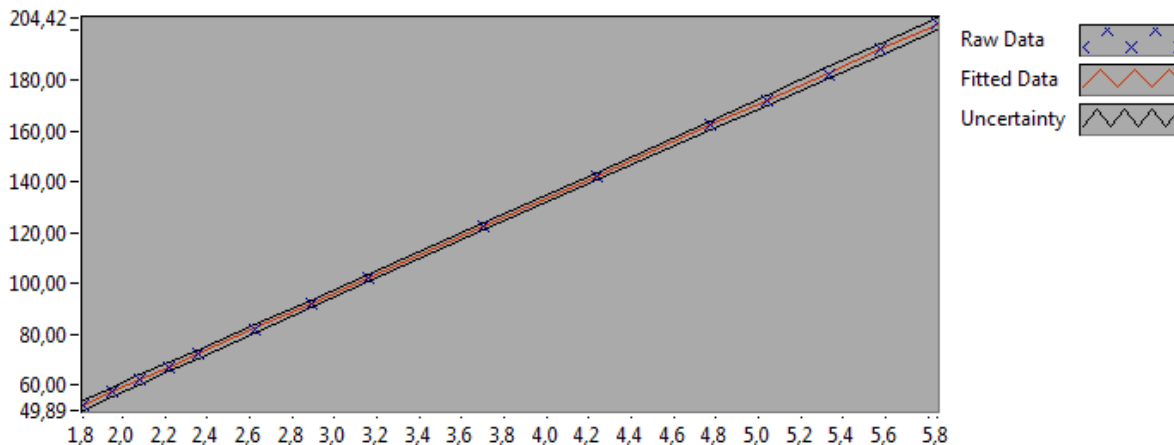RSQ   : 0,999979
Calibration points : 15

Figure 1 : Calibration chart (The uncertainty band is multiplied by 10)

_____

Katarina Kloster

_____

CALIBRATION VALUES

Value [kPa]	Voltage [V]	Best Poly Fit [kPa]	Deviation [kPa]	Uncertainty [%]	Uncertainty [kPa]
52,024465	1,256370	52,032286	-0,007822	0,397652	0,206876
57,032018	1,391836	57,034973	-0,002955	0,346012	0,197338
62,039572	1,527381	62,040570	-0,000998	0,303218	0,188115
67,047125	1,662928	67,046244	0,000881	0,267408	0,179289
72,054679	1,798475	72,051911	0,002768	0,237190	0,170906
82,069786	2,069613	82,064873	0,004913	0,189777	0,155750
92,084893	2,340708	92,076251	0,008641	0,155644	0,143324
102,100000	2,611900	102,091213	0,008787	0,131613	0,134377
122,130214	3,154053	122,112587	0,017627	0,106088	0,129565
142,160428	3,695751	142,117161	0,043267	0,100571	0,142972
162,190643	4,236547	162,088431	0,102212	0,105101	0,170464
172,205750	4,506808	172,069010	0,136739	0,108910	0,187550
182,220857	4,803963	183,042758	-0,821901	0,114162	0,208028
192,235964	5,046814	192,011100	0,224864	0,117468	0,225815
202,251071	5,316436	201,968094	0,282976	0,121860	0,246463

COMMENTS:

The uncertainty is calculated with 95% confidence. The uncertainty includes the randomness in the calibrated instrument during the calibration, systematic uncertainty in the instrument or property which the instrument under calibration is compared with (dead weight manometer, calibrated weights etc.), and due to regression analysis to fit the calibration points to a linear calibration equation.The calculated uncertainty can be used as the total systematic uncertianty of the calibrated instrument with the given calibration equation.

CALIBRATION REPORT

_____

CALIBRATION PROPERTIES
Calibrated by: Katarina Kloster
Type/Producer: Kulite XTM-190SM
SN: 8317-1-203
Range: 0-3,5 bar a
Unit: kPa

CALIBRATION SOURCE PROPERTIES
Type/Producer: Pressurements deadweight tester P3223-1
SN: 66256
Uncertainty [%]: 0,01

POLY FIT EQUATION:
$Y = -15,59293487E+0X^0 + 37,22867417E+0X^1$

CALIBRATION SUMARY:
Max Uncertainty   : 0,398919 [%]
Max Uncertainty   : 0,247063 [kPa]
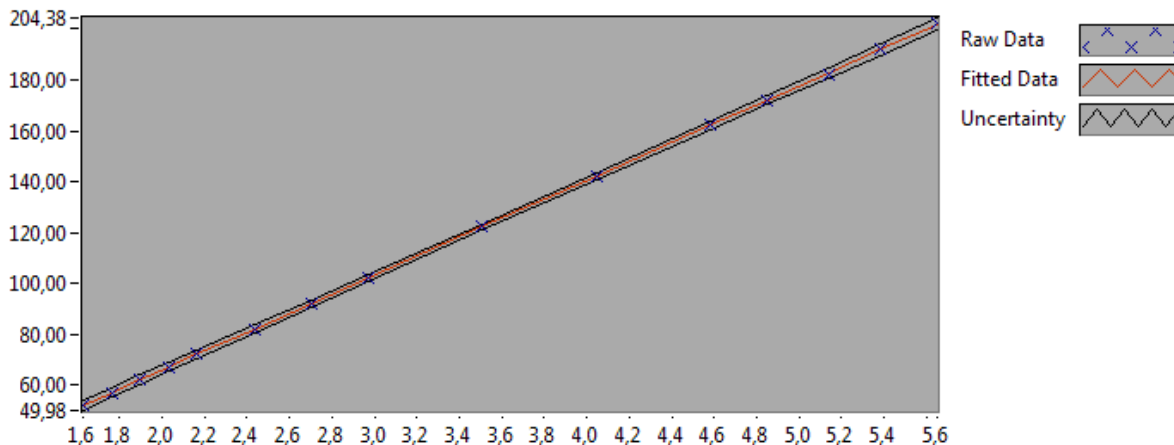RSQ   : 0,999979
Calibration points : 15

Figure 1 : Calibration chart (The uncertainty band is multiplied by 10)

_____

Katarina Kloster

_____

CALIBRATION VALUES

Value [kPa]	Voltage [V]	Best Poly Fit [kPa]	Deviation [kPa]	Uncertainty [%]	Uncertainty [kPa]
52,024465	1,814818	51,970319	0,054146	0,398919	0,207535
57,032018	1,950244	57,012067	0,019951	0,346983	0,197892
62,039572	2,085131	62,033734	0,005838	0,304028	0,188618
67,047125	2,219728	67,044592	0,002533	0,268106	0,179757
72,054679	2,354344	72,056172	-0,001493	0,237794	0,171342
82,069786	2,623907	82,091649	-0,021863	0,190226	0,156118
92,084893	2,893109	92,113675	-0,028782	0,156004	0,143656
102,100000	3,161908	102,120721	-0,020721	0,131935	0,134706
122,130214	3,699622	122,139075	-0,008861	0,106367	0,129906
142,160428	4,236823	142,138375	0,022054	0,100845	0,143362
162,190643	4,773052	162,101471	0,089172	0,105357	0,170880
172,205750	5,040319	172,051455	0,154295	0,109149	0,187961
182,220857	5,335225	183,030432	-0,809576	0,114433	0,208520
192,235964	5,575989	191,993727	0,242237	0,117751	0,226360
202,251071	5,843424	201,950000	0,301071	0,122156	0,247063

COMMENTS:

———————————

The uncertainty is calculated with 95% confidence. The uncertainty includes the randomness in the calibrated instrument during the calibration, systematic uncertainty in the instrument or property which the instrument under calibration is compared with (dead weight manometer, calibrated weights etc.), and due to regression analysis to fit the calibration points to a linear calibration equation.The calculated uncertainty can be used as the total systematic uncertianty of the calibrated instrument with the given calibration equation.

CALIBRATION REPORT

_____

CALIBRATION PROPERTIES
Calibrated by: Katarina Kloster
Type/Producer: Kulite XTM-190SM
SN: 8317-1-204
Range: 0-3,5bar a
Unit: kPa

CALIBRATION SOURCE PROPERTIES
Type/Producer: Pressurements deadweight tester P3223-1
SN: 66256
Uncertainty [%]: 0,01

POLY FIT EQUATION:
Y= -8,69549532E+0X^0 + 37,28439544E+0X^1

CALIBRATION SUMARY:
Max Uncertainty   : 0,390050 [%]
Max Uncertainty   : 0,241706 [kPa]
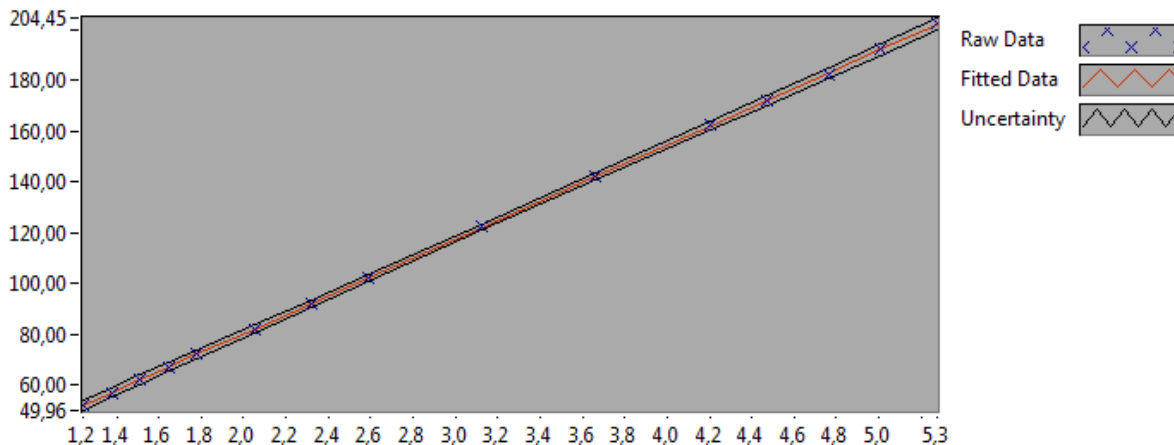RSQ   : 0,999980
Calibration points : 15

Figure 1 : Calibration chart (The uncertainty band is multiplied by 10)

_____
Katarina Kloster

_____

CALIBRATION VALUES

Value [kPa]	Voltage [V]	Best Poly Fit [kPa]	Deviation [kPa]	Uncertainty [%]	Uncertainty [kPa]
52,024465	1,628072	52,006172	0,018293	0,390050	0,202922
57,032018	1,762727	57,026725	0,005293	0,339339	0,193532
62,039572	1,897090	62,036351	0,003221	0,297364	0,184483
67,047125	2,031375	67,043106	0,004019	0,262243	0,175826
72,054679	2,165738	72,052747	0,001932	0,232601	0,167600
82,069786	2,434635	82,078403	-0,008617	0,186090	0,152724
92,084893	2,703210	92,092051	-0,007158	0,152624	0,140544
102,100000	2,971733	102,103759	-0,003759	0,129071	0,131782
122,130214	3,508752	122,126199	0,004015	0,104054	0,127082
142,160428	4,044996	142,119741	0,040688	0,098644	0,140233
162,190643	4,580491	162,085326	0,105317	0,103065	0,167162
172,205750	4,848974	172,095584	0,110166	0,106921	0,184124
182,220857	5,142000	183,020852	-0,799995	0,111955	0,204006
192,235964	5,382836	192,000301	0,235662	0,115197	0,221450
202,251071	5,649968	201,960148	0,290923	0,119508	0,241706

COMMENTS:

———————————

The uncertainty is calculated with 95% confidence. The uncertainty includes the randomness in the calibrated instrument during the calibration, systematic uncertainty in the instrument or property which the instrument under calibration is compared with (dead weight manometer, calibrated weights etc.), and due to regression analysis to fit the calibration points to a linear calibration equation.The calculated uncertainty can be used as the total systematic uncertianty of the calibrated instrument with the given calibration equation.

CALIBRATION REPORT

_____

CALIBRATION PROPERTIES
Calibrated by: Katarina Kloster
Type/Producer: Kulite XTM-190SM
SN: 8317-1-205
Range: 0-3,5 bar a
Unit: kPa

CALIBRATION SOURCE PROPERTIES
Type/Producer: Pressurements deadweight tester P3223-1
SN: 66256
Uncertainty [%]: 0,01

POLY FIT EQUATION:
Y= + 5,87661454E+0X^0 + 37,17518896E+0X^1

CALIBRATION SUMARY:
Max Uncertainty   : 0,397164 [%]
Max Uncertainty   : 0,246198 [kPa]
RSQ   : 0,999979
Calibration points : 15

Figure 1 : Calibration chart (The uncertainty band is multiplied by 10)

_____
Katarina Kloster

_____

CALIBRATION VALUES

Value [kPa]	Voltage [V]	Best Poly Fit [kPa]	Deviation [kPa]	Uncertainty [%]	Uncertainty [kPa]
52,024465	1,241435	52,027208	-0,002744	0,397164	0,206623
57,032018	1,376092	57,033111	-0,001093	0,345577	0,197090
62,039572	1,510832	62,042062	-0,002491	0,302827	0,187873
67,047125	1,645553	67,050344	-0,003219	0,267057	0,179054
72,054679	1,780273	72,058608	-0,003929	0,236873	0,170678
82,069786	2,049690	82,074230	-0,004445	0,189520	0,155539
92,084893	2,318990	92,085523	-0,000630	0,155435	0,143132
102,100000	2,588248	102,095209	0,004791	0,131444	0,134204
122,130214	3,126414	122,101637	0,028577	0,105952	0,129399
142,160428	3,664240	142,095420	0,065008	0,100428	0,142769
162,190643	4,201565	162,070604	0,120038	0,104951	0,170221
172,205750	4,470140	172,054923	0,150827	0,108760	0,187292
182,220857	4,765781	183,045421	-0,824565	0,114021	0,207770
192,235964	5,007269	192,022798	0,213165	0,117331	0,225553
202,251071	5,275393	201,990363	0,260708	0,121729	0,246198

COMMENTS:

———————————

The uncertainty is calculated with 95% confidence. The uncertainty includes the randomness in the calibrated instrument during the calibration, systematic uncertainty in the instrument or property which the instrument under calibration is compared with (dead weight manometer, calibrated weights etc.), and due to regression analysis to fit the calibration points to a linear calibration equation.The calculated uncertainty can be used as the total systematic uncertianty of the calibrated instrument with the given calibration equation.

CALIBRATION REPORT

_____

CALIBRATION PROPERTIES
Calibrated by: Katarina Kloster
Type/Producer: Kulite
SN: V4537-34
Range: 0-10 bar a
Unit: kPa

CALIBRATION SOURCE PROPERTIES
Type/Producer: Pressurements deadweight tester P3023-6-P
SN: 66611
Uncertainty [%]: 0,008

POLY FIT EQUATION:
Y= + 98,86246121E+0X^0 -70,35007630E+3X^1

CALIBRATION SUMARY:
Max Uncertainty   : 0,039565 [%]
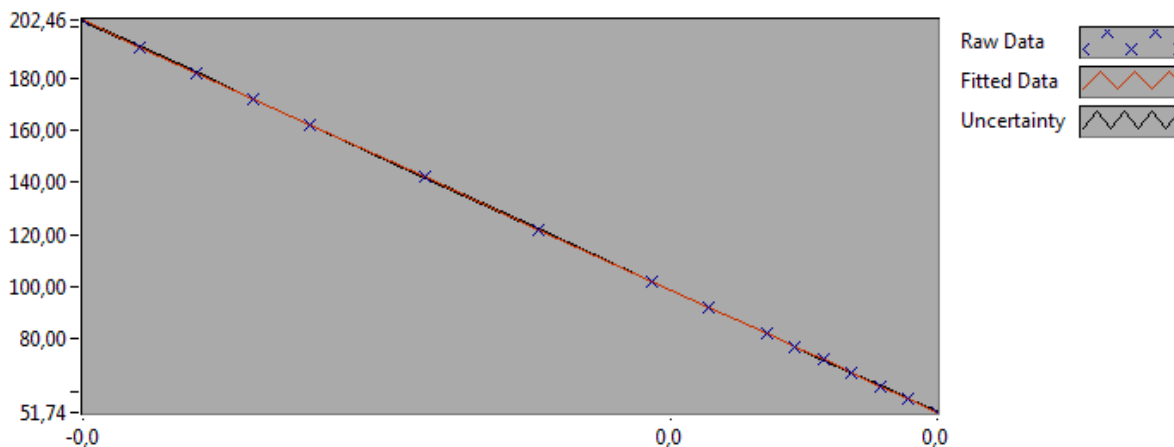Max Uncertainty   : 0,029554 [kPa]
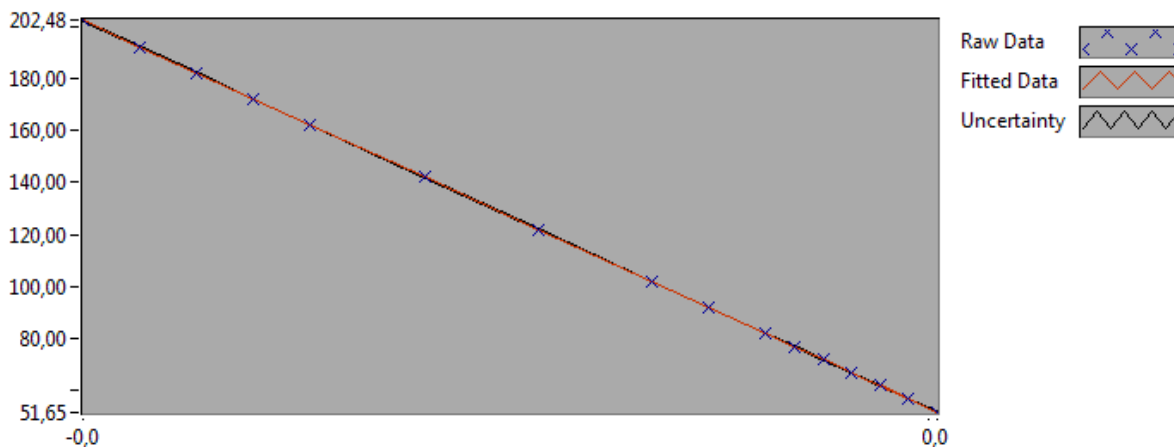RSQ   : 1,000000
Calibration points : 16

Figure 1 : Calibration chart (The uncertainty band is multiplied by 10)

_____
Katarina Kloster

_____

CALIBRATION VALUES

Value [kPa]	Voltage [V]	Best Poly Fit [kPa]	Deviation [kPa]	Uncertainty [%]	Uncertainty [kPa]
51,954465	0,000667	51,945614	0,008851	0,039565	0,020556
56,962018	0,000596	56,961839	0,000179	0,034545	0,019677
61,969572	0,000525	61,963083	0,006489	0,030565	0,018941
66,977125	0,000453	66,976076	0,001049	0,027085	0,018141
71,984679	0,000382	71,985625	-0,000946	0,024602	0,017709
76,992232	0,000311	76,994447	-0,002215	0,023104	0,017788
81,999786	0,000240	81,999547	0,000239	0,020736	0,017004
92,014893	0,000097	92,016276	-0,001383	0,017514	0,016115
102,030000	-0,000045	102,031898	-0,001898	0,015502	0,015816
122,060214	-0,000330	122,071054	-0,010840	0,013133	0,016030
142,090428	-0,000615	142,099123	-0,008695	0,013976	0,019858
162,120643	-0,000899	162,128092	-0,007450	0,015579	0,025257
172,135750	-0,001042	172,139068	-0,003318	0,013677	0,023543
182,150857	-0,001184	182,149320	0,001536	0,013885	0,025292
192,165964	-0,001326	192,159500	0,006464	0,014314	0,027506
202,181071	-0,001468	202,169133	0,011937	0,014618	0,029554

COMMENTS:

―――――――――

The uncertainty is calculated with 95% confidence. The uncertainty includes the randomness in the calibrated instrument during the calibration, systematic uncertainty in the instrument or property which the instrument under calibration is compared with (dead weight manometer, calibrated weights etc.), and due to regression analysis to fit the calibration points to a linear calibration equation.The calculated uncertainty can be used as the total systematic uncertianty of the calibrated instrument with the given calibration equation.

CALIBRATION REPORT

_____

CALIBRATION PROPERTIES
Calibrated by: Einar Agnalt and Katarina Kloster
Type/Producer: Kulite
SN: V4537-33
Range: 0-10 bar a
Unit: kPa

CALIBRATION SOURCE PROPERTIES
Type/Producer: Pressurements deadweight tester P3023-6-P
SN: 66611
Uncertainty [%]: 0,008

POLY FIT EQUATION:
Y= + 53,37801232E+0X^0 -77,26353937E+3X^1

CALIBRATION SUMARY:
Max Uncertainty   : 0,052726 [%]
Max Uncertainty   : 0,030448 [kPa]
RSQ   : 1,000000
Calibration points : 16

Figure 1 : Calibration chart (The uncertainty band is multiplied by 10)

_____
Einar Agnalt

_____

CALIBRATION VALUES

Value [kPa]	Voltage [V]	Best Poly Fit [kPa]	Deviation [kPa]	Uncertainty [%]	Uncertainty [kPa]
51,954465	0,000019	51,919861	0,034604	0,052726	0,027393
61,969572	-0,000111	61,942501	0,027070	0,031512	0,019528
56,962018	-0,000047	56,971794	-0,009776	0,037707	0,021479
66,977125	-0,000176	66,967565	0,009560	0,027897	0,018685
71,984679	-0,000241	71,996309	-0,011631	0,024981	0,017983
76,992232	-0,000306	77,016601	-0,024369	0,022538	0,017353
81,999786	-0,000371	82,016920	-0,017134	0,020525	0,016831
92,014893	-0,000500	92,024780	-0,009887	0,017451	0,016058
102,030000	-0,000630	102,024453	0,005547	0,015408	0,015721
122,060214	-0,000889	122,077012	-0,016797	0,013541	0,016528
142,090428	-0,001148	142,099463	-0,009035	0,014582	0,020720
162,120643	-0,001407	162,121678	-0,001035	0,013619	0,022079
172,135750	-0,001537	172,134553	0,001196	0,013961	0,024033
182,150857	-0,001667	182,147625	0,003231	0,014328	0,026098
192,165964	-0,001796	192,154310	0,011654	0,014900	0,028633
202,181071	-0,001926	202,174270	0,006801	0,015060	0,030448

COMMENTS:

The uncertainty is calculated with 95% confidence. The uncertainty includes the randomness in the calibrated instrument during the calibration, systematic uncertainty in the instrument or property which the instrument under calibration is compared with (dead weight manometer, calibrated weights etc.), and due to regression analysis to fit the calibration points to a linear calibration equation. The calculated uncertainty can be used as the total systematic uncertianty of the calibrated instrument with the given calibration equation.

WATERPOWER LABORATORY

Calibration Sheet

Calibration of weighing tank load cells

Date:
08.04,16

Operator:
Katarina, Ingebjørg, Helene, Joel

Unit: Weighing tank load cells, reg. nr. 4331-5/6/7

W_L	5126,075	[kg]

Coments:
Flow through pressure tank and the Gibson loop.
Controlled the flowrate by use of pump 2, 450rpm.
"Valve 1" 200‰ open
filling time 20 sec.

Manual Observation	Manual Observation	Displayed load increase	$k = \dfrac{W_L}{\Delta W}$	Weight midpoint	Estimated correction factor	Difference in real k and estimated k	
Weights off	Weights on	ΔW	k	Weight	k	Δk	Δk
[kg]	[kg]	[kg]	[-]	[kg]	[-]	[-]	[%]
2625,82	7756,3	5130,48	0,9991	5191,1	0,999146232	0,00000	0,000
7902,97	13034,78	5131,81	0,9989	10468,9	0,99891	0,00003	0,003
13165,14	18297,15	5132,01	0,9988	15731,1	0,99880	-0,00004	0,004
18407,37	23539,33	5131,96	0,9989	20973,4	0,99878	-0,00007	0,007
23653,33	28785,89	5132,56	0,9987	26219,6	0,99881	0,00008	0,008
28893,22	34025,46	5132,24	0,9988	31459,3	0,99887	0,00007	0,007
34125,44	39256,68	5131,24	0,9990	36691,1	0,99894	-0,00006	0,006
39334,05	44465,51	5131,46	0,9990	41899,8	0,99900	0,00005	0,005
44546,08	49676,85	5130,77	0,9991	47111,5	0,99905	-0,00004	0,004
49751,75	54882,07	5130,32	0,9992	52316,9	0,99909	-0,00008	0,008
54933,9	60064,61	5130,71	0,9991	57499,3	0,99913	0,00003	0,003
60126,97	65257,54	5130,57	0,9991	62692,3	0,99918	0,00006	0,006
65295,79	70425,54	5129,75	0,9993	67860,7	0,99927	-0,00001	0,001
73447,98	78576,29	5128,31	0,9996	76012,1	0,99956	-0,00001	0,001

$k = 7E-27w^4 - 1E-20w^3 + 5E-15w^2 - 8E-10w + 0.0999$
$R^2 = 0.6653$
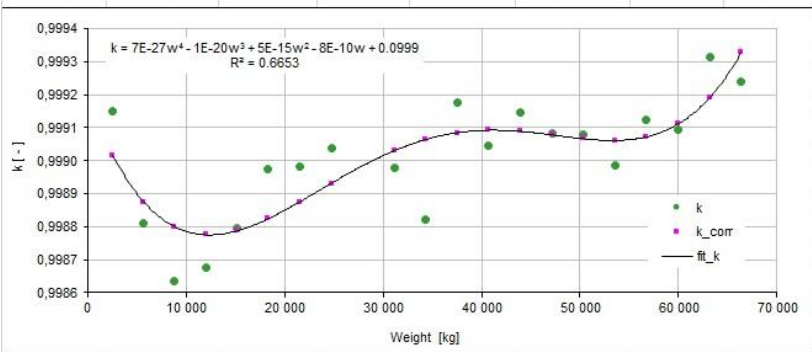
Calibration constants	a_1	3,88209E-22
	a_2	-6,73376E-17
	a_3	4,16853E-12
	a_4	-9,82556E-08
	b	9,99553E-01
	R^2	0,940917571

WATERPOWER LABORATORY
Calibration Sheet
Calibration of flow meter

NTNU

Calibrator: Weighing tank system

Unit: Flowmeter, Francisrigg

Date:	08.03.2016
Operator:	Rakel Ellingsen

Calibrator: Weighing tank system

Calibration constants for weighing tank correction

a_1	7.49E-22	
a_2	-1.07E-16	
a_3	5.04E-12	
a_4	-8.13E-08	
a_5	9.99E-01	

Corrected weight is calculated from formula where parameters a,b,c,d and e is achieved through substitution calibration

$$W = a \cdot \frac{mW^5}{5} + b \cdot \frac{mW^4}{4} + c \cdot \frac{mW^3}{3} + d \cdot \frac{mW^2}{2} + e \cdot mW$$

Density of water is calculated from formula

Density of air is calculated from formula

$$\rho_a = \frac{(p_{da} \cdot 3.4837 \cdot 10^3)}{(273.15 + \theta)}$$

Discharge is found from formula

$$Q = \frac{(\rho_{dc} - \frac{\rho_a}{\rho_s})}{\rho_w - \rho_a}$$

	nPoints	17
	S_{xy}	0.00039

Data table

Manual Observation before Weight [kg]	Manual Observation after Weight [kg]	Manual Observation Voltage [V]	Manual Observation Time [s]	Ambient pressure P_{amb} [kPa]	Water temp T_W [°C]	Air temp T_A [°C]	Calculated value before Weight [kg]	Calculated value after Weight [kg]	Differential weight Weight [kg]	Density of water ρ [kg/m³]	Density of air ρ [kg/m³]	Differential volume Volume [m³]	Calculated Flow Rate Q [m³/s]	Estimate Q [m³/s]	Deviation [%]	e_i	Outlier detection e_i/S_{xy}
14405.3	18802.3	5.320763	120.099	100.170	15.26	19.08	14389.2	18781.0	4391.7	999.1146	1.1950	4.40089	0.0366439	0.03729	-1.73900	-0.00065	-1.66921
8149.9	13547.2	5.651954	70.101	100.060	15.44	18.42	8141.4	13532.2	5390.7	999.0860	1.1964	5.40214	0.0700622	0.07621	-1.12148	-0.00085	2.19978
18802.3	24844.1	5.742822	70.100	100.160	15.29	19.11	18781.0	24816.0	6035.0	999.0998	1.1947	6.04765	0.08688	0.08688	-0.70542	0.00061	-1.57755
13547.2	19149.7	5.954272	50.102	100.060	15.41	18.33	13532.2	19128.0	5595.8	999.0908	1.1967	5.60760	0.1119236	0.11173	-0.17312	0.00019	0.49786
24844.1	30045.1	5.986709	45.101	100.150	15.22	18.96	24816.0	30011.7	5195.7	999.1209	1.1952	5.20648	0.1154404	0.11554	-0.08755	-0.00010	-0.26038
19149.7	25830.6	6.165786	45.101	100.100	15.38	18.44	19128.0	25801.5	6160.7	999.0956	1.1967	6.17371	0.1368864	0.13658	-0.22198	-0.00026	0.78036
30045.1	36177.2	6.424069	40.101	100.060	15.37	18.29	30011.7	36138.0	6673.5	999.0971	1.1969	6.68754	0.1667675	0.16693	0.09833	-0.00016	-0.42249
25830.6	31459.2	6.487957	35.101	100.140	15.25	19.07	25801.5	31424.4	6126.3	999.1161	1.1946	6.13904	0.1748964	0.17444	-0.26251	0.00046	1.17862
36177.2	30011.7	6.596432	35.101	100.060	15.37	18.29	36138.0	31424.4	5622.9	999.0971	1.1967	5.63471	0.1871893	0.18718	-0.00261	0.00000	0.01256
31459.2	37763.3	6.786332	30.102	100.060	15.38	18.34	31424.4	37722.6	6298.2	999.0956	1.1971	6.31147	0.2096693	0.20950	-0.08187	0.00017	0.44146
8650.1	8650.1	7.055631	30.102	100.100	15.29	18.60	8641.0	72311.1	7231.1	999.1098	1.1961	7.24621	0.2407297	0.24114	0.17039	-0.00041	-1.05757
15890.0	23812.4	7.245409	30.102	100.100	15.31	18.55	15872.1	23786.4	7913.3	999.1067	1.1963	7.92986	0.2634330	0.26344	0.00255	-0.00001	-0.01726
23812.4	31930.7	7.300698	30.100	100.100	15.32	18.55	23785.4	31895.4	8110.0	999.1051	1.1963	8.12703	0.2700010	0.26994	-0.02401	0.00006	-0.16683
31930.7	40676.0	7.477328	30.101	100.100	15.32	18.54	31895.4	40632.6	8737.2	999.1051	1.1963	8.75552	0.2908713	0.29069	-0.06224	0.00018	0.46069
40676.0	60126.8	7.547291	30.101	100.100	15.36	18.48	40632.6	60065.5	8981.4	999.0987	1.1966	9.00029	0.2990029	0.29891	-0.03074	0.00009	0.23649
60126.8	69114.8	7.689607	30.102	100.100	15.37	18.53	60065.5	69046.9	8981.4	999.0987	1.1964	9.50005	0.3155953	0.31563	0.01204	-0.00004	-0.09782
50637.9	60126.8	7.826172	30.101	100.100	15.33	18.50	50585.4	60065.5	9480.1	999.0972	1.1965	9.97363	0.3313389	0.33168	0.10277	-0.00034	-0.87738

Flow Meter Calibration Francis

$y = 0.11750071x - 0.58790103$

$R^2 = 0.99983316$

Axes: Flow rate [m3/s] (vertical, 0.00–0.35) vs Flow rate signal [V] (horizontal, 5.0–7.5)

Legend:
- Calibration Curve
- Linear (Calibration Curve)

Calibration constants

C_0	-0.587901026
C_1	0.11750071
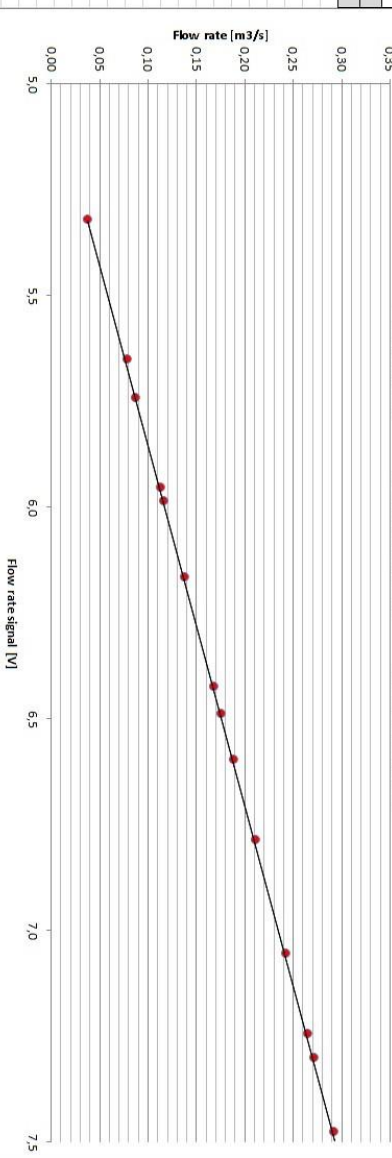
CALIBRATION REPORT

CALIBRATION PROPERTIES
Calibrated by: Rakel Ellingsen
Type/Producer: Krohne Optiflux
SN: xxxxxx
Range: 0 - 450 l/s
Unit: l/s

CALIBRATION SOURCE PROPERTIES
Type/Producer: Weighing method
SN: xxxxx
Uncertainty [%]: 0

POLY FIT EQUATION:
$Y = -147.80000000E\text{-}3X^0 + 73.95900000E\text{-}3X^1$

CALIBRATION SUMARY:
Max Uncertainty   : 0.056734 [%]
Max Uncertainty   : 0.000201 [l/s]
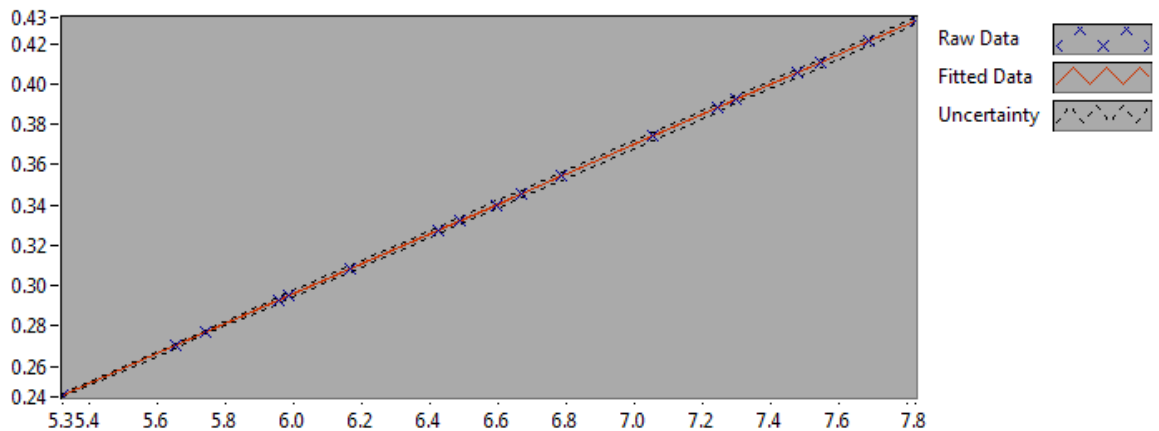RSQ   : 1.000000
Calibration points : 18

Figure 1 : Calibration chart (The uncertainty band is multiplied by 10)

_____
Rakel Ellingsen

CALIBRATION VALUES

Value [l/s]	Voltage [V]	Best Poly Fit [l/s]	Deviation [l/s]	Uncertainty [%]	Uncertainty [l/s]
0.245718	5.320763	0.245718	0.000000	0.033218	0.000082
0.276933	5.742822	0.276933	0.000000	0.040414	0.000112
0.294971	5.986709	0.294971	0.000000	0.050470	0.000149
0.332043	6.487957	0.332043	0.000000	0.048292	0.000160
0.345482	6.669667	0.345482	0.000000	0.055743	0.000193
0.374027	7.055631	0.374027	0.000000	0.050539	0.000189
0.388063	7.245409	0.388063	0.000000	0.048331	0.000188
0.392152	7.300698	0.392152	0.000000	0.043560	0.000171
0.405216	7.477328	0.405216	0.000000	0.046113	0.000187
0.431016	7.826172	0.431016	0.000000	0.041826	0.000180
0.420916	7.689607	0.420916	0.000000	0.041396	0.000174
0.410390	7.547291	0.410390	0.000000	0.046184	0.000190
0.308215	6.165786	0.308215	0.000000	0.049692	0.000153
0.270213	5.651954	0.270213	0.000000	0.040581	0.000110
0.292572	5.954272	0.292572	0.000000	0.047872	0.000140
0.327318	6.424069	0.327318	0.000000	0.047770	0.000156
0.340066	6.596432	0.340066	0.000000	0.051606	0.000175
0.354110	6.786332	0.354110	0.000000	0.056734	0.000201

COMMENTS:

The uncertainty is calculated with 95% confidence. The uncertainty includes the randomness in the calibrated instrument during the calibration, systematic uncertainty in the instrument or property which the instrument under calibration is compared with (dead weight manometer, calibrated weights etc.), and due to regression analysis to fit the calibration points to a linear calibration equation.The calculated uncertainty can be used as the total systematic uncertianty of the calibrated instrument with the given calibration equation.

CALIBRATION REPORT

CALIBRATION PROPERTIES
Calibrated by: Katarina Kloster og Einar Agnalt
Type/Producer: FHCW36W1-AKCAY
SN: 5332548
Range: 0-5 bar
Unit: kPa

CALIBRATION SOURCE PROPERTIES
Type/Producer: Pressurements deadweight tester P3223-1
SN: 66256
Uncertainty [%]: 0,01

POLY FIT EQUATION:
Y= -124.73172075E+0X^0 + 62.78902544E+0X^1

CALIBRATION SUMARY:
Max Uncertainty   : Inf [%]
Max Uncertainty   : 0.151612 [kPa]
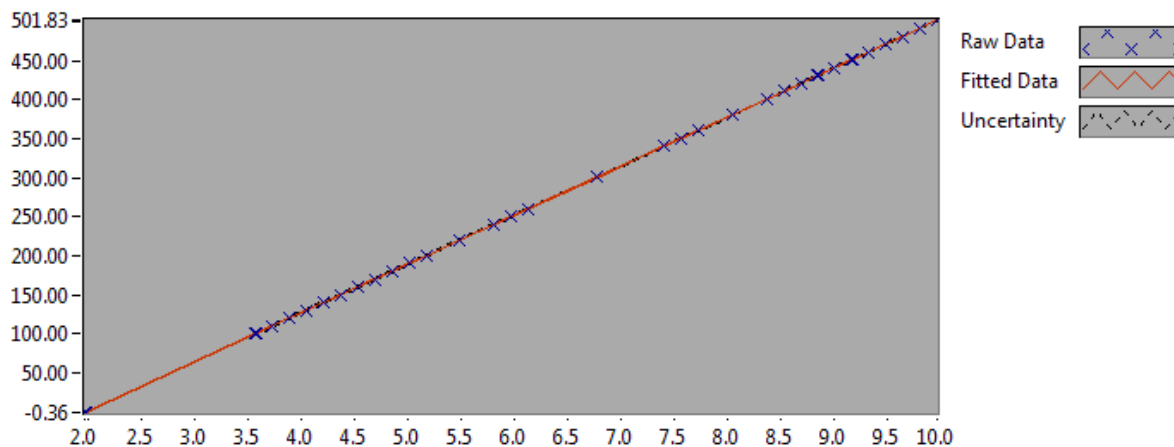RSQ   : 0.999998
Calibration points : 44
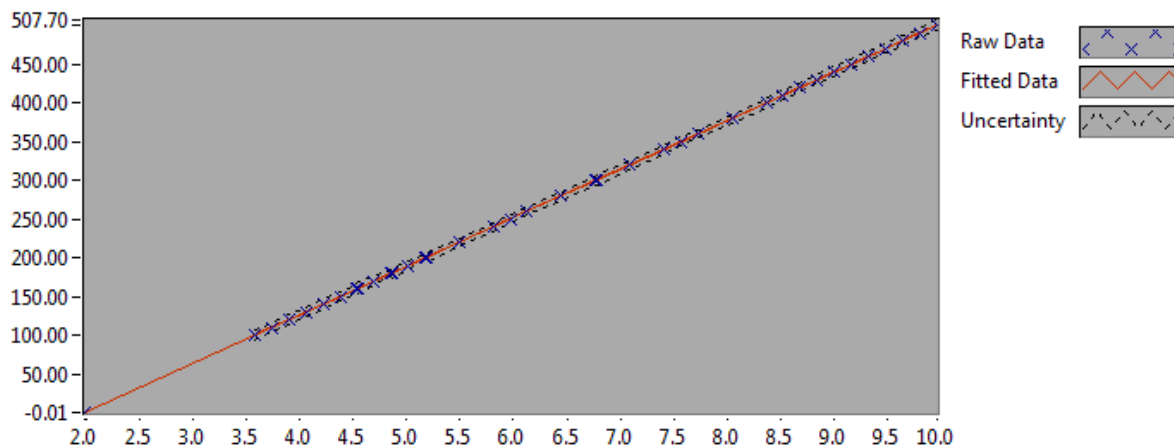
Figure 1 : Calibration chart (The uncertainty band is multiplied by 50)

_____
Katarina Kloster og Einar Agnalt

CALIBRATION VALUES

Value [kPa]	Voltage [V]	Best Poly Fit [kPa]	Deviation [kPa]	Uncertainty [%]	Uncertainty [kPa]
0.000000	1.989080	0.160656	-0.160656	Inf	NaN
100.151071	3.578962	99.987845	0.163226	0.134289	0.134492
110.166178	3.743256	110.303652	-0.137474	0.114797	0.126467
120.181285	3.900404	120.170842	0.010443	0.105924	0.127301
130.196392	4.060813	130.242772	-0.046379	0.100161	0.130406
140.211499	4.218979	140.173829	0.037670	0.086589	0.121408
150.226606	4.380136	150.292744	-0.066137	0.084123	0.126376
160.241714	4.534776	160.002415	0.239298	0.072724	0.116534
170.256821	4.696255	170.141530	0.115290	0.063848	0.108705
180.271928	4.854628	180.085658	0.186269	0.057295	0.103287
190.287035	5.014961	190.152824	0.134211	0.061818	0.117633
200.302142	5.175049	200.204544	0.097598	0.053114	0.106388
220.332356	5.492106	220.112279	0.220077	0.047365	0.104360
240.362570	5.813185	240.272473	0.090098	0.048022	0.115427
260.392784	6.128190	260.051351	0.341433	0.035409	0.092203
280.422999	6.450688	280.300676	0.122323	0.041027	0.115048
300.453213	6.768101	300.230743	0.222470	0.035348	0.106203
320.483427	7.086405	320.216727	0.266700	0.032946	0.105586
340.513641	7.406337	340.304984	0.208658	0.030893	0.105194
360.543855	7.725477	360.343458	0.200397	0.028619	0.103185
380.574070	8.045315	380.425738	0.148331	0.028039	0.106709
400.604284	8.365655	400.539600	0.064684	0.027864	0.111624
410.619391	8.525062	410.548615	0.070776	0.028611	0.117484
420.634498	8.683610	420.503659	0.130839	0.025597	0.107671
430.649605	8.845366	430.660171	-0.010566	0.025353	0.109181
440.664712	9.004142	440.629605	0.035108	0.026875	0.118430
450.679819	9.163264	450.620724	0.059095	0.025478	0.114826
460.694926	9.323779	460.699302	-0.004376	0.025810	0.118907
470.710033	9.483799	470.746745	-0.036711	0.026220	0.123420
480.725141	9.645973	480.929496	-0.204355	0.026831	0.128984
490.740248	9.807166	491.050672	-0.310424	0.026084	0.128006
500.755355	9.966263	501.040222	-0.284867	0.026580	0.133101
450.679819	9.166879	450.847667	-0.167847	0.026375	0.118865
400.604284	8.368133	400.695183	-0.090899	0.030958	0.124020
350.528748	7.569534	350.551950	-0.023202	0.034976	0.122600
300.453213	6.773381	300.562240	-0.109027	0.042605	0.128008
250.377677	5.976573	250.531496	-0.153819	0.044278	0.110861
200.302142	5.181682	200.621028	-0.318886	0.061709	0.123605
180.271928	4.860407	180.448500	-0.176572	0.076228	0.137417
160.241714	4.545116	160.651694	-0.409981	0.094615	0.151612
140.211499	4.221640	140.340960	-0.129461	0.104742	0.146861
120.181285	3.902883	120.326522	-0.145237	0.124271	0.149350
100.151071	3.584595	100.341535	-0.190464	0.133964	0.134166

0.000000   1.986324   -0.012348   0.012348   Inf   NaN

COMMENTS:

The uncertainty is calculated with 95% confidence. The uncertainty includes the randomness in the calibrated instrument during the calibration, systematic uncertainty in the instrument or property which the instrument under calibration is compared with (dead weight manometer, calibrated weights etc.), and due to regression analysis to fit the calibration points to a linear calibration equation. The calculated uncertainty can be used as the total systematic uncertianty of the calibrated instrument with the given calibration equation.

CALIBRATION REPORT

CALIBRATION PROPERTIES
Calibrated by: Katarina Kloster og Einar Agnalt
Type/Producer: FHCW36W1-AKCAY
SN: 5332544
Range: 0-5 bar
Unit: kPa

CALIBRATION SOURCE PROPERTIES
Type/Producer: Pressurements deadweight tester P3223-1
SN: 66256
Uncertainty [%]: 0,01

POLY FIT EQUATION:
Y= -124.21648772E+0X^0 + 62.75555460E+0X^1

CALIBRATION SUMARY:
Max Uncertainty   : Inf [%]
Max Uncertainty   : 0.189217 [kPa]
RSQ   : 0.999999
Calibration points : 45

Figure 1 : Calibration chart (The uncertainty band is multiplied by 10)

_____
Katarina Kloster og Einar Agnalt

CALIBRATION VALUES

Value [kPa]	Voltage [V]	Best Poly Fit [kPa]	Deviation [kPa]	Uncertainty [%]	Uncertainty [kPa]
0.000000	1.983013	0.228610	-0.228610	Inf	NaN
100.151071	3.577036	100.262421	-0.111350	0.128657	0.128851
110.166178	3.731596	109.961878	0.204300	0.119484	0.131631
120.181285	3.892490	120.058866	0.122419	0.107005	0.128601
130.196392	4.053484	130.162127	0.034265	0.108468	0.141222
140.211499	4.217842	140.476531	-0.265032	0.099120	0.138977
150.226606	4.372979	150.212207	0.014400	0.078841	0.118440
160.241714	4.532001	160.191745	0.049968	0.075042	0.120249
170.256821	4.697466	170.575583	-0.318762	0.077902	0.132633
180.271928	4.853362	180.358939	-0.087011	0.067465	0.121620
190.287035	5.013529	190.410310	-0.123275	0.056855	0.108187
200.302142	5.170485	200.260147	0.041995	0.063287	0.126765
220.332356	5.490434	220.338717	-0.006360	0.058905	0.129786
240.362570	5.807117	240.212379	0.150191	0.043605	0.104810
260.392784	6.128818	260.400884	-0.008099	0.039227	0.102144
300.453213	6.763980	300.260855	0.192358	0.034784	0.104509
340.513641	7.402037	340.302422	0.211219	0.030146	0.102653
360.543855	7.724922	360.565301	-0.021445	0.028525	0.102845
380.574070	8.040798	380.388275	0.185795	0.026882	0.102307
400.604284	8.360019	400.421157	0.183127	0.024920	0.099831
410.619391	8.519253	410.413980	0.205411	0.026045	0.106944
420.634498	8.681173	420.575319	0.059179	0.023399	0.098424
430.649605	8.839896	430.536116	0.113489	0.023991	0.103315
440.664712	8.999816	440.571938	0.092774	0.022058	0.097201
450.679819	9.160680	450.667085	0.012734	0.020104	0.090605
460.694926	9.320513	460.697503	-0.002577	0.020977	0.096638
470.710033	9.480630	470.745727	-0.035694	0.020517	0.096577
480.725141	9.639165	480.694632	0.030509	0.021043	0.101159
490.740248	9.800494	490.818957	-0.078709	0.020369	0.099958
500.755355	9.960186	500.840529	-0.085174	0.019844	0.099369
490.740248	9.799922	490.783029	-0.042781	0.020729	0.101727
470.710033	9.481527	470.801998	-0.091964	0.021540	0.101393
450.679819	9.163949	450.872191	-0.192371	0.020908	0.094229
430.649605	8.844076	430.798404	-0.148799	0.022939	0.098786
400.604284	8.363564	400.643591	-0.039307	0.023370	0.093623
350.528748	7.567459	350.683625	-0.154877	0.025636	0.089860
300.453213	6.769154	300.585540	-0.132327	0.030927	0.092920
250.377677	5.971826	250.548757	-0.171080	0.043283	0.108370
200.302142	5.170563	200.265034	0.037108	0.072995	0.146210
180.271928	4.848850	180.075789	0.196139	0.078231	0.141028
160.241714	4.529384	160.027494	0.214220	0.118082	0.189217
140.211499	4.215810	140.349015	-0.137515	0.107308	0.150458
120.181285	3.897584	120.378550	-0.197265	0.133665	0.160640

| 100.151071 | 3.575702 | 100.178686 | -0.027615 | 0.130027 | 0.130223 |
| 0.000000 | 1.973691 | -0.356400 | 0.356400 | Inf | NaN |

COMMENTS:

The uncertainty is calculated with 95% confidence. The uncertainty includes the randomness in the calibrated instrument during the calibration, systematic uncertainty in the instrument or property which the instrument under calibration is compared with (dead weight manometer, calibrated weights etc.), and due to regression analysis to fit the calibration points to a linear calibration equation.The calculated uncertainty can be used as the total systematic uncertianty of the calibrated instrument with the given calibration equation.

Appendix E

Procedure for operation with variable RPM

1 Oscillating RPM or torque

This is a procedure explaining how to produce oscillations in RPM or generator torque in the Francis test rig at the Waterpower Laboratory. The general idea is to send an oscillating RPM or torque current signal to the rectifier cabinet controlling the generator power. Both options are explained in this document.

Set-up of the system

1. **Connect a 9-36 voltage DC power source and banana plug cables to the NI 9265 module**
   The module has a current output ranging from 0 to 20 mA and needs a power source to operate.

2. **Connect the module to a cDAQ**

3. **Find the chosen input channels on the "Francis Generator signals" box**
   The box is located down by the Francis runner, and the signals from the box goes to the rectifier cabinet in the basement which transfers DC power to the generator. If the RPM is to be controlled, the cables from the NI 9265 module shall be connected to the "disturbance RPM"-input. And if the torque is to be controlled, the cables must be connected to the "disturbance TRQ"-input. The different options are seen in Figure 1. Be aware that the input signal starts at 4mA.

4. **Connect other cables if necessary**
   It is also possible to measure the voltage and current sent to the rectifier cabinet by connecting a suitable module to the "Generator voltage/current" input.

5. **Connect the cDAQ to a computer with an usb cable**

6. **Open your LabVIEW project and connect it to the right cDAQ channel**

In the control room

1. **Start up the test rig and go to planned operational point**
   See other procedures if needed.

2. **Activate the "speed/torque korreksjon"**
   It is found under "Francis-generator" and "Kommandoer" on one of the computers. See Figure 3. When this is activated, the RPM/torque is controlled by the current signal sent from the NI module to the rectifier cabinet.

How to run the test rig

1. **Start up the LabVIEW program which controls the oscillations**
   The output from the NI module is given by the coding you have provided in LabVIEW. For example, a sine curve can be used.

2. **An change of 1 mA is equivalent with 6.25 RPM**
   Given that the NI 9265 module only goes up to 20 mA and you have to start at 4 mA, you can only increase/decrease the signal with total of 16 mA, which is equal to 100 RPM.

3. **Always make sure the changes are okay** Try to start with a small increase or decrease. Follow the RPM/torque movement on the screens in the control room.

4. **Change to the original RPM and stop the oscillations**
   To avoid a jump in RPM, let the LabVIEW program run the RPM back to its starting point before you shut it down.

5. **Deactivate the "speed/torque correction"**
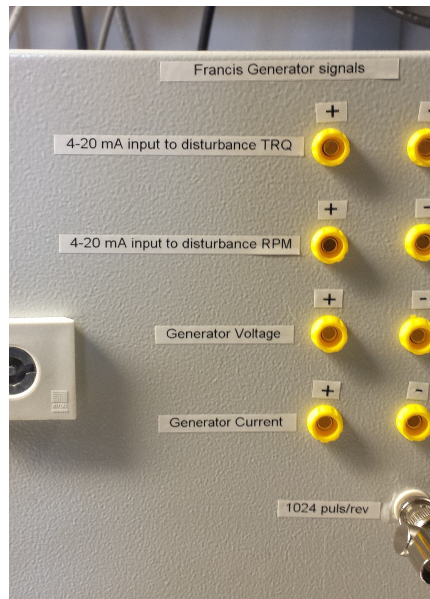
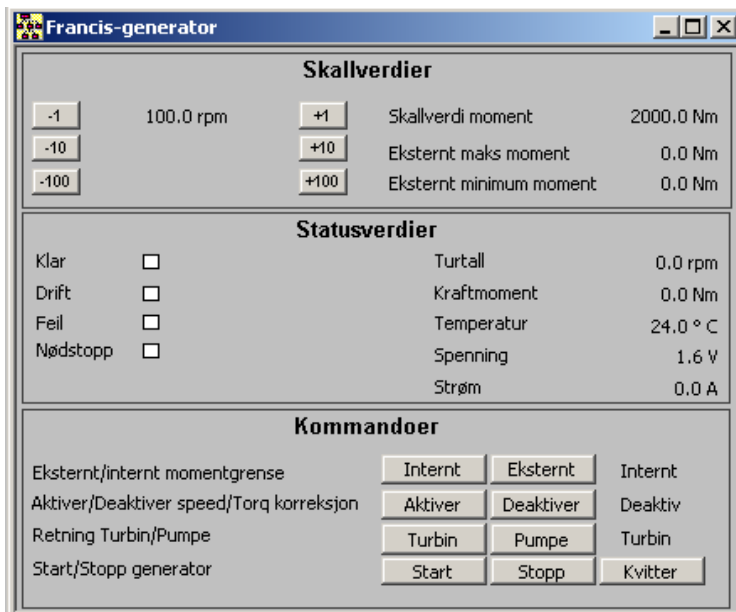Figure 1: "Francis Generator signals" box
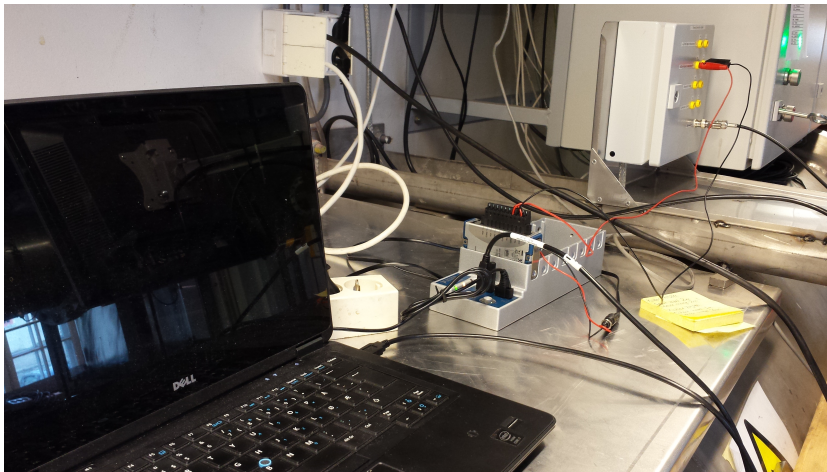
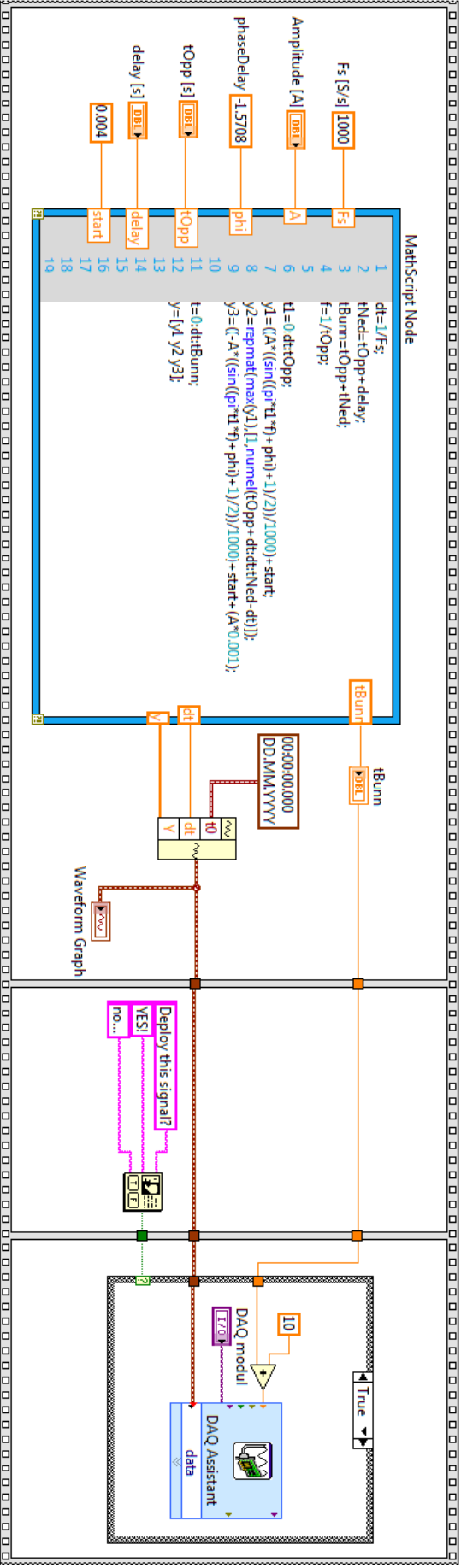Figure 2: Set-up of the system

Figure 3: Screen shot from the computer in the control room

Appendix F

LabView program for controlling RPM

The LabVIEW program shown on the next page has been produced by PhD Candidate Carl Bergan. It uses the application MatchScript to be able to write a script, and further uses the script outputs to create a waveform signal. The signal is transferred to a CompactDAQ and corresponding module when the user choose to deploy it. This specific script produces a signal starting at 4 mA.
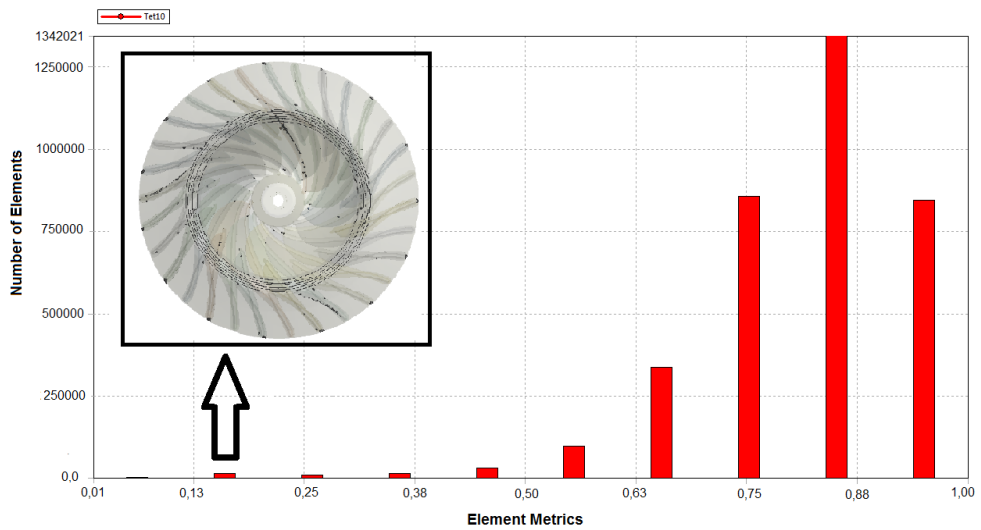
MathScript Node

Fs [S/s] 1000
Amplitude [A]
phaseDelay -1.5708
tOpp [s]
delay [s]
0.004

```
1   dt=1/Fs;
2   tNed=tOpp+delay;
3   tBunn=tOpp+tNed;
4   f=1/tOpp;
5
6   t1=0:dt:tOpp;
7   y1=((A*((sin((pi*t1*f)+phi)+1)/2))/1000)+start;
8   y2=repmat(max(y1),1,numel(tOpp+dt:dt:tNed-dt));
9   y3=((-A*(sin(((pi*t1*f)+phi)+1)/2))/1000)+start+(A*0.001);
10
11
12
13
14  t=0:dt:tBunn;
15  y=[y1 y2 y3];
16
17
18
19
```

start delay tOpp phi A Fs

Y dt tBunn

00:00:00.000
DD.MM.YYYY

tBunn

Waveform Graph

Deploy this signal?
no...
YES!

DAQ modul

10

True

DAQ Assistant
data

Appendix G

Additional results

Figure G.1: Element metrics showing the quality of the mesh elements

G.1 Mesh independence test
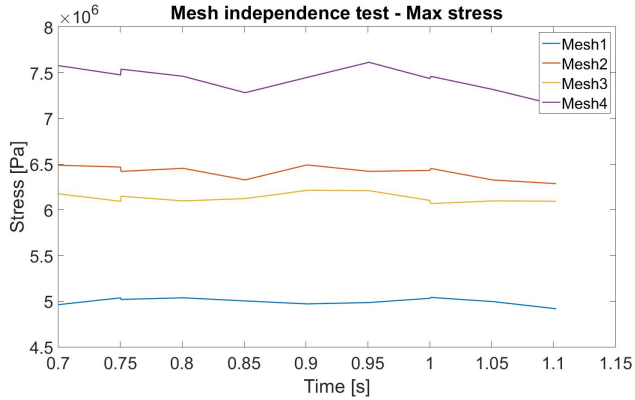
(a) Stress vs. time
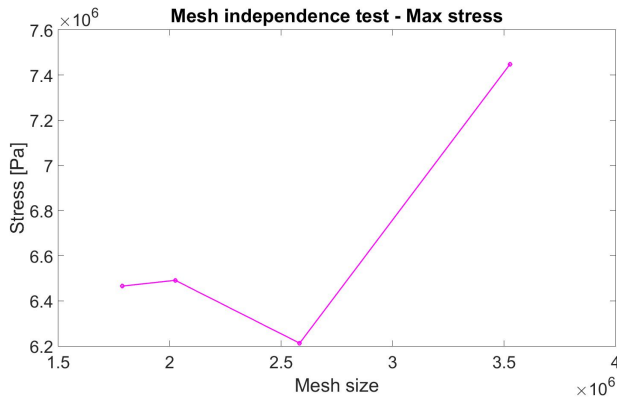
(b) Stress vs. mesh size

Figure G.2: Mesh independence test - Max stress

G.2 von-Mises yield criterion

The von-Mises yield criterion states that yielding will occur whenever the distortion energy in a unit volume is equal to the distortion energy in the same volume when uniaxially stressed to the yield strength [15]. A scalar invariant is derived as von-Mises equivalent stress:
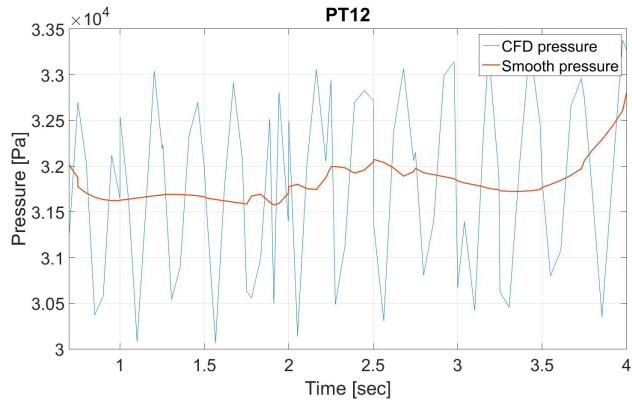
$$\sigma_e = \sqrt{\frac{1}{2}[(\sigma_1 - \sigma_2)^2 + (\sigma_2 - \sigma_3)^2 + (\sigma_3 - \sigma_1)^2]} \tag{G.1}$$

When the von-Mises equivalent stress exceeds the uniaxial material yield strength, general yielding will occur.

G.3   Validation of CFD
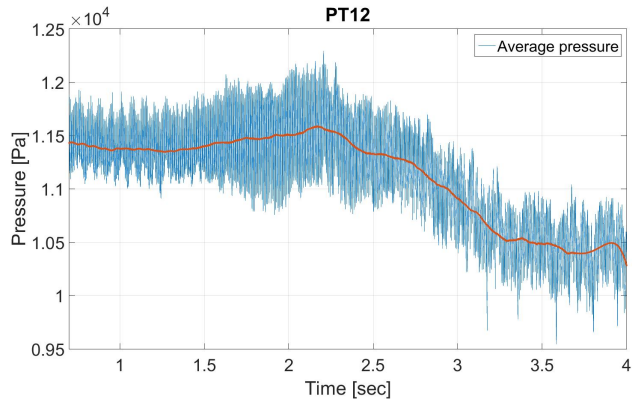
(a) LAB

(b) CFD

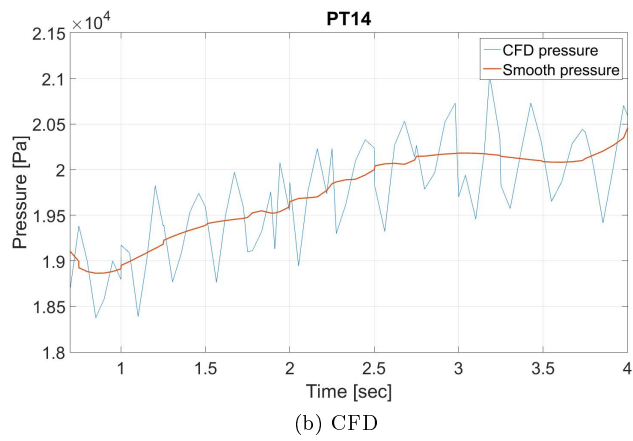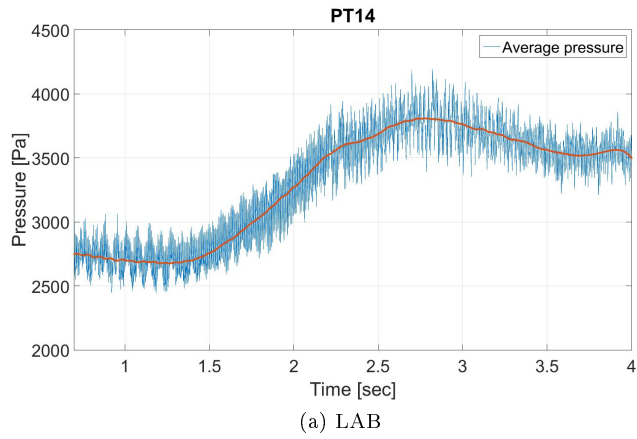Figure G.3: Comparison of pressure results from sensor PT12

(a) LAB

(b) CFD

Figure G.4: Comparison of pressure results from sensor PT14